

## Magnetic adatoms as building blocks for quantum magnetism

Toskovic, Ranko

**DOI**

[10.4233/uuid:d3cfe1fc-5782-4315-9cd1-5c6209814595](https://doi.org/10.4233/uuid:d3cfe1fc-5782-4315-9cd1-5c6209814595)

**Publication date**

2018

**Document Version**

Final published version

**Citation (APA)**

Toskovic, R. (2018). *Magnetic adatoms as building blocks for quantum magnetism*. [Dissertation (TU Delft), Delft University of Technology]. <https://doi.org/10.4233/uuid:d3cfe1fc-5782-4315-9cd1-5c6209814595>

**Important note**

To cite this publication, please use the final published version (if applicable).  
Please check the document version above.

**Copyright**

Other than for strictly personal use, it is not permitted to download, forward or distribute the text or part of it, without the consent of the author(s) and/or copyright holder(s), unless the work is under an open content license such as Creative Commons.

**Takedown policy**

Please contact us and provide details if you believe this document breaches copyrights.  
We will remove access to the work immediately and investigate your claim.

**MAGNETIC ADATOMS AS BUILDING BLOCKS FOR  
QUANTUM MAGNETISM**



# **MAGNETIC ADATOMS AS BUILDING BLOCKS FOR QUANTUM MAGNETISM**

## **Proefschrift**

ter verkrijging van de graad van doctor  
aan de Technische Universiteit Delft,  
op gezag van de Rector Magnificus prof. dr. ir. T.H.J.J. van der Hagen,  
voorzitter van het College voor Promoties,  
in het openbaar te verdedigen op dinsdag 19 juni 2018 om 10:00 uur

door

**Ranko TOSKOVIC**

Master of Science in Nanoscience and Nanotechnology,  
KU Leuven and Chalmers University of Technology,  
geboren te Niksic, Montenegro.

Dit proefschrift is goedgekeurd door de

promotor: Dr. A.F. Otte

promotor: Prof. dr. ir. H.S.J. van der Zant

Samenstelling promotiecommissie:

Rector Magnificus,

Dr. A.F. Otte,

Prof. dr. ir. H.S.J. van der Zant,

voorzitter

Delft University of Technology, The Netherlands

Delft University of Technology, The Netherlands

*Onafhankelijke leden:*

Prof. dr. F. Mila,

Prof. dr. J.M. van Ruitenbeek,

Prof. dr. Y.M. Blanter,

Dr. M. Ternes,

Dr. T. van der Sar,

EPFL, Switzerland

Leiden University, The Netherlands

Delft University of Technology, The Netherlands

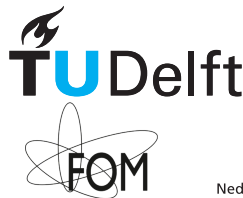
Max Planck Institute for Solid State Research, Germany

Delft University of Technology, The Netherlands

*Reservelid:*

Prof. dr. ir. T.M. Klapwijk,

Delft University of Technology, The Netherlands



Delft  
University of  
Technology



Nederlandse Organisatie voor Wetenschappelijk Onderzoek

*Keywords:* atomic magnetism, scanning tunneling microscopy, inelastic electron tunneling spectroscopy

*Printed by:* Gildeprint

*Front & Back:* Dr. M.C. Martinez Velarte

Copyright © 2018 by R. Toskovic

Casimir PhD Series 2018-15

ISBN 978-90-8593-347-2

An electronic version of this dissertation is available at

<http://repository.tudelft.nl/>.

*To my parents*



# CONTENTS

<b>1</b>	<b>Introduction</b>	<b>1</b>
1.1	Quantum magnetism . . . . .	2
1.2	Quantum simulation . . . . .	3
1.3	STM as a tool for analog quantum simulation. . . . .	4
1.4	Thesis layout . . . . .	5
<b>2</b>	<b>Theory</b>	<b>7</b>
2.1	Quantum criticality and quantum phase transitions . . . . .	8
2.2	Spin-1/2 chains . . . . .	9
2.3	Spin-1/2 XXZ Heisenberg chain in transverse field . . . . .	11
2.3.1	Analysis for $\Delta = 0.125$ . . . . .	12
2.3.2	Relation to spin-3/2 Co chains on Cu <sub>2</sub> N/Cu(100) . . . . .	14
2.3.3	Appendix: Jordan-Wigner transformation . . . . .	16
<b>3</b>	<b>Experimental set-ups and techniques</b>	<b>21</b>
3.1	STM set-ups . . . . .	22
3.1.1	<sup>3</sup> He STM . . . . .	22
3.1.2	JT STM . . . . .	24
3.2	Sample preparation . . . . .	26
3.2.1	Metal substrates . . . . .	26
3.2.2	Thin insulating layers on metal crystals . . . . .	26
3.2.3	Deposition of magnetic atoms . . . . .	27
3.3	STS techniques . . . . .	28
3.3.1	Inelastic electron tunnelling spectroscopy . . . . .	29
3.3.2	Spin polarized STM . . . . .	31
<b>4</b>	<b>Platforms for building atomic structures</b>	<b>35</b>
4.1	Copper-nitride on Cu(100) . . . . .	36
4.1.1	Copper-nitride reconstruction . . . . .	36
4.1.2	Co adatoms on copper-nitride on Cu(100) – spectroscopy and ma- nipulation . . . . .	37
4.1.3	Atomic dimers – study of different configurations . . . . .	39
4.2	Copper-nitride on Cu <sub>3</sub> Au(100) . . . . .	44
4.2.1	Copper-nitride reconstruction . . . . .	44
4.2.2	Co adatoms on copper-nitride on Cu <sub>3</sub> Au(100) – spectroscopy and manipulation . . . . .	45
4.3	Cl-reconstructed Cu(111) surface . . . . .	46

---

<b>5</b>	<b>Spin chains test of quantum criticality</b>	<b>51</b>
5.1	Introduction . . . . .	52
5.2	STM realization of spin-1/2 XXZ Heisenberg chains. . . . .	52
5.3	Finite chains predictions . . . . .	54
5.4	Experiment and comparison to spin-1/2 XXZ model . . . . .	55
5.5	Observation of onset of quantum criticality in finite atomic chains . . . . .	58
5.6	Conclusions. . . . .	61
<b>6</b>	<b>Controlling spin and orbital inelastic tunneling in atomic chains</b>	<b>65</b>
6.1	Introduction . . . . .	66
6.2	Suppression of spin and orbital excitations in Co atomic chains . . . . .	66
6.3	Suppression mechanism in spin and orbital excitations. . . . .	70
6.4	Magnetic anisotropy of Co atomic chains . . . . .	71
6.5	Conclusions. . . . .	74
<b>7</b>	<b>Probing orbital-specific excitations in single atoms</b>	<b>77</b>
7.1	Co adatoms on Cl-reconstructed Cu(111) surface. . . . .	78
7.2	Orbital-specificity in inelastic excitations . . . . .	79
7.3	Adatom manipulation . . . . .	85
7.4	Conclusions. . . . .	89
	<b>References</b>	<b>91</b>
	<b>Summary</b>	<b>103</b>
	<b>Samenvatting</b>	<b>105</b>
	<b>Acknowledgements</b>	<b>107</b>
	<b>Curriculum Vitæ</b>	<b>113</b>
	<b>List of Publications</b>	<b>115</b>

# 1

## INTRODUCTION

*Physics at the level of an atom is dominated by laws of quantum mechanics. Often, this is entangled with a high complexity in behavior of the systems at that length scale. Unravelling the properties of a material at the atomic level is, therefore, a challenging task that easily supersedes current computational capabilities. A route to circumvent this problem is found in physical realization of simpler quantum systems that are representative of the complex quantum systems one is interested in. These simpler physical systems, unlike their more complex counterparts, can actually be measured and information about the complex system, otherwise inaccessible, gained. In this thesis, we focus mainly on the property of magnetism in spin chains. To mimic these complex systems, we employ a scanning tunnelling microscope to build atomic chains on solid state surfaces and probe their magnetic properties.*

## 1.1. QUANTUM MAGNETISM

Magnetism is a phenomenon arising whenever an atom has unpaired electrons in one of its shells. The spin of this unpaired electron has no spatial preference for orientation until it gets exposed to some form of external stimuli such as an external magnetic field, a crystal field of a material it is embedded in/on or another atom with unpaired electrons. Combination of both the field generated by the structure of the host material and the external field can result in atomic magnetic moments arranging themselves in a particular manner across a large spatial scale, creating a macroscopically ordered magnetic state.

The fashion in which this macroscopic ordering develops in different materials as a function of size and external stimuli, starting from the basic building block – a single atom with a number of unpaired electron spins – is an interesting question to tackle. Understanding this, one would possess the knowledge on emerging interactions between the materials constituting parts and could influence their further development, tailoring magnetism on a macro-scale by manipulating it controllably on a nano-scale. Therefore, the bottom-up study of the rise of magnetism as a function of the system size should begin with understanding the magnetism of a single magnetic atom and the simplest structure one can construct out of single atoms – an atomic chain.

Studying single magnetic atoms demands accounting for the effects of quantum mechanics (QM) that determine physical properties of a system at a (sub-)nanometer scale. First, at zero temperature, the low-energy spectrum of a single magnetic atom is composed out of discrete states, each one corresponding to a unique composition of spin states in different atomic orbitals. Next, QM imposes selection rules that determine which transitions between those levels are possible with an experimental probing tool, preserving quantities such as charge, energy and angular momentum in the investigated system. Understanding the low-lying energy levels of individual atoms and having control of the transitions between them is the first step towards controllable bottom-up large scale engineering of spin structures, atom-by-atom.

Physically accessing low-dimensional quantum systems such as a magnetic atom (0D) [1–18] or a molecule [10, 19–21] on a solid surface and constructing larger structures out of them, such as spin chains (1D) [22–31], or spin arrays (2D) [32–34] is already possible with a scanning tunneling microscope (STM). STM allows for control over size of the system with atomic precision and also over exact positioning and the geometry of the system, influencing in that way the interaction of the spin of an atom with other spins in the structure or the material that surrounds it. By combining the STM mechanical precision of structure building with a spectroscopic ability – scanning tunneling spectroscopy (STS) – one gets a powerful synergetic tool, STM-STS, that constructs and probes the spin states of individual atoms within atomic structures. Here lies the power of STM engineering – its ability to tailor the interactions of a magnetic atom with the environment and monitor the changes along the way. This unique opportunity to engineer a system from a level of an atom and measure its properties as it scales up, gives the STM an interesting role – the one of a quantum simulator.

## 1.2. QUANTUM SIMULATION

A quantum simulator (QS) is any controllable quantum system that can simulate another less controllable or accessible quantum system [35]. By a "controllable" quantum system, the following is assumed: 1) initial state of the system can be (physically) prepared, 2) evolution (Hamiltonian) of the initial state can be engineered and 3) final state can be measured. As long as there is correspondence between the initial/final state of the QS and the initial/final state of the quantum system to be simulated, then the quantum system can be simulated with the QS.

Simulating a quantum system becomes useful in case the size of the system is so large that it impedes calculating its properties on a classical computer. Let us take an example of a 1D quantum system in a form of a chain of  $N$  spin-1/2 particles (e.g. spin-1/2 atoms on a solid surface that can be readily made with an STM). Each of these spins has 2 states, "up" and "down", constituting a total of  $2^N$  states to be written in a computer memory. These states represent the probability amplitudes of wavefunctions of all the possible spin configurations. So, to write down all the configurations the system can assume in its initial state, we need to store  $2^N$  numbers. For a chain of  $N = 40$  spin-1/2 atoms, the requirement on the computer memory would be 4 TB (terabytes). Even worse, to calculate the time evolution of this system, one needs to exponentiate  $2^N \times 2^N$  matrix elements. This leads to a computational problem known as the *exponential explosion*. Classical computers cannot deal this simple QM system (spins can take only 2 values) already at a few tens of spins.

The reason for which classical computers fail is because their computation time grows exponentially with the number of particles of the QM system  $N$ . Alternative to diagonalizing full Hamiltonian of large QM systems and, in that way, avoiding the exponential explosion, has already been developed in a form of Monte Carlo algorithms. These stochastic methods cut the computation time by sampling functions in relatively small number of points. However, if the function changes sign or doesn't vary slowly (like in the case of fermionic and frustrated systems), statistical error grows exponentially with  $N$ , and so does the computation time. This is known as the *sign problem* [36]. Other methods have been developed as well for studying large QM systems, such as: density functional theory (DFT), mean-field theories, many-body perturbation theories, etc. However, they all suffer from similar problems which restrict their applicability to solving these systems [35].

The true solution must come in a form a computer whose processing time is intrinsically polynomial in  $N$  (ideally linear). The solution was proposed by Feynman in [37] where he suggests that for solving large QM systems, one should build a computer out of QM elements obeying QM laws. Recalling our  $N = 40$  spin-1/2 particles example, for which we needed 4 classical TB, in a quantum computer we need only 40 quantum bits (qubits) or 5 quantum bytes to represent system states. In [38] it is proved this a quantum computer can indeed be used as a universal QS. However, to simulate a quantum system we do not necessarily need a quantum computer, but rather a simpler quantum device that can mimic the behavior of the quantum system.

A variety of these application-specific Qs has been obtained experimentally already (before the quantum computer). Quantum systems to be simulated by these Qs appear in a number of disciplines: condensed matter physics, high-energy physics, quantum chemistry, cosmology, nuclear physics, etc.<sup>1</sup> What concerns condensed matter physics, applications include (among others) Hubbard models, spin glasses, disordered systems, high critical temperature superconductors, metamaterials, topological order, and also spin models, quantum phase transitions and frustrated systems [35]. We will take a closer look at the Qs used to emulate spin models and their quantum phase transitions.

For simulating spin models, research proposals have been directed mainly towards trapped ions [39–44], neutral atoms [39, 45, 46] and polar molecules [47] in an optical lattice and superconducting qubits and resonators [48]. Physical realizations have also been reported mostly for trapped ions [49–56], with scarce realizations with superconducting circuits [57] and nuclear spins [58]. Quantum phase transitions have been detected in experiments with trapped ions [50, 53, 55] and neutral atoms in an optical lattice [59, 60]. Neutral atoms are strong in terms of scaling (good control over at least tens of qubits), while lacking in control and readout of individual qubits. Trapped ions and superconducting circuits, on the other hand, are good in individual control and readout, but scaling is a challenge. Nuclear spins are already well established (readily available technology) but lack in both scaling and individual control. In summary, problems with existing Qs revolve around scaling and control over individual qubits.

### 1.3. STM AS A TOOL FOR ANALOG QUANTUM SIMULATION

STM-STs does not suffer from problems intrinsic to currently used as Qs. On the contrary, it is designed to access individual atoms (whose spin states can potentially be treated as qubits) and measure them one-by-one (individual control and readout). What concerns the size of the system, dimensions of the building surface platform on which the atoms are manipulated can be readily tens or even hundreds of nanometers wide on metal crystals (as will be shown later in this thesis). This allows for potential building of atomic structures containing hundreds or even thousands of spins in the future (scaling).

Putting terms as quantum simulation and STM together, one needs to precisely define the STM as a creation tool for analog Qs. An analog Q is an actual quantum physical system that emulates another (much more complex) quantum physical system. The task of the STM is to build spin structures by assembling magnetic adatoms into a surface structure of pre-defined geometry that would emulate a particular quantum system.

Firstly, by a controlled preparation of the building platform, one controls the interaction of the magnetic adatom with the substrate [3, 5, 8, 9, 12, 13, 21, 61]. Secondly, by engineering the positioning and distances between the adatoms, STM controls sign and strength of interactions between magnetic adatoms [22, 24, 29, 32, 62, 63]. Finally, STM

---

<sup>1</sup>For an extensive list of applications with their corresponding Qs the reader is referred to [35].

can probe those interactions by performing STS, with a single adatom precision. In this way, an STM experiment defines and measures interactions within the analog QS and this is crucial for establishing the QS (magnetic adatom structure) as a faithful representation of the actual quantum system one is interested in.

STM is a suitable candidate for studies on theoretical models of 1D and 2D spin structures whose properties are not well known due to computational problems arising from their size. By controllably manipulating magnetic adatoms into desired (simulator) systems, STM can provide theorists with valuable insight into those large 1D and 2D systems. Moreover, this insight could act as a precursor for further theoretical (and experimental) studies.

## 1.4. THESIS LAYOUT

In this thesis I present STM experiments on Co adatoms on three distinct solid surfaces – nitride-reconstructed Cu(100), nitride-reconstructed Cu<sub>3</sub>Au(100) and chlorine-reconstructed Cu(111). In addition to single adatoms, studies on Co atomic chains built along different directions on nitride-reconstructed Cu(100) will be presented in detail. The thesis is organized as follows.

In **chapter 1** I give a brief outlook on the topic of quantum simulation and the function STM studies on magnetic adatoms have in it as an analog simulation tool.

**Chapter 2** presents briefly the theory behind the well known theoretical model of a spin-1/2 chain – XY chain in transverse field. Here we elaborate on how a particular type of Co atomic chain we constructed using STM on a Cu<sub>2</sub>N/Cu(100) surface can be translated onto an effective spin-1/2 chain that has a form of an XY chain in transverse field. In other words, here I show the correspondence between a quantum system we want to simulate (XY chain in transverse field) and its analog QS (our Co chain).

In **chapter 3** I describe the experimental STM setups we use followed by a general elaboration on the experimental preparation of surfaces we use for studies on magnetic atoms. The chapter concludes with a discussion on measurement techniques used for our studies on the atoms.

**Chapter 4** presents three surface platforms used for our quantum magnetism studies. Next to that, a detailed study on interaction within the smallest atomic chain of Co atoms on one of those, Cu<sub>2</sub>N/Cu(100), is given here. Atomic chains discussed in chapters 5 and 6 rely heavily on the interaction findings of this experiment. This is followed by initial results on single Co atoms on the second platform, copper-nitride on Cu<sub>3</sub>Au(100), that holds promise for STM construction of atomic structures at least an order of magnitude larger compared to Cu<sub>2</sub>N/Cu(100). The chapter concludes with the third platform, Cl-reconstructed Cu(111), that could potentially surpass all the previous ones in terms of structure size one could build on it and could potentially, due to its geometry, be used for frustrated magnetism studies.

A study on an STM-assembled atomic QS is shown in **chapter 5**. STM-assembled atomic chains of Co along a nitrogen-vacancy direction of  $\text{Cu}_2\text{N}/\text{Cu}(100)$  are used as a QS for a spin model of an XY chain in transverse field. Here I report on experimental observation of the onset of quantum criticality that would, in a limit of an infinite chain, lead to a quantum phase transition in the XY chain at a critical value of the transverse magnetic field.

**Chapter 6** introduces STM as a control device that, by modifying the geometry of direct surroundings of an atom, influences the very existence of magnetic excitations of the atom. This is shown through an experimental study on Co chains STM-assembled along a nitrogen direction on  $\text{Cu}_2\text{N}/\text{Cu}(100)$ .

**Chapter 7** shows results on a system never reported on before in the STM community – a Co adatom on a Cl-reconstructed  $\text{Cu}(111)$  surface. I show an STM study on Co on this surface, supported by DFT and multiplet calculations. Experimental findings, supported by theoretical calculations, suggest we are probing inelastic excitations of the Co atom with subatomic resolution.

# 2

## THEORY

*In this chapter we introduce a general concept of quantum phase transitions and quantum criticality and discuss them within a framework of spin chains. Spin chains with spin  $S = 1/2$  are of particular interest as these systems exhibit the strongest quantum fluctuations leading to exotic matter states (spin liquids) in the quantum critical region. Here we show how a particular type of Co chain we obtain in our lab is formally mapped onto a class of spin-1/2 chains – the XY chain, thus demonstrating the capability of STM to act as an analog quantum simulator for complex systems that exhibit critical behavior.*

## 2.1. QUANTUM CRITICALITY AND QUANTUM PHASE TRANSITIONS

Magnetism in materials develops as a result of a large scale collective spin behavior leading to spins being organized (ordered) in a particular fashion. The different ordering phases are well known and explained for a number of systems, but what is less known and more intriguing are the transition regions in-between the different ordered phases. In other words, one would like to know what conditions need to be met for a system to undergo a phase transition separating two ordered phases and what the physical properties of a system in that transition region are.

Phase transitions are well known in many systems at finite temperatures, where thermal motion "melts" the low temperature ordering and the system is disordered above the critical temperature. Upon reducing the temperature to zero, one would expect the order to prevail. However, due to Heisenberg's uncertainty principle which states that position and velocity of a particle cannot be simultaneously known, so-called quantum fluctuations take place (zero-point motion). Quantum fluctuations prohibit ordering from happening even at zero temperature and are responsible for a new class of phase transitions – quantum phase transitions (QPTs) [64–66]. The most famous example of a QPT is the transition occurring in helium that, due to strong quantum fluctuations, cannot remain solid even at zero temperature unless pressure is applied to stabilize the structure.

Even though QPTs occur at the experimentally inaccessible zero temperature and can therefore never be truly captured in an experiment, critical behavior associated with their existence can be felt at finite (small) temperatures, where the crossover between two ordered phases happens through a critical region, instead of a single point, like at zero temperature. This has practical consequences for critical behavior detection as the critical point is often not accessible in the laboratory setting. However, due to fanning of critical lines from quantum critical point at zero temperature to a V-shaped region at finite temperatures, critical effects can be felt long before the phase transition takes place and existence of phase transitions confirmed by detecting the emergence of critical behavior under accessible experimental conditions.

To reach this critical region, one needs to tune a parameter that will destroy the low temperature ordering and force the system to adopt another form of ordering after crossing the critical region. The critical region is a phase where the system behaves abnormally and no information on the microscopic properties of the material can be inferred from it. It was suggested that in this region, the electrons undergo a spin-charge separation, creating a quantum critical matter with universal scaling properties [67]. Understanding this matter would be useful for material science because of the highly degenerate states that form at the critical point and could potentially allow for controllably driving the system into stable ordered phases.

Spin-1/2 chains are of particular interest in terms of studying quantum criticality and quantum phase transitions as the quantum fluctuations are the expected to be the strongest in these systems. The tuning parameter driving these systems through the critical region is the external magnetic field. We will focus on a particular type of spin-1/2 chain that via magnetic field undergoes a phase transition from AFM ordering to a paramagnetic phase.

## 2.2. SPIN-1/2 CHAINS

One-dimensional (1D) spin structures, as a platform for studies on magnetism, have been widely explored theoretically for both large spins (classical limit) and spin-1/2 (quantum limit) generating an extensive library of knowledge on magnetic ordering in these systems. Despite their seeming simplicity, spin chains can only be exactly solved for particular combinations of intra-chain coupling, field direction, spin and system sizes. We will focus on spin chains in the quantum limit as they are associated with fascinating phenomena such as quantum phase transitions and can exhibit an exotic spin-liquid state. Experimental spin chains discussed in chapter 5 of this thesis are composed of spins with value close to 1/2 and, under certain conditions, can be even mapped onto spin-1/2 systems, as will be shown later in this chapter.

### ANTIFERROMAGNETIC SPIN CHAINS

Spin-1/2 chain with nearest neighbor exchange coupling ( $\mathbf{S}_n \cdot \mathbf{S}_{n+1}$ ) favoring anti-parallel alignment of spins on neighboring sites (antiferromagnetic or AFM coupling) is a prototypical system for studies of quantum magnetism [68]. Its Hamiltonian is given by:

$$H = J_x \sum_{i=1}^{N-1} S_i^x S_{i+1}^x + J_y \sum_{i=1}^{N-1} S_i^y S_{i+1}^y + J_z \sum_{i=1}^{N-1} S_i^z S_{i+1}^z,$$

where  $J_\alpha > 0$  is the AFM exchange coupling value along direction  $\alpha$  ( $\alpha = \{x, y, z\}$ ),  $S_i^\alpha$  the projection of the spin operator  $\mathbf{S}$  at a chain site  $i$  in the  $\alpha$  direction and  $N$  is the length of the spin chain.

Unlike in its classical analogue, where the Néel state is the true ground state (GS), long range order in this quantum system is inhibited even at  $T = 0$  as a consequence of quantum fluctuations (zero-point motion). The GS for this system has been found in [69] to be a many-body singlet ( $S = 0$ ) with algebraically (power-law) decaying correlations between spins on different sites. It can be described by a resonating valence bond state (RVB) introduced in [70] which is essentially a superposition of all the possible singlet pairings (valence bonds) between neighboring spins. Energy gap to higher excited states decays with chain length and excitations of this chain, called spinons, are gapless in the thermodynamic limit ( $N \rightarrow \infty$ ). This is in accordance with the Lieb, Schultz and Mattis theorem which states that the half-integer spins with interactions described by the Heisenberg Hamiltonian either have a non-degenerate GS with a vanishing gap in thermodynamic limit or a degenerate GS with no gap to higher states [71]. In the Ising limit:

$$H_{\text{Ising}} = \mathbf{S}_n \cdot \mathbf{S}_{n+1} = S_n^x S_{n+1}^x + S_n^y S_{n+1}^y + \Delta S_n^z S_{n+1}^z, \quad \Delta \rightarrow \infty,$$

a spin flip generates two spinons and each of them can be visualized as a domain wall separating two regions of AFM ordering phase shifted by  $\pi$ . In the isotropic Heisenberg limit:

$$H_{\text{Heisenberg}} = \mathbf{S}_n \cdot \mathbf{S}_{n+1} = S_n^x S_{n+1}^x + S_n^y S_{n+1}^y + \Delta S_n^z S_{n+1}^z, \quad \Delta \rightarrow 1,$$

each spin flip generates spatially extended spinons and the resulting state is best described as a superposition of states with mostly two and four spinons [72].

### XY SPIN CHAINS WITH AN IN-PLANE MAGNETIC FIELD

Hamiltonian describing the XY spin chain with an in-plane magnetic field is given by:

$$H_{XY} = J_x \sum_{i=1}^{N-1} S_i^x S_{i+1}^x + J_z \sum_{i=1}^{N-1} S_i^z S_{i+1}^z - h \sum_{i=1}^N S_i^z, \quad (2.1)$$

where  $h$  is the field applied along the  $x$  direction. In extreme limits, this chain corresponds either to an Ising chain in a transverse field (TFI), when  $J_z = 0$ , or an Ising chain in a longitudinal field (LFI), when  $J_x = 0$ . This spin chain model is important to us as, under certain approximations, we can formally map our spin-3/2 Co chains from chapter 5 onto this spin chain class.

The TFI limit is exactly solvable in the thermodynamic limit in [73] by means of a Jordan-Wigner (J-W) transformation that maps the coupled spin chain onto a chain of spinless fermions (the details of Jordan-Wigner transformation can be found in the appendix of this chapter). The authors reported on the ground state being two-fold degenerate for  $h < h_c = 1/2J_x$  and non-degenerate with a gap for  $h > h_c$ . More interestingly, in-between these two regions, at  $h = h_c$ , this chain undergoes a quantum phase transition. For study on our chains, the interesting parameter in the XY Hamiltonian is the  $J_z$  term, which couples spins along the field direction (the so-called longitudinal coupling). Upon switching on the  $J_z$  term, there is no qualitative change in the behavior in field in the thermodynamic limit, other than the change in  $h_c$  that now depends on  $J_z$ . For  $J_z \leq J_x$ , the GS is still two-fold degenerate [74].

It is interesting to see how this theory translates onto finite spin chains, as those are the ones we can build in our STM set-ups. The field dependence of finite size spin chains of this type has been studied theoretically in [75] for  $0 < J_z \leq J_x$ . In finite chains, parity in chain length becomes important. For  $h = 0$ , the GS of odd chains is two-fold degenerate, whereas even chains develop a gap between the ground state and the first excited state. For  $J_z = 0$ , this gap increases with the field, for both odd and even chains.

In the rest of the discussion, we will focus on the  $0 < J_z \leq J_x$  region. Upon introducing an infinitesimally small  $J_z > 0$  term, the lowest two states in all chains become non-degenerate, with the energy gap exponentially suppressed with chain length  $N$ . However, there exist field values where the two lowest states cross and form points of GS degeneracy. Each of the crossing points marks the appearance of a new ground state in a chain, and therefore a new value of total magnetization which, in this manner, becomes a step-like function of applied field assuming a discrete set of values. The two lowest states cross each other a number of times before reaching the critical field  $h_c$ , after which there are no more degeneracy points and the energy gap only grows in field. Therefore, for  $h < h_c$ , the first excitation energy ( $E_1 - E_{GS}$ ) displays an oscillatory behavior with an exponentially diminishing amplitude and a linearly increasing frequency with  $N$ .

An interesting observation is discovered in the total number of the GS crossings. As mentioned above, the two states never cross for  $J_z = 0$ . For  $J_z > 0$ , the crossings appear and one would expect this number to increase with the value of  $J_z$ . However, it turns out that the number of crossings is dependent on chain length  $N$  only and amounts to  $(N + 1)/2$

( $N/2$ ) for odd (even) chains. In other words, whether the longitudinal coupling is infinitesimally small or close to  $J_x$ , the number of crossings remains the same. To explain this interesting finding, the authors in [75] make a formal mapping of the spin Hamiltonian in eq. 2.1 onto a system of spinless fermions (via J-W transformation) and apply perturbative theory up to third order in the longitudinal coupling term  $\left(J_z \sum_{i=1}^{N-1} S_i^z S_{i+1}^z\right)$ . Using perturbation theory they reproduce the number of crossings, indicating that the level crossings are a perturbative effect to the TFI model, i.e. they appear already for infinitesimally small  $J_z$ .

Mean field approximation applied to a fermionic system the spin chain is mapped on gives an even better agreement in crossing fields and first excitation energies (compared to the GS oscillations obtained from diagonalizing finite chains) for  $h \neq 0$  and  $J_z \leq 0.8J_x$  [75]. They find that the self-consistent parameters used in the mean field analysis are all independent of  $h$  but one, and consequently treat the chain as an open Kitaev chain [76] where the self-consistent parameters from MF approximation are taken as free parameters and the field dependent parameter is tuned, resulting in ground state crossings. By doing so, they explain the appearance of  $N$  GS crossings as soon as  $J_z \neq 0$  and find an excellent agreement with the spin Hamiltonian diagonalization results in finite chains. This finding indicates correspondence between Majorana edge modes in an open Kitaev chain and the ground state crossings in the TFI chain with longitudinal coupling [77].

### 2.3. SPIN-1/2 XXZ HEISENBERG CHAIN IN TRANSVERSE FIELD

In this section we present the formalism behind a particular spin chain type – a chain composed of spin-1/2 constituents with a particular kind of anisotropic coupling, namely the XXZ coupling (the spins interact with the same strength along two directions, denoted by  $X$ , and with a different strength along the third,  $Z$ , direction). This is a particular case of an anisotropic coupling – the most general description for  $S \geq 1/2$  chains with anisotropic coupling (XYZ) for a field in arbitrary direction, can be found in [68]. In particular, the XXZ spin-1/2 chain is described by the following Hamiltonian:

$$H_{\text{XXZ}} = \sum_{i=1}^{N-1} J_{\perp} (S_i^x S_{i+1}^x + S_i^y S_{i+1}^y) + J_z S_i^z S_{i+1}^z - \mu_B B_x \sum_{i=1}^N g_i S_i^x, \quad (2.2)$$

where the ratio  $J_z/J_{\perp} \cong \Delta$  determines how the ordering evolves in transverse magnetic field  $B_x$  ( $g$  is the  $g$ -factor and  $\mu_B$  Bohr magneton).

In thermodynamic limit ( $N \rightarrow \infty$ ), for  $0 < \Delta < 1$ , a long range Néel order along  $y$  direction and a gap in the excitation spectrum characterize the phase at low fields. With field increasing, quantum fluctuations become stronger and eventually the order is lost and the gap in the spectrum vanishes. This happens at a field value labeled as the critical field –  $B_{\text{crit}}$ . Beyond this field all intrinsic order is lost and replaced by ordering along the transverse field in  $x$  direction [78, 79]. In the vicinity of this critical point, right before the quantum phase transition takes place, there is a region characterized by no long range order between the spins but still some short range order present and a non-zero gap in the excitation spectrum. This phase region is known as a spin-liquid phase and it has received considerable scientific attention lately [80–82].

This model Hamiltonian promises to explain some unusual magnetic field observations in certain compound materials, such as  $(\text{C}_5\text{H}_{12}\text{N})_2\text{CuBr}_4$  [83, 84],  $\text{BaCo}_2\text{V}_2\text{O}_8$  [85, 86],  $\text{CuSe}_2\text{O}_5$  [87] and  $\text{Cs}_2\text{CoCl}_4$  [88, 89]. Experimental reports on this chain type [85, 86, 88, 89] consider spin chains found in bulk materials.

In chapter 5 we will report on a discrete realization of this type of a chain. There we will discuss Co chains built by STM vertical manipulation on a surface and in a geometry that facilitate the necessary experimental conditions for mapping the chains onto this particular theoretical spin chain model. In the rest of this section we discuss the behaviour of such chain in transverse field and show how our spin-3/2 chains with isotropic coupling relate to spin-1/2 chains with XXZ coupling.

### 2.3.1. ANALYSIS FOR $\Delta = 0.125$

Fig. 2.1a shows a phase diagram of the spin-1/2 XXZ Heisenberg chain, given in eq. 2.2 as a function of applied transverse field and the anisotropy coupling parameter  $\Delta$ .

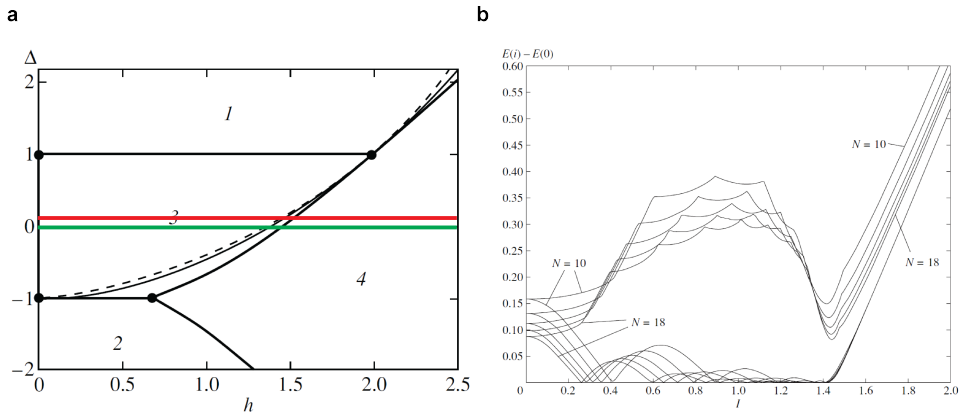


Figure 2.1: **Spin-1/2 XXZ model in transverse field.** **a** Phase diagram as a function of transverse field ( $h$ ) and coupling ( $\Delta$ ), showing 4 different regions defined by critical lines ( $h_c$  – bold solid). Classical line ( $h_{cl}$ ) is shown as thin solid and  $h_1$  as dashed. Chains we discuss in Chapter 5 reside on  $\Delta = 0.125$  line (red). Discussion of the chain model in this chapter follows the red line in (a). **b** Lowest two excitation energies for finite chains of length  $N = 10, 12, 14, 16, 18$  for  $\Delta = 0$  (green line in (a)) as a function of field. Figure adapted from [90].

For  $h = 0$ , the XXZ model is integrable and low-energy properties can be obtained. This is a spin-liquid phase with a linear spectrum and power-law decaying correlations. The energy gap for this case scales as:

$$m \sim h^\nu,$$

where

$$\nu = \frac{2}{4 - \theta - 1/\theta}, \quad \theta = 1 - \frac{\arccos \Delta}{\pi}.$$

Staggered magnetization along  $y$  axis behaves as:

$$\langle |S^y| \rangle \sim h^{\frac{\theta}{4 - \theta - 1/\theta}}.$$

For  $0 < h \leq h_c$ , the XXZ model is not exactly solvable. In this region, staggered magnetization along the  $y$  axis exists (long range Néel order) and the spectrum is gapped up to the transition point where the gap vanishes, the long range order is lost and the chain is characterized by ferromagnetic ordering along the field direction. We will discuss this region by analyzing two characteristic points in the mean field approximation.

The first one will be the one lying on the classical line ( $h_{cl}$ ):

$$h_{cl} = \sqrt{2(1 + \Delta)}.$$

This is a line where quantum fluctuations are compensated by the transverse field and the ground state is identical to the classical one. Namely, it is a two-fold degenerate state with the two states being simply product states of single site functions (two Néel state configurations). Excitation gap is given by:

$$m = \frac{1}{4}(2 - h_{cl})^2$$

Staggered magnetization along  $y$  axis is given by:

$$\langle S_n^y \rangle = \frac{(-1)^n}{2} \sqrt{1 - \frac{h_{cl}}{4}}.$$

For  $n \rightarrow \infty$  spin correlation function decays exponentially:

$$\langle S_1^\alpha S_n^\alpha \rangle - \langle S^\alpha \rangle^2 = f(n)e^{-\kappa n},$$

where  $S_n^\alpha$  ( $\alpha = x, y, z$ ) is the staggered magnetization in the  $\alpha$  direction and  $f(n)$  is a function which is oscillatory for  $0 < h < h_{cl}$ , monotonic for  $h > h_{cl}$  and 0 for  $h = h_{cl}$ . For  $h_{cl} - h \ll 1$ , the function reads:

$$f(n) \approx \frac{\cos(\omega n)}{n^2} \quad \omega = \sqrt{2 \frac{h_{cl} - h}{h_{cl}}}.$$

The next point we will discuss is the one on the transition line ( $h_c$ ). This line connects the two limit points  $\Delta \rightarrow \pm\infty$  where the model is reduced to an Ising chain in transverse field (ITF). The same long range order is assumed on the entire classical line as well with algebraically decaying correlations. In the vicinity of the  $h_c$  line ( $h \rightarrow h_c$ ), staggered magnetization along  $y$  axis behaves as:

$$\langle S_n^y \rangle \propto (h_c - h)^{1/8}.$$

For  $h \rightarrow h_c$ , magnetization  $S$  has a logarithmic singularity. On the transition line ( $h = h_c$ ) spin correlation functions have a power-law decay:

$$\langle S_1^x S_n^x \rangle - \langle S^x \rangle^2 \propto 1/n^2, \quad \langle S_1^y S_n^y \rangle - \langle S^y \rangle^2 \propto 1/n^{1/4}, \quad \langle S_1^z S_n^z \rangle - \langle S^z \rangle^2 \propto 1/n^{9/4}.$$

This line can be observed in numerical energy calculations of finite chains. Fig. 2.1b shows lowest two excitation energy calculations for finite even chains of lengths  $N = 10$  to 18 as a function of transverse field. This graph does not correspond to the coupling value  $\Delta$  in our chains, but to  $\Delta = 0$  instead (green line in Fig. 2.1a). However, conclusions drawn from this graph are valid for our chains too as our chains, indicated by the red line, reside in the same regions of the phase diagram (3 and 4).

First, we analyze the lower curves (1<sup>st</sup> excitation energy) which show the ground state crossings. It is evident that as the chain size increases this excitation energy decreases for all field values below the critical point. In the thermodynamic limit ( $N \rightarrow \infty$ ), the 1<sup>st</sup> excitation energy goes to zero as the ground state becomes degenerate with the 1<sup>st</sup> excited state. The ground state crosses the lowest excited state  $N/2$  times and the last crossing sits on the transition line. The gap to higher states (here only 2<sup>nd</sup> excitation energy shown) remains open for all non-zero fields. However, for increasing  $N$ , it becomes smaller at the critical point where it vanishes for  $N \rightarrow \infty$ .

### 2.3.2. RELATION TO SPIN-3/2 CO CHAINS ON $\text{Cu}_2\text{N}/\text{Cu}(100)$

To capture the effect of nearest neighbor spin-spin interaction, crystal field of the underlying surface and external magnetic field, the following model Hamiltonian describing our Co chains is used:

$$H_{3/2} = J \sum_{i=1}^{N-1} \mathbf{S}_i \mathbf{S}_{i+1} - \sum_{i,\mu} (\lambda^2 \Lambda_{\mu\mu} S_{\mu}^i S_{\mu}^i + 2(1 - \lambda \Lambda_{\mu\mu}) \mu_B B_{\mu} S_{\mu}^i), \quad (2.3)$$

where  $\mathbf{S}_i$  and  $\mathbf{S}_{i+1}$  are total spins of the two neighboring atoms which couple isotropically with strength  $J$ ,  $B$  is the magnetic field,  $\mu_B$  the Bohr magneton,  $\lambda$  the spin-orbit constant ( $\lambda = -21$  meV for Co adatom [91]),  $N$  the length of a chain and  $\mu = x, y, z$ . Term  $J$  represents Heisenberg coupling between two spins and its sign defines the preferred relative orientation of two adjacent spins:  $J > 0$  corresponds to a situation where spins point in opposite directions (antiferromagnetic or AFM coupling) and  $J < 0$  to a situation where spins point in the same direction (ferromagnetic or FM coupling).  $\Lambda_{\mu\mu}$  is the anisotropy parameter that comes out from the second-order perturbation theory by expanding the spin-orbit coupling term  $\lambda \mathbf{L} \cdot \mathbf{S}$  [62, 91] and serves as a quantitative measure for the extent to which the orbital angular momentum  $L$  is quenched along  $\mu$  direction.

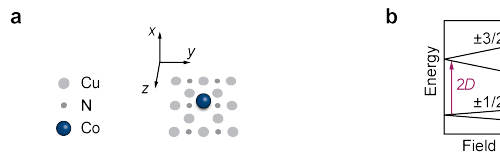


Figure 2.2: **Anisotropy of a Co adatom on  $\text{Cu}_2\text{N}/\text{Cu}(100)$ .** **a** Schematics of a Co adatom with its nearest underlying environment. **b** Energy diagram of a single Co adatom showing magnetic field evolution of its low energy states.

For the case of a single Co atom, these anisotropy parameters amount to:  $\Lambda_{zz} = 0$ ,  $\Lambda_{xx} = \Lambda_{yy} = 6.4 \text{ eV}^{-1}$  with axes as defined in Fig. 2.2a. In terms of phenomenological parameters, these  $\Lambda$  parameters correspond to  $D = +2.75 \text{ meV}$  and  $E = 0$ , where  $D$  and  $E$  are uniaxial and transverse anisotropy, respectively. Note that the positive value for  $D$  corresponds to hard-axis (easy plane) anisotropy (i.e. the spin prefers to orient in a certain plane, rather than along a particular axis) and the negative value of  $D$  to the easy-axis case [92] (i.e. the spin prefers to orient along a particular axis rather than in a certain plane). These  $\Lambda$  numbers for the Co adatom on  $\text{Cu}_2\text{N}/\text{Cu}(100)$ , therefore, translate into a hard-axis anisotropy for the Co adatom on this surface along the  $x$  (vacancy) direction, which shifts the  $\pm 3/2$  states above the lower  $\pm 1/2$  states by  $2\lambda^2\Lambda_{zz} = 5.5 \text{ mV}$  [3, 92] as shown in Fig. 2.2b. This energy is resolved in an IETS spectrum of a Co adatom as a step and will be shown in section 4.1.2. where a detailed discussion on the IETS spectrum of a single Co adatom on  $\text{Cu}_2\text{N}/\text{Cu}(100)$  is presented.

Written in terms of the phenomenological parameters  $D$  and  $E$ , the Hamiltonian given in eq. 2.3 in out of plane field becomes:

$$H_{3/2} = J \sum_{i=1}^{N-1} \mathbf{S}_i \mathbf{S}_{i+1} + D \sum_{i=1}^N (S_i^x)^2 - g\mu_B B_x \sum_{i=1}^N S_i^x. \quad (2.4)$$

As can be seen in Fig. 2.2b, for zero field, this Hamiltonian results in an energy spectrum consisting of two doublets: one comprised of  $m_z = \pm 3/2$  states and one with  $m_z = \pm 1/2$  states. Assuming anisotropy is the dominant energy contribution in the Hamiltonian given by eq. 2.4, i.e.:

$$J, k_B T, \mu_B B \ll 2D, \quad (2.5)$$

we can treat our spin-3/2 chain as an effective spin-1/2 chain. Mathematically, one needs to project out the excitations from the ground state,  $m_z = \pm 1/2$ , to the  $m_z = \pm 3/2$  states and that is done by the Schrieffer-Wolff transformation up to first order in  $1/D$  [93–95], resulting in the following effective spin-1/2 Hamiltonian:

$$H_{1/2} = \sum_{i=1}^{N-1} J_{\perp} (S_i^x S_{i+1}^x + S_i^y S_{i+1}^y) + J_z S_i^z S_{i+1}^z + J_{\perp}^{\text{nnn}} \sum_{i=1}^{N-2} S_i^x S_{i+2}^x + S_i^y S_{i+2}^y - \mu_B B_x \sum_{i=1}^N g_i S_i^x, \quad (2.6)$$

where the generated exchange parameters are:

$$J_{\perp} = 4J, \quad J_z = J - \frac{39J^2}{8D}, \quad J_{\perp}^{\text{nnn}} = -\frac{3J^2}{D} \quad (2.7)$$

and the bulk/boundary g-factors:

$$g_{\text{bulk}} = 2g \left(1 - \frac{3J}{2D}\right), \quad g_{\text{boundary}} = 2g \left(1 - \frac{3J}{4D}\right). \quad (2.8)$$

If the next-nearest neighbor interaction is much weaker compared to the components of the nearest neighbor interaction ( $J_{\perp}^{\text{nnn}} \ll J_{\perp}, J_z$ ), the Hamiltonian becomes the spin-1/2 Hamiltonian with XXZ coupling in transverse field (eq. 2.2).

If in addition to  $J_{\perp}^{\text{nnn}}$ , we neglect the term  $J_z$  (which in our case is 8 times smaller than  $J_{\perp}$ ), we end up with the Hamiltonian describing the TFI chain with the additional coupling along the field direction, described in section 2.2. Therefore, our chain is a special case of  $H_{\text{XY}}$  Hamiltonian, given by eq. 2.1, where  $J_z = J_x$ .

### 2.3.3. APPENDIX: JORDAN-WIGNER TRANSFORMATION

Here we perform formal mapping of a Hamiltonian describing spin-1/2 system with XXZ (eq. 2.2 in zero field) onto a Hamiltonian describing interacting fermions. This section is based on analysis presented in [96] where one can find mathematical details of the transformation we show here. We begin the discussion by writing down anticommutation rules for raising ( $S^+ = S^x + iS^y$ ) and lowering ( $S^- = S^x - iS^y$ ) spin operators on the same site:

$$\{S_i^+, S_i^-\} = 1 \quad \{S_i^+, S_i^+\} = \{S_i^-, S_i^-\} = 0.$$

These relations resemble the ones for creation and annihilation operators for fermions, so the following definitions are introduced:

$$S_i^+ = f_i^\dagger \quad S_i^- = f_i. \quad (2.9)$$

Since  $S_z$  is obtained as  $S_z^z = 1/2[S^+, S^-]$ , we get for the spin operator  $S_z$ :

$$S_z^z = f_i^\dagger f_i - \frac{1}{2}. \quad (2.10)$$

Now we mapped spin operators onto fermionic operators. Physically, we have mapped the "up" state of a spin-1/2 to an occupied fermionic state and the "down" state of a spin-1/2 to an empty fermionic state. However, spin operators acting on different sites commute ( $[S_i^+, S_j^+] = 0$ ), whereas fermionic ones do not. To eliminate this discrepancy, a non-local phase correction must be introduced:

$$S_i^+ = f_i^\dagger U(i, \{j\}) \quad S_i^- = U^\dagger(i, \{j\}) f_i \quad S_z^z = f_i^\dagger f_i - \frac{1}{2}.$$

This phase correction  $U(i, \{j\})$  introduced for site  $i$  depends on wavefunctions of all the other sites  $f_j$  and satisfies relations  $U^\dagger U = 1$  and  $U^+ = U^{-1}$ . In 1D (spin chains), the following expression for  $U$  is proposed by P. Jordan and E. Wigner [97]:

$$U_{1D}(i) = \prod_{k < i} e^{i\pi f_k^\dagger f_k},$$

where the phase term takes into account all states to the left of the  $i^{\text{th}}$  spin and is referred to as the string operator. In this way, a rising and lowering spin operators become products of the fermionic state and the string operator containing information of all the sites to the left of the spin. This is important as it enables proper commutation relations between spin operators to be satisfied:

$$[S_i^+, S_j^-] = 2S_z^z \quad \text{and} \quad [S_i^+, S_j^+] = 0 \quad (i < j).$$

Let us now apply this fermionization of the spin-1/2 operators to our spin chain model – a spin-1/2 chain with XXZ coupling (eq. 2.2 in zero field):

$$H = \frac{J}{2} \sum_j [S_{j+1}^+ S_j^- + S_{j+1}^- S_j^+] + J_z \sum_j S_j^z S_{j+1}^z. \quad (2.11)$$

Using the formalism introduced above (eq. 2.9), the first two terms in our Hamiltonian (eq. 2.11) become:

$$\frac{J}{2} \sum_j S_{j+1}^+ S_j^- = \frac{J}{2} \sum_j f_{j+1}^\dagger f_j, \quad \frac{J}{2} \sum_j S_{j+1}^- S_j^+ = \frac{J}{2} \sum_j f_j^\dagger f_{j+1}. \quad (2.12)$$

These terms correspond to hopping between adjacent fermionic sites. Using eq. 2.10, the last term of the spin Hamiltonian in eq. 2.11 becomes:

$$J_z \sum_j S_{j+1}^z S_j^z = J_z \sum_j \left( \hat{n}_{j+1} - \frac{1}{2} \right) \left( \hat{n}_j - \frac{1}{2} \right), \quad (2.13)$$

where  $n_j$  is the occupation number at site  $j$  which in case of fermions can be either 1 or 0. This part describes the interaction between adjacent fermionic sites. Now the entire fermionic Hamiltonian reads:

$$H_{XXZ} = \frac{J}{2} \sum_j \left( f_{j+1}^\dagger f_j + \text{h.c.} \right) - J_z \sum_j n_j + J_z \sum_j n_{j+1} n_j. \quad (2.14)$$

To write this Hamiltonian in momentum space, a Fourier transformation is used:

$$f_j = \frac{1}{\sqrt{N}} \sum_k f_k e^{ikj} \quad f_j^\dagger = \frac{1}{\sqrt{N}} \sum_k f_{-k}^\dagger e^{ikj},$$

where we put the lattice spacing  $a = 1$  for simplicity;  $N$  is the number of spin sites in the chain. Momentum  $k$  takes discrete values in the first Brillouin zone  $k = 2\pi n/N$  ( $n = 0, 1, \dots, N-1$ ). Operators  $f_k^\dagger$  and  $f_k$  represent creation and annihilation operators for fermions with momentum  $k$ <sup>1</sup>. Now the hopping term in eq. 2.12 can be written as:

$$\frac{J}{2} \sum_j \left( f_{j+1}^\dagger f_j + \text{h.c.} \right) = J \sum_k \cos(k) f_k^\dagger f_k$$

and the first interaction term in eq. 2.13:

$$J_z \sum_j n_j = J_z \sum_k f_k^\dagger f_k.$$

The second interaction term from eq. 2.13 involves only nearest neighbors and can be, therefore, written as:

$$J_z \sum_j n_{j+1} n_j \quad \Longleftrightarrow \quad \sum_{jj'} V_{jj'} n_j n_{j'} \quad \text{where} \quad V_{jj'} = V_{j-j'} = \begin{cases} J_z/2 & \text{for } |j-j'| = 1 \\ 0 & \text{otherwise} \end{cases}.$$

<sup>1</sup>This can be confirmed by expressing  $f_k^\dagger$  and  $f_k$  using inverse Fourier transformation:

$$f_k = \frac{1}{\sqrt{N}} \sum_j f_j e^{-ikj} \quad f_k^\dagger = \frac{1}{\sqrt{N}} \sum_j f_j^\dagger e^{ikj}$$

and calculating the anticommutator:  $\{f_k, f_{k'}^\dagger\} = \delta_{kk'}$

The Fourier transformation of this short-range interaction reads:

$$v_q = \sum_r V_r e^{-iqr} = \frac{J_z}{2} (e^{-iq} + e^{iq}) = J_z \cos(q),$$

which gives the following Fourier transformation of the entire second interaction part:

$$V_{j-j'} = \frac{1}{N} \sum_q v_q e^{iq(j-j')}.$$

Written in terms of second quantization:

$$\sum_{j,j'} V_{j,j'} n_j n_{j'} = \frac{1}{N} \sum_{k,k'} \sum_q v_q f_{k'+q}^\dagger f_{k-q}^\dagger f_k f_{k'} = \frac{J_z}{N} \sum_{k,k',q} \cos(q) f_{k'+q}^\dagger f_{k-q}^\dagger f_k f_{k'}.$$

The entire Hamiltonian in momentum space finally reads:

$$H = \sum_k \omega_k f_k^\dagger f_k + \frac{J_z}{N} \sum_{k,k',q} \cos(q) f_{k'+q}^\dagger f_{k-q}^\dagger f_k f_{k'}, \quad (2.15)$$

where:

$$\omega_k = J \cos(k) - J_z \quad (2.16)$$

is the excitation energy. In case of FM coupling, this is the energy of a magnon and, in case of an AFM coupling, this expression denotes the energy of a spinon.

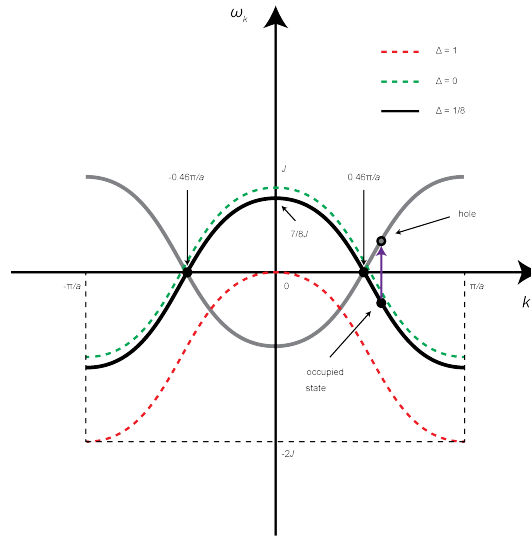


Figure 2.3: **Dispersion spectra for spin-1/2 model with nearest neighbor AFM coupling.** Graph showing dispersion curves  $\omega_k(k)$ , based on eq. 2.16, of the XXZ spin-1/2 AFM chain for three values of anisotropy coupling parameter  $\Delta$ :  $\Delta = \{0, 1/8, 1\}$ , corresponding to XY chain (green), our effective spin-1/2 chain (black) and isotropic Heisenberg chain (red), respectively. Black curve mirrored over  $\omega = 0$  to denote the hole states (gray) of the effective chain and the hole excitation (purple).

This dispersion relation is shown in Fig. 2.3 for three values of  $J_z$  ( $0$ ,  $J/8$  and  $J$ ). As can be seen, our effective spin-1/2 chain is very close to the XY chain in  $k$ -space with zero-energy mode at  $k = 0.46\pi/a$ . Zero mode indicates long range correlations between spins in a chain. Analysis of the low energy excitations ( $k$ -points in the vicinity of  $\pi/2a$ ) shows a power-law decay of spin-spin correlations [96]. Excitations are made by adding a spinon for  $|k| \leq 0.46\pi/a$  or annihilating it (and forming a hole) for  $|k| \geq 0.46\pi/a$ . XY chain-like behavior (gapless spectrum) is preserved up to  $J_z = J$ . For  $J_z > J$ , a gap appears and correlations start decaying exponentially.



# 3

## EXPERIMENTAL SET-UPS AND TECHNIQUES

*A scanning tunnelling microscope (STM) is a sophisticated tool with a three-fold function. Invented in 1986 by Binnig and Rohrer [98], the microscope is widely recognized as a visualization tool for solid conductive surfaces and surface adsorbates with unprecedented lateral and height resolution at the nanoscale going into sub-nanometer range. In addition to its ability to acquire topography information, STM is widely used for probing electronic states of the surface and surface adsorbates (atoms or molecules). Lastly, STM serves as a building tool of 1D and 2D atomic structures on solid surfaces. In this chapter, we describe the two STM setups used for obtaining data presented in the subsequent chapters of the thesis. Section 3.1 presents two commercial low-temperature STM systems used in experiments presented in this thesis. Set-ups are built by Unisoku (3.1.1) and SPECS (3.1.2) and differences between them will be highlighted here. Section 3.2 gives an overview of the working surfaces for magnetic structures presented in this thesis along with the corresponding deposition methods, both for surfaces (3.2.1 and 3.2.2) and surface adatoms (3.2.3). Different experimental techniques employed in obtaining the data are discussed next, in section 3.3. This part of the chapter is dedicated mainly to explaining the mechanisms behind two STM spectroscopy techniques. Principles of the inelastic electron tunnelling spectroscopy (IETS) are shown in 3.3.1 followed by a discussion on the spin-polarized (SP-) IETS technique in 3.3.2.*

### 3.1. STM SET-UPS

Here we describe two experimental STM set-ups used in our lab.

We start with the USM-1300  $^3\text{He}$  STM, made by Unisoku, in 3.1.1. This is a low-temperature STM we employ mostly for studies on spin excitations in single surface magnetic adatoms or atomic structures we build out of such atoms. This system is specially suitable for these studies as sample stage can reach as low as 330 mK and the system is provided with a 2 T / 9 T vector magnet. Both of these are desirable for measuring excitations of magnetic origin in adatoms as they typically occur at a few meV.

The Joule-Thomson (JT) SPM, made by SPECS, is also a low-temperature microscope that allows for magnetic field application. However, JT SPM is typically used for applications that do not require sub-Kelvin and high magnetic field conditions ( $T_{\min} \sim 1$  K,  $B_{\max} = 3$  T) and, as such, is used more as a system for preliminary experiments on magnetic adatoms or investigations of new surface platforms.

The main advantage of the JT SPM system over the  $^3\text{He}$  STM system is the possibility to switch between two working modes: STM and atomic force microscopy (AFM). Work presented in thesis was conducted employing STM techniques only so we will refer to this system as JT STM further on. What concerns the system usage, the important distinction from the  $^3\text{He}$  STM system lies in the position of the STM head. In the  $^3\text{He}$  STM, the STM head and the magnet are positioned inside the cryostat whereas in the JT STM, these are located below the cryostat. This presents the JT STM with the ability to visualize the process of sample/tip insertion onto the STM head via several viewports installed onto this system. More importantly, owing to this design type, the JT STM system has an evaporator unit attached directly to the STM chamber allowing for magnetic atom evaporation onto cold samples (5 – 10 K), which reduces the probability for adatoms clustering on the surface after the evaporation. This can be a limiting factor for adatom studies in the  $^3\text{He}$  STM system where the evaporation takes place outside of the STM head, with the sample at temperatures  $> 60$  K.

The following two subsections cover the important structural and operational aspects of these two systems.

#### 3.1.1. $^3\text{He}$ STM

The schematics of this system are shown in Fig. 3.1a. The system counts three main parts – the STM head, the cryogenic part within which the STM head and magnets are positioned and the room temperature series of connected vacuum chambers for sample preparation and transfer.

##### STM HEAD

The core part of the setup is the STM head depicted in Fig. 3.1b. As mentioned, the head sits inside the cryostat, in its central part which is an ultra high vacuum (UHV) space isolated from but surrounded by a  $^4\text{He}$  bath. The STM head has a sample stage below which the tip is positioned. Coarse motion of the sample stage and the tip is regulated by a Pan-type piezo motor [99] and, for scanning purposes, a piezo tube on top of which the

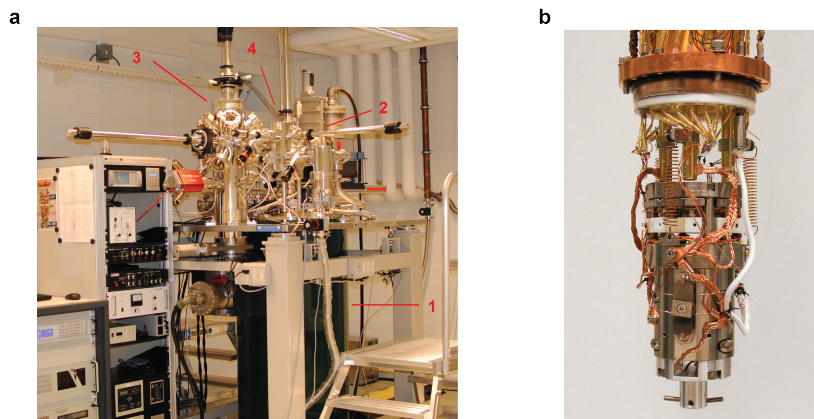


Figure 3.1: **Unisoku  $^3\text{He}$  STM with UHV system.** **a** Externally visible part of the experimental set-up with main parts numbered as: 1 – cryostat, 2 – load lock, 3 – preparation chamber, 4 – exchange chamber. The whole system is attached to a floating table. **b** STM head suspended on 3 springs. A sample stage is located inside the white plate with the tip below. A coaxial cable (white) connects to the tip and carries the current signal we measure.

tip is mounted is employed. The accessible scanning range at low temperatures (1.5 K and lower) is  $520 \times 520 \text{ nm}^2$ . The head is suspended on 3 springs as to dampen vibrational noise. This is essential for achieving atomic resolution. To this end, the entire  $^3\text{He}$  setup is fixed to a floating table supported by a set of 4 passive air legs.

### CRYOSTAT

This system allows for two stable operational temperature regimes – 1.5 K and 330 mK. The cryostat is essentially a dewar (green cylinder in Fig. 3.1a) that can contain up to 120 l liquid  $^4\text{He}$ , the lifetime of which varies between 6 and 7 days (by ‘lifetime’ we refer to the time it takes before  $\sim 90\%$  of the liquid  $^4\text{He}$  has evaporated from our system into the helium recovery line connected to the dewar). Pumping on the 1-K pot allows us to reach 1.5 K at the STM head. To go to 330 mK, we use a closed cycle of  $^3\text{He}$  recondensation which occurs in a small pot located in the vicinity of the STM head [99]. A fixed amount of  $^3\text{He}$  (20 l of gas at atmospheric conditions) is stored in an external container. After its recondensation in the cryostat, we typically have 18 – 24 h at 330 mK before  $^3\text{He}$  has evaporated, the exact duration being strongly dependent on the number of sample insertions and the usage of magnets during that period. The process of recondensing  $^3\text{He}$  and achieving a stable temperature of 330 mK afterwards typically takes 1 – 2 h.

A superconducting vector magnet is immersed near the bottom of the cryostat, surrounding the sample stage. A split-coil allows for up to 2 T in one of the sample plane directions and a solenoid provides for up to 9 T perpendicular to the sample.

### UHV CHAMBERS

The UHV system on the  $^3\text{He}$  STM is a series of inter-connected chambers that facilitate sample and tip insertion, treatment and transport to the STM head. This part can be divided into 3 chambers – a load lock, a preparation and an exchange chamber.

Samples and STM tips are introduced from the ambient conditions to the system via the smallest chamber, the load lock, which is directly connected to a turbo pump and can achieve pressure of  $5 \times 10^{-10}$  mbar.

3

Next, they are transferred to the preparation chamber where they undergo cleaning treatment prior to being transferred into the STM. The preparation chamber is equipped with an ion gun for ion sputtering of the sample surface and a heater stage for the subsequent electron-beam (e-beam) annealing. Additional modules are added to this chamber. For cleaning the metal crystal surface (Cu(100) and  $\text{Cu}_3\text{Au}(100)$ ), an argon (Ar) bottle is installed; for deposition of different insulating layers onto clean metal substrates, we attach a nitrogen ( $\text{N}_2$ ) bottle (for forming copper-nitride on Cu(100) and  $\text{Cu}_3\text{Au}(100)$ ) and insert a copper(II)-chloride ( $\text{CuCl}_2$ ) crucible (for forming Cl-reconstructed Cu(111)). The purity of the gases introduced to this chamber is checked by a residual gas analyzer. The chamber also contains an additional heater stage for e-beam annealing of the tip. Treatment of the PtIr tip consists of heating up its apex by bringing it in a millimeter proximity to the heater filament. This being the chamber where the samples and the tips are prepared for the STM head, it is crucial to keep the pressure as low as possible. Therefore, this chamber is pumped by both a turbo pump (via the load lock) and an ion pump connected directly below it which ensures pressures as low as  $7 \times 10^{-11}$  mbar.

Once the sample or the tip have been properly cleaned, they are transferred to the exchange chamber. This is a chamber connecting the preparation chamber and the cryostat part of the system, located directly above the latter. This is where magnetic atom evaporation takes place (more on this in 3.2) and this chamber has two evaporators attached, each with 3 crucibles, allowing for storing six different chemical elements simultaneously. Like the preparation chamber, this chamber requires strict vacuum conditions so it has its own ion pump but also a titanium sublimation pump (TSP) which ensures pressures of  $2 \times 10^{-10}$  mbar. This chamber, like the rest of the vacuum chamber system, is at room temperature and isolated from the cryogenic part by two thermal shields. The chamber system described is equipped with three magnetically driven manipulation (transfer) sticks serving as transportation vehicles between the load lock at one end and STM head at the other and three storage stages, one per each chamber.

#### 3.1.2. JT STM

The JT STM, shown in Fig. 3.2, can be divided in a similar fashion as the  $^3\text{He}$  STM – the STM head, cryogenic part and the vacuum chamber part. In the remainder of this section we will point out the main technical features of this system.

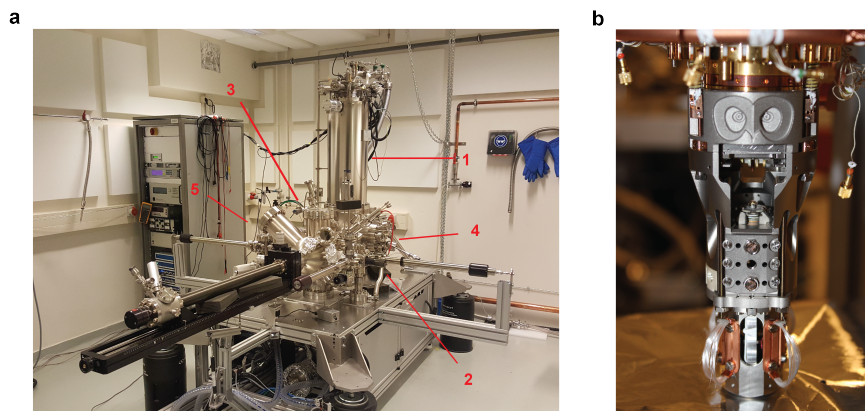


Figure 3.2: **SPECS Joule-Thomson STM with UHV system.** **a** Externally visible part of the experimental set-up with main parts numbered as: 1 – cryostat, 2 – load lock, 3 – preparation chamber, 4 – JT chamber, 5 – molecular chamber. The system is supported by a floating table sitting on 4 air legs. **b** STM head with an opening revealing an empty sample stage on the top and a tip stage at the bottom.

### STM HEAD

The STM head is suspended in the JT chamber, a UHV chamber in the centre of which the cryostat resides. The tip and the sample stage are aligned vertically, with the tip at the bottom. As mentioned, sample and tip insertion is performed with visual access and the STM head in a non-suspended (clamped) position. Coarse motion (cm range) of the sample stage and the tip is handled by a piezo motor and fine movements (nm– $\mu\text{m}$  range) of the tip in all three directions are controlled by a piezo tube. The scan range at 1 K on this system is  $4.2 \times 4.2 \mu\text{m}^2$ . This system, like the  $^3\text{He}$  system, is fixed to a floating table with 4 air legs, with the difference of the cryostat (with the STM head) sitting on top of the table here.

### CRYOSTAT

The cryostat is composed of two hollow concentric containers, the outer of which is filled with liquid  $\text{N}_2$ , giving access to a stable regime at 77 K, and the inner one filled with liquid  $^4\text{He}$ , giving access to a stable regime at 4 K. The STM head, located below the cryostat, is connected to the cryogenic system via a thermal shortcut. To reach 1 K, the lowest accessible temperature on this system, this shortcut needs to be broken and high pressure  $^4\text{He}$  gas ( $\sim$  bar) is introduced to the JT pot, located in the vicinity of the sample stage, where it cools down by expansion based on the Joule-Thomson principle [100]. The time limiting factor for performing continuous measurements at low temperature is the liquid  $\text{N}_2$  lifetime which amounts to  $\sim$  48 h (this is still a factor of 2 better compared to the  $^3\text{He}$  system); liquid  $^4\text{He}$  holds for  $\sim$  72 h on this system. The microscope can be operated at room temperature as well.

A split-coil superconducting magnet located below the cryostat surrounds the STM head and provides up to 3 T field out of the sample plane.

### UHV CHAMBERS

The vacuum chamber system on JT STM setup counts one preparation chamber more compared to the  $^3\text{He}$  STM. This chamber is equipped with three crucibles and is used exclusively for evaporation of copper-chloride and other molecules. As emphasized already, an additional evaporator in the JT chamber is directly attached to the STM chamber, with a Co rod inside. In this way, we can keep the main preparation chamber, where we clean the metal substrates (by Ar sputtering and e-beam annealing), free of additional contamination. However, additional evaporation modules, if needed, can be installed onto the main preparation chamber. The pump distribution and lowest pressures achievable per chamber are as follows: 1 turbo pump for the load lock ( $\sim 5 \times 10^{-8}$  mbar); 1 turbo pump + 1 ion pump + 1 TSP for the main preparation chamber ( $\sim 5 \times 10^{-10}$  mbar); 1 turbo pump + 1 ion pump for the second (smaller) preparation chamber ( $\sim 1 \times 10^{-8}$  mbar); 1 ion pump + 1 TSP for the JT chamber ( $\sim 7 \times 10^{-11}$  mbar).

A number of storage positions for sample/tip holders (15 in total) distributed throughout the UHV chamber system together with a relatively simple and visually accessible sample/tip switching at the STM stage makes this system suitable for a variety of applications.

## 3.2. SAMPLE PREPARATION

In this section we will discuss in detail the two stages comprising the preparation of our samples. First, we will explain how we obtain a clean metal substrate after introducing it from ambient conditions into our UHV system (3.2.1) followed by recipes for different insulating layers we deposit on such clean substrates (3.2.2). This is how we develop a working surface for our experiments on metal substrates. Once the proper surface is obtained, magnetic atom/molecule evaporation is performed. The technical details of this part of the sample preparation for different substrate/atom(molecule) combinations are given in 3.2.3.

### 3.2.1. METAL SUBSTRATES

After introducing the metal substrate into our system, we need to ensure all the water, nitrogen and other contaminants from the air are taken off the sample. To this end, in the preparation chamber we heat up the sample and its holder to  $\sim 600^\circ\text{C}$  for  $\sim 1 - 2$  h by e-beam heating. In addition to this, the surface of the sample undergoes several rounds of Ar sputtering. After sputtering, the surface is left with fewer impurities but more roughness. Therefore, we need to expose the crystal to a thermal treatment which results into surface reconstruction in a form of flat, clean and preferably large plateaus. Typically, the Ar sputtering time amounts to a total of 1 h and the annealing to 6 h after the sample is first introduced into UHV, with the ratio of sputtering/annealing time decreasing with every preparation round. After preparing the metal surface (typically 5 – 10 sputtering and annealing cycles), its quality is checked by means of topographic STM imaging.

### 3.2.2. THIN INSULATING LAYERS ON METAL CRYSTALS

Here we will give details on the three types of thin insulating layers we deposited onto single metal crystals discussed in the previous section.

Copper-nitride ( $\text{Cu}_2\text{N}$ ) reconstructions on both  $\text{Cu}(100)$  and  $\text{Cu}_3\text{Au}$  were obtained in-situ in the preparation chamber of our  $^3\text{He}$  STM system. For obtaining a monolayer of  $\text{Cu}_2\text{N}$  we performed several cycles of sputtering of  $\text{N}_2$  followed by e-beam annealing. Details on the nitride-reconstructed  $\text{Cu}(100)$  and  $\text{Cu}_3\text{Au}(100)$  preparation will be presented in 4.1 and 4.2.

Surface of Cl-reconstructed  $\text{Cu}(111)$  crystal was obtained in our JT STM system and by means of  $\text{CuCl}_2$  thermal evaporation. This was done in a small chamber dedicated to thermal evaporation of different molecules onto our metal substrates after they are cleaned by Ar sputtering in the preparation chamber. Details on the Cl-reconstructed  $\text{Cu}(111)$  preparation together with the resulting monolayer coverages will be presented in 4.3.

After the last preparation cycle (ending with e-beam annealing), all crystals are kept at room temperature in the preparation chamber for at least 20 min before being transferred onto at a cold stage (on the JT system, first at the liquid nitrogen shield stage at 77K for additional 20 min and only then onto the STM head; on  $^3\text{He}$  STM, directly onto the STM head from the preparation chamber) to facilitate a more gradual cooldown.

### 3.2.3. DEPOSITION OF MAGNETIC ATOMS

Once the required insulating layer (copper-nitride or chlorine in this thesis) is found on top of a metal crystal –  $\text{Cu}(100)$ ,  $\text{Cu}(111)$  or  $\text{Cu}_3\text{Au}(100)$  – magnetic atoms (Co in this thesis) are deposited. The  $^3\text{He}$  STM is equipped with a Knudsen cell evaporator containing 6 crucibles, allowing for thermal deposition of 6 different elements whereas JT system has only one Co rod evaporator that makes use of e-beam heating to evaporate Co atoms. For obtaining a surface with individual adatoms and prevent cluster formation, one should ideally perform the evaporation onto the cold sample.

In the  $^3\text{He}$  system, the STM head is immersed in the cryostat leaving no other option for the magnetic metal adatom evaporation to take place anywhere but outside the STM head. This is done in the exchange chamber located above the cryostat. We ought to ensure a minimum time delay between the atom evaporation onto the sample and the sample insertion into the sample stage located inside the cryostat. In this way we reduce the effect of heating up the sample during evaporation and minimize thermal motion of the atoms once on surface. The transfer is done via a room temperature transfer stick approx. 1.5 m long. To lessen the inevitable effect of warming up the sample during this transfer, we pre-cool the long transfer stick on two cooling stages (1 K pot stage and  $^3\text{He}$  pot stage) of the cryostat before executing the sample transfer. Nevertheless, this results in a sample temperature rise of up to at least 60 K during the magnetic adatom evaporation.

In the JT system there are no constraints of this type as this system is built for cold adatom evaporation. This is achieved by having an e-beam evaporator directly attached to the STM chamber, so that the evaporation can take place while the sample is inside the STM head and, hence, cold. The temperature of the sample rises up to  $\leq 10$  K during the evaporation.

### 3.3. STS TECHNIQUES

STM has been primarily used as an imaging tool reproducing the corrugation surface profile of conductive samples. When working in a constant current mode, the electronic feedback regulates the tip height relative to the sample surface as to ensure a constant current of tunnelling electrons between the two while the tip is moving in the plane of the sample. The number of electrons tunnelling between the tip and the sample per second (tunnelling current) gives a measure for the tip-sample distance (tip height). If the tunneling current increases, the feedback loop is triggered to pull the tip away from the sample as to adjust the current to its pre-set value. In this way, maps of constant tunneling current are made and the  $Z$ -signal, representing the tip movement perpendicular to the sample plane, recorded. This tip height profile as a function of the lateral components  $Z(X, Y)$  is what we refer to as the STM topographic image. The tunnelling current, starting from Bardeen's perturbation theory [101], is found to depend on the tip-surface separation  $z$  as [102, 103]:

$$I \propto e^{-cz}.$$

This exponential dependence on the tip-sample distance gives rise to a potential for a surface corrugation reconstruction with atomic resolution.

The STM topographic image does not contain information only about the corrugation profile of the surface. More generally, STM is a tool that maps local density of surface states of conducting samples. The local density of states is energy dependent and, therefore, set by the tip-sample voltage. An STM image obtained as explained above contains information about both the corrugation surface profile and its surface states at a particular energy (tip-sample bias). This explains why insulating areas scanned together with conductive areas on the same surface plateau appear lower in topography compared to conductive areas in certain voltage ranges.

If STM is used in constant height mode, feedback is switched off, so that the tip is kept at the same height w.r.t. to the sample and current is recorded instead. This produces current maps  $I(X, Y)$  of the area scanned with the STM tip. This is a less common operational mode, as the tip is not protected from unwanted sample contact which is a problem for corrugation- and cleanness-compromised samples.

In this section, however, we focus on spectroscopy techniques one can perform with STM. We present two most common scanning tunnelling spectroscopy (STS) techniques that are also used in this thesis. The first one, the inelastic electron tunnelling spectroscopy (IETS), provides information on the magnetic state of the atom or atomic structure by identifying energy and intensity of spin excitations in a range of voltages (3.3.1) while the second one, the spin-polarized (SP-) STM, can be used two-fold, namely as an imaging tool providing spin-contrast directly observed in topographies, but also as a spectroscopy tool unfolding the entire spectral range of the examined object through SP-IETS (3.3.2).

### 3.3.1. INELASTIC ELECTRON TUNNELLING SPECTROSCOPY

Developed decades ago and used as a technique for detection of vibrational modes of molecules buried inside planar metal-insulator-metal junctions [104], inelastic electron tunnelling spectroscopy (IETS) has been extensively applied to many surface science problems, such as chemical identification, bonding configuration, adsorption and catalysis of surface adsorbents [105]. In addition to chemistry and structural studies, the technique became an irreplaceable spectroscopy tool for studies on electronic properties of both surfaces and surface adsorbents. Optical spectroscopy techniques, such as infrared and Raman spectroscopy, infer properties at the molecular or atomic level by measuring average properties of large ensembles of atoms and molecules (typically  $> 10^3$ ) [105]. STM-IETS, on the other hand, utilizes the atomic imaging resolution of STM and its ability to modify position of surface-adsorbed species, enabled isolating and probing single molecules and atoms in order to get insight into their structural, electronic and magnetic properties. Possessing control over geometry and dimensions of the system while being able to probe electronically any part of the system with atomic precision, this combination of techniques can be crucial in understanding how properties of macroscale materials develop as a function of size.

In this thesis we will focus on a particular system of magnetic  $3d$  adatoms on solid surfaces and we will use IETS to study their spin states. We will look at spin states of individual adatoms and atomic chains built out of such atoms via STM manipulation.

#### WORKING PRINCIPLE OF IETS

A simplified energy diagram behind this all-electronic measurement technique is depicted in Fig. 3.1. An object with discrete energy levels whose properties are to be determined is placed between two metal electrodes separated by a thin insulator (a quantum mechanical object in a tunnel junction). In our case, this corresponds to a single adatom in a vacuum barrier positioned between a metallic STM tip and a metal substrate.

As the voltage between the tip and the substrate is swept, the two electrodes are kept at a fixed distance and the current of electrons tunnelling between them is measured. For small voltages, this current is a result of elastic tunnelling which keeps the adatom in its ground state as the energy of the tunnelling electrons is smaller than the adatom's excitation energy,  $\Delta E$ . When a voltage threshold for the adatom to be excited from its ground state is reached:

$$V_{\text{th}} = \Delta E / e,$$

the adatom is brought to its excited state causing the tunnelling electron to lose  $\Delta E$  of its energy before reaching the end electrode. These tunnelling electrons that lose a part of their energy are responsible for opening up a new channel of conduction – the inelastic channel – which reflects in increased tunnelling current for voltages  $V > V_{\text{th}}$ . In the  $dI/dV$  curve, this spectroscopy point is marked by the appearance of a step. Direction of the tunnelling electrons (tip to sample or vice versa) is irrelevant for the adatom excitation, as long as  $|V| > V_{\text{th}}$ , which results in IETS steps being symmetric around  $V = 0$ .

This current increase due to inelastic channel opening is detected with a lock-in detection scheme where, in addition to a DC voltage, an AC voltage is sent and the lock-in signal, which in turn is proportional to  $dI/dV$ , detected [105].

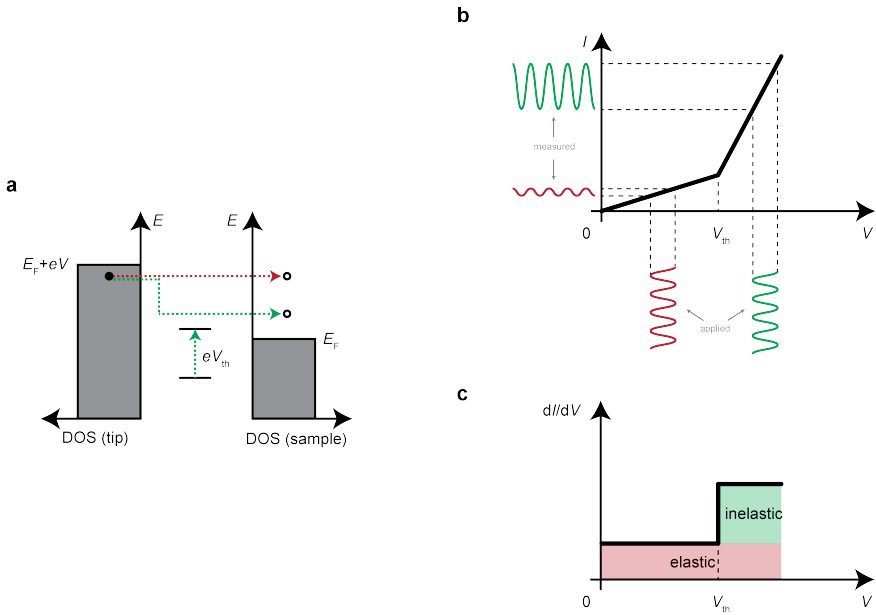


Figure 3.3: **IETS – principle and measurement.** **a** Energy diagram depicting continuous density of states (DOS) of two electrodes, separated by a high barrier, with a voltage difference  $V$ . Inside the barrier, a two-level system with energy separation  $eV_{th}$ . As long as the voltage between electrodes is below  $V_{th}$ , only elastic channel of tunneling is open. Once  $V > V_{th}$ , additional, inelastic channel opens up, as a consequence of energy exchange with the localized discrete system. **b** Measurement of the IETS signal. A small modulation (AC) is added to the DC voltage signal, and the AC component of the resulting tunneling current extracted by lock-in detection. The amplitude of the AC component depends on the  $I(V)$  slope at which modulation is applied and measured. **c** Corresponding  $dI/dV$  signal with a step at  $V = V_{th}$ , marking the onset of additional channel for electron tunneling (in **b**), this is marked by a change in slope in the  $I(V)$  curve).

### IETS STEP ANALYSIS

Analysis of  $dI/dV$  steps provides information on the low-energy spin states of magnetic adatoms. Three step features are to be considered: position, width and height.

Step position, as explained above, corresponds to the energy an adatom requires to reach a certain excited state where its spin is pointing along a different direction. For a single adatom at 0 magnetic field this number translates into a quantitative measure of magnetic anisotropy the adatom experiences on a surface it sits on. The higher the step position, the more stable the adatom's ground spin state.

The width of the IETS step includes the intrinsic broadening of the line but also broadening due to experimental conditions – temperature and modulation voltage for the lock-in signal. Intrinsic broadening ( $W_{intrinsic}$ ) is a signature of a lifetime of the excited state – the shorter lived the excited state, the more smeared the step will be. For magnetic adatoms on surfaces, the spin state lifetime is related to the level of decoupling from the metallic substrate. Therefore, the choice of the appropriate decoupling (insulating) layer and its thickness is crucial for resolving low-energy excitation steps such as spin transitions

that occur typically in the meV energy range. The layer cannot be too thick as to allow for detectable electron tunnelling to occur, but it should not be too thin either, as that makes for a poor shield against conduction electrons from the substrate that scatter on the spin of the adatom and change its spin state. Thermal broadening at a temperature  $T$  of the Fermi distribution function is reflected in a linewidth broadening (full width at half maximum) as

$$W_{\text{thermal}} = 5.4k_{\text{B}}T/e$$

( $k_{\text{B}}$  – Boltzmann constant) [106, 107].

This yields the following limitations on energy resolutions on our STM systems – for  $^3\text{He}$  STM ( $T_{\text{base}} = 330$  mK) 0.2 meV and for JT STM ( $T_{\text{base}} = 1.2$  K) 0.6 meV. As mentioned, spin excitations in magnetic adatoms typically occur on an energy scale of a few meV or, extraordinarily, tens of meV [9], and therefore this resolution is sufficient for our experiments. The modulation voltage necessary for reconstruction of the  $dI/dV$  signal also causes linewidth broadening and this one is quantified (FWHM) as

$$W_{\text{mod}} = 1.7V_{\text{rms}}$$

with  $V_{\text{rms}}$  being the rms value of the modulation voltage. To measure an IETS spectrum with a sufficient signal to noise ratio, we apply  $V_{\text{rms}} = (70 - 110)$   $\mu\text{V}$  which identifies the temperature as the dominant resolution limiting source. Experimentally observed spectral line broadening is given with the formula combining the three effects [108]:

$$W_{\text{total}} = \sqrt{W_{\text{intrinsic}}^2 + W_{\text{thermal}}^2 + W_{\text{mod}}^2}$$

### 3.3.2. SPIN POLARIZED STM

Up until now we neglected the spin aspect of the electrons on the tip and discussed imaging and spectroscopy assuming identical density of states (DOS) for spin up and spin down carriers, i.e. no spin polarization of the tip. In this section we discuss the case of that carrier balance being broken at the tip site which consequently accounts for a non-equilibrium DOS for spin up and spin down electrons at the Fermi level of the tip [109–112]. This imbalance causes the magnitude of the tunnelling current between the tip and the surface adatom to vary depending on the relative orientation between the spin of the (apex of the) tip and the spin of the adatom. Tunnelling current is proportional to the product of DOS of electrons at the Fermi level in initial ( $N_i$ ) and final ( $N_f$ ) states. Therefore, when the spins of the tip (apex) and the adatom are pointing in the same direction, the current is defined by the sum:

$$I_{\text{p}} \propto N_i^{\uparrow}N_f^{\uparrow} + N_i^{\downarrow}N_f^{\downarrow},$$

whereas for the antiparallel orientation of the two, the following holds:

$$I_{\text{ap}} \propto N_i^{\uparrow}N_f^{\downarrow} + N_i^{\downarrow}N_f^{\uparrow}.$$

A more general dependence on relative orientation is captured in a following manner:

$$I = I_0(1 + P_i P_f \cos\delta)$$

where  $\delta$  is the angle difference between the spin orientations of the tip and adatom and  $P$  is the relative population for spin up electrons:

$$P = (N^\uparrow - N^\downarrow)/(N^\uparrow + N^\downarrow).$$

Defined in this way,  $I_0$  is the tunnelling current of the non-SP tip which.

## 3

## SP-TIP

Creating a spin-polarized tip apex for STM imaging and spectroscopy can be achieved either ex-situ or in-situ [112]. For an extensive review on SP-tip preparation, reader is referred to [112]. We will focus on the in-situ preparation of nonmagnetic tips with magnetic apex in the remainder of this section.

This can be achieved in several ways – by using voltage pulses to facilitate a material flow from the substrate towards the tip [113] or by indenting the tip into a magnetic substrate [114]. Both methods leave the tip apex covered with magnetic atoms. However, control over the apex size and shape is poor.

A reversible in-situ preparation method of SP-tips emerged with mastering STM manipulation of magnetic adatoms – namely, one makes the tip spin-polarized by attaching one or few magnetic adatoms from the surface onto the non-magnetic tip. Even though the overall shape of the tip apex still cannot be determined, this method of generating SP-tips allows for an atomically precise control over the size of the magnetic cluster attached to the apex of the tip and is proven to generate a tip apex that is paramagnetic [92, 115]. Once external field is applied, the spin states of the adatom or the atomic cluster on the apex of the tip split in energy due to Zeeman effect, i.e. the apex of the tip orients itself along the field and is able to map the spin component of the surface adatoms along the field direction. This effect can be detected already for fields as low as  $\sim 200$  mT as reported in e.g. [25].

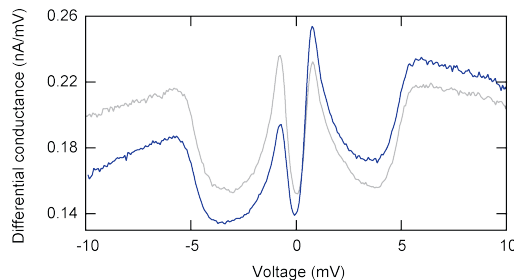
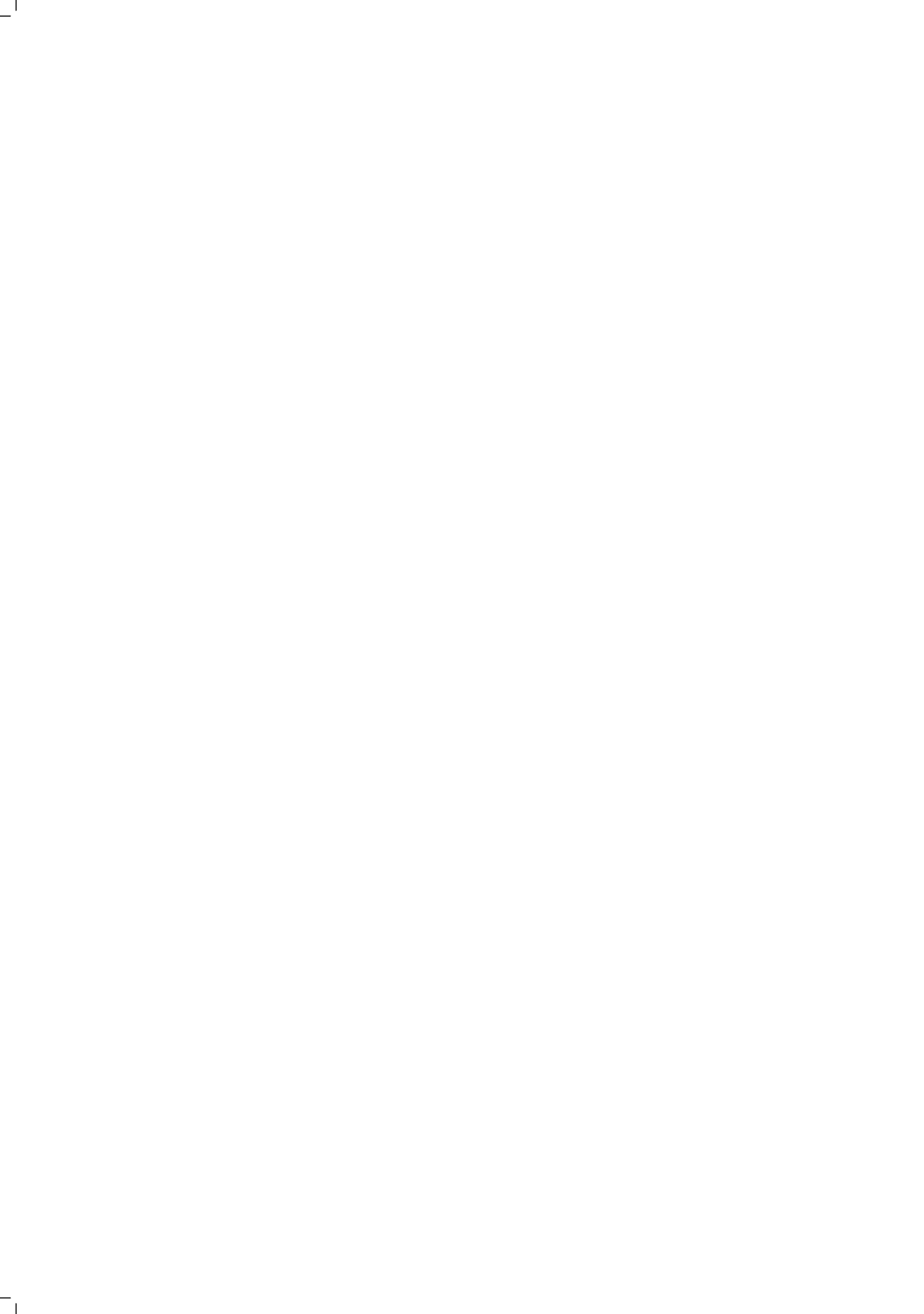


Figure 3.4: **SP-IETS on a single Co atom.** IETS spectra on a single Co atom on  $\text{Cu}_2\text{N}/\text{Cu}(100)$  in a 3 T magnetic field oriented perpendicular to the surface, taken with the same spin-polarized tip as used in Fig. 5.7 (blue) and with a spin-unpolarized tip (grey).

For our SP-IETS experiments on Co adatoms (presented in section 5.5), we used PtIr tips created by STM vertical manipulation by attaching one or several Co to the apex of the STM tip. As will be explained in section 4.1.2, at zero field, a low voltage IETS spectrum taken with a non-SP tip on a Co adatom on this surface presents a Kondo peak at zero-bias and an anisotropy step at 5 mV (grey line in Fig. 3.4). To demonstrate that we have a SP-tip, we will analyze the Kondo state of the Co adatom on  $\text{Cu}_2\text{N}/\text{Cu}(100)$  [3, 92].

At zero field this state is represented by a pronounced peak at zero-bias. At finite field Kondo feature is split into two peaks which appear symmetric in IETS taken with a spin-averaging tip (non-SP tip). This symmetry in the split Kondo state indicates equal probability of tunnelling for spin-up and spin-down electrons. Upon attaching several Co adatoms onto the tip and repeating the measurement on a single Co adatom, we observe a higher intensity peak in the split Kondo state for positive voltages. This indicates a tip that is spin-polarized and in the direction opposing the external field, in contrast to what is expected [116] and previously reported in experiment [117]. This can be explained by the exchange forces within the tip that leave the apex with higher DOS for spin-down electrons (spin-up is conventionally defined to be in the direction of external field).



# 4

## PLATFORMS FOR BUILDING ATOMIC STRUCTURES

*In this thesis, we present studies on magnetic adatoms separated by an insulating thin layer from a conductive substrate. The key to a successful signal detection in such an STM measurement lies in the proper choice of the insulating layer between the STM tip and the conductive substrate. This layer serves as a shield protecting the surface adatom from conduction electrons from the substrate that limit the spin lifetimes of the adatom probed by the tunnelling electrons. On the other hand, the layer has to be thin enough to allow for the detectable tunnelling current to flow through. The compromise between the two opposing requirements is typically found in a formation of a single insulating monolayer atop a metal crystal substrate. In this chapter we present two types of monolayers with distinct geometries employed as working platforms in STM-IETS experiments on Co adatoms presented in the latter chapters of this thesis. The first one –  $\text{Cu}_2\text{N}/\text{Cu}(100)$  – was used for assembling Co chains along two distinct directions along which they behave differently due to the difference in intra-chain coupling. Here we present experiments and analysis on Co dimers along those two directions used as chain building blocks in subsequent chapters. An inherent problem of lattice mismatch between  $\text{Cu}_2\text{N}$  and  $\text{Cu}(100)$  surface reconstruction leads to a limitation in the size of nitride islands and therefore size of our magnetic systems, a problem overcome by replacing the  $\text{Cu}(100)$  crystal with  $\text{Cu}_3\text{Au}(100)$ , an initial study on which is presented here as well. The second type of monolayer discussed here – Cl-reconstructed  $\text{Cu}(111)$  – promises to be a building platform for atomic structures with unmatched sizes and its hexagonal geometry could potentially serve as a viable platform for building frustrated spin lattices.*

---

Parts of this chapter describe work published as a journal article [63] and work in preparation for journal submission by **R. Toskovic**, M.C. Martínez Velarte, J. Girovsky, M. Kokken, J.W. González<sup>§</sup>, F. Delgado<sup>†</sup>, and A.F. Otte. Theory results supporting the part on Cl-reconstructed  $\text{Cu}(111)$  were obtained by J.W. González<sup>§</sup> and F. Delgado<sup>†</sup>.

<sup>§</sup> Materials Physics Center, San Sebastián, Spain

<sup>†</sup> Departamento de Física, Universidad de La Laguna, San Cristóbal de La Laguna, Spain

## 4.1. COPPER-NITRIDE ON CU(100)

This part of the chapter focuses mainly on a working surface that is widely explored by the magnetic adatom STM community –  $c(2 \times 2)$  nitrogen reconstruction on copper(100) (here referred to as  $\text{Cu}_2\text{N}/\text{Cu}(100)$ ) [118]. We start with experimental conditions behind its formation and the resulting geometry and end by motivating the need for a different substrate for growth of copper-nitride –  $\text{Cu}_3\text{Au}(100)$  (4.1.1). In 4.1.2 we describe a case study of a single Co adatom on  $\text{Cu}_2\text{N}/\text{Cu}(100)$  showing vertical STM manipulation and IETS spectroscopy, followed by a study on inter-atomic coupling in Co dimers in different configurations (4.1.3). Two of these configurations will become building blocks for longer atomic chains discussed in chapters 5 and 6.

### 4

#### 4.1.1. COPPER-NITRIDE RECONSTRUCTION

Copper-nitride ( $\text{Cu}_2\text{N}$ ) on Cu(100) crystal has proved to be a rewarding working surface for atomic magnetism investigations for over 10 years now. The system was successfully utilized in numerous magnetic adatom studies, including adatom anisotropy [8, 61, 62], Kondo coupling of the adatom to substrate electrons [3, 117, 119], spin-spin exchange coupling between adatoms [5, 22, 63], spin waves detection [25] and even unravelling potential for building stable bits [32] and control over them [6, 115].

A monolayer of  $\text{Cu}_2\text{N}$  is formed by nitrogen ( $\text{N}_2$ ) sputtering of Cu(100) surface (gentler than Ar sputtering used for cleaning the crystal surface) and subsequent annealing. Typically, sputtering is done at a  $\text{N}_2$  partial pressure of  $\sim 1 \times 10^{-5}$  mbar for  $\sim 40 - 50$  s and later annealed for 1–20 min (this difference in annealing time was not found to influence the reconstruction) at  $\sim 400^\circ\text{C}$ .

DFT studies show nitrogen atoms forming covalent bonds with the neighbouring Cu atoms, forming a 2D covalent network on top of Cu(100) [61]. A clean Cu(100) crystal surface can be readily obtained with plateaus of hundreds of nanometers wide, as verified in STM topography (Fig. 4.1a). However, due to the lattice mismatch between  $\text{Cu}_2\text{N}$  and Cu(100) surfaces, a 3% compressive stress arises in the nitride layer. This results in nitride appearing in a form of rectangular islands of typical sizes  $\sim 5 - 10$  nm with copper areas in between as can be seen in Fig. 4.1b.

This results in a  $\text{Cu}_2\text{N}$  surface reconstruction shown in Fig. 4.2a. Two directions can be distinguished in this surface reconstruction – one direction containing a nitrogen atom between every two copper atoms (N direction) and another direction with no nitrogen atoms in-between the copper atoms (vacancy direction). Choice of surface direction for adatom assembly into atomic chains results in structures with distinct properties, as will be shown on the example of cobalt adatoms in section 4.1.3 and chapters 5 and 6.

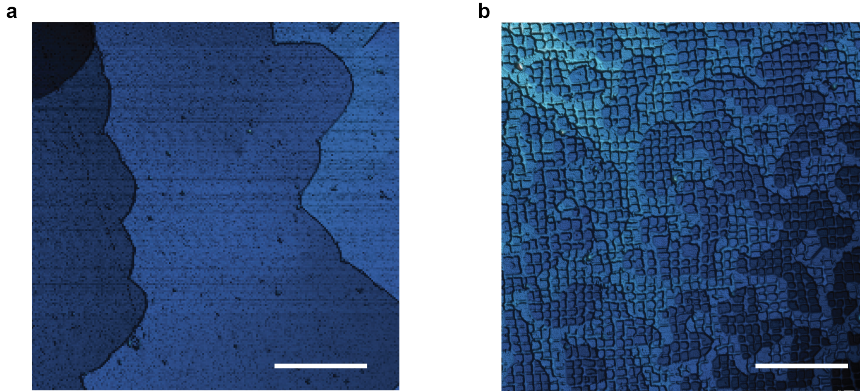


Figure 4.1: **Copper-nitride on Cu(100).** **a** STM topography of a clean Cu(100) crystal surface. A terrace of  $\sim 200$  nm wide can be seen. Imaging settings:  $I = 5$  pA,  $V = 15$  mV,  $T = 1.5$  K; scale bar 100 nm. **b** STM topography of copper-nitride reconstruction of Cu(100) surface after  $N_2$  sputtering. Nitride islands with predominantly rectangular shapes and typical sizes  $\sim 5 \times 5$  nm<sup>2</sup> can be seen. Imaging settings:  $I = 5$  pA,  $V = 15$  mV,  $T = 1.5$  K; scale bar 100 nm.

#### 4.1.2. CO ADATOMS ON COPPER-NITRIDE ON Cu(100) – SPECTROSCOPY AND MANIPULATION

An IETS spectrum of a Co adatom on  $Cu_2N/Cu(100)$  at 330 mK is shown in Fig. 4.2b. The zero field spectrum (red curve in Fig. 4.2b) is characterized by two features: a pronounced zero-bias peak, marking Kondo effect the adatom exhibits on this surface (with a Kondo temperature of  $T_K = 2.6 \pm 0.2$  K), and a symmetric IETS step at  $\sim 5.5$  mV, as a consequence of the anisotropy the adatom's spin experiences when adsorbed onto this surface [3, 120].

Co adatom is a spin-3/2 system. Kramers' theorem prevents the ground state of non-integer spins from being non-degenerate and the hard-axis anisotropy makes the  $\pm 3/2$  states to be higher in energy compared to  $\pm 1/2$  ones. This results in a zero field energy diagram of a Co adatom being characterized by a doubly degenerate ground state composed of  $\pm 1/2$  states and a doubly degenerate first excited state composed of  $\pm 3/2$  states (here, we neglect transverse anisotropy which, in any case, does not break the ground state degeneracy ensured by Kramers' theorem).

The zero-bias peak corresponds to Kondo screening by the substrate conduction electrons which, by scattering on the Co adatom, give rise the transitions between  $-1/2$  and  $+1/2$  degenerate ground states resulting in an increased density of states at the Fermi level [1, 3, 121–123]. Upon applying a magnetic field Kondo peak splits into two smaller peaks (blue curve in Fig. 4.2b) that grow in energy with increasing field. This comes from splitting of  $\pm 1/2$  states in field due to Zeeman effect. The rate at which the two states split is determined by the field axis.

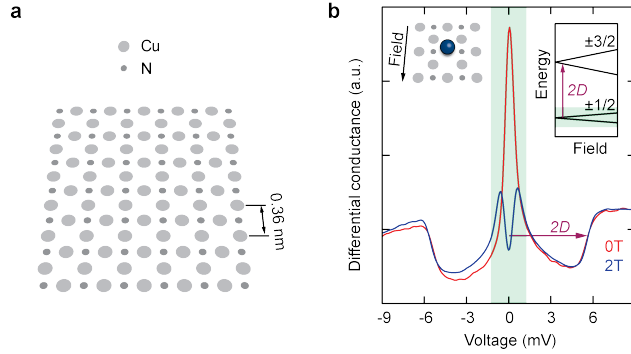


Figure 4.2: **Co adatom on  $\text{Cu}_2\text{N}/\text{Cu}(100)$ .** **a** Schematics of a  $\text{Cu}_2\text{N}$  reconstruction on a  $\text{Cu}(100)$  crystal surface. **b** IETS spectra taken on a single Co atom on  $\text{Cu}_2\text{N}$  at 0 T and 2 T applied along the hard axis. Left inset: atomic arrangement near the Co atom. Right inset: energy diagram indicating the separation between the  $\pm 1/2$  and  $\pm 3/2$  doublets.

Transitions from the  $\pm 1/2$  to the higher lying  $\pm 3/2$  states are seen as an IETS step at  $2D = 5.5$  meV, where  $D$  is the hard-axis anisotropy ( $D > 0$ ) and is found to be along the N-vacancy direction (hollow direction). Similarly to the Kondo feature, upon applying field, this anisotropy step also shifts in energy, where the direction and value of the anisotropy step shift are dependent on the field axis [3].

The precise position of Co adatoms on the  $\text{Cu}_2\text{N}/\text{Cu}(100)$  surface is controlled by means of vertical STM manipulation. After thermal evaporation of Co onto  $\text{Cu}_2\text{N}$  surface, in most cases a Co adatom sits on top of a Cu site [124]. Co adatom forms strong covalent bonds with two neighboring N atoms. Due to strong bonding of the adatom to the  $\text{Cu}_2\text{N}$  surface network, lateral manipulation is challenging. Instead, vertical manipulation, discussed next, proved to be a reliable method for Co manipulation on this surface.

First, the STM tip is brought closer to the Co adatom ( $\sim 150$ – $200$  pm) from the tunneling regime to the tip-adatom distance corresponding to 2 nA tunneling current at +20 mV, after which a positive voltage of  $\sim +1.2$  V is applied on the sample side. This causes the Co adatom to break the bonds with two N atoms and gets transferred from the surface onto the tip. The pick-up is presumably, similarly to Fe on the same surface [125], related to the charging effect that takes place when the adatom is embedded into the surface in which some negative charge is transferred to the underlying  $\text{Cu}_2\text{N}$  network leaving the Co adatom positively charged. The charging effect creates a local minimum in energy on the tip side resulting in the adatom pick-up.

After moving the tip to the desired location on the surface, a drop-off can be performed by bringing the tip closer to the surface (a few tens of picometers less compared to the pick-up setting) and subsequently applying a negative voltage (on the sample side) of  $\sim -120$  mV. This creates a local energy minimum on the sample side and the Co adatom is transferred onto the surface.

After the drop-off occurs, the Co adatom initially occupies a position atop a N site. The configuration atop a N site shows no excitations in the low-energy IETS spectra as predicted by DFT and confirmed by STM-IETS. To push it to a (neighboring) Cu atop site, we get  $\sim 50 - 100$  pm closer to the adatom and apply a positive voltage ( $\sim +1.1$  V) in the desired direction. We achieved a good reliability in terms of the hopping direction.

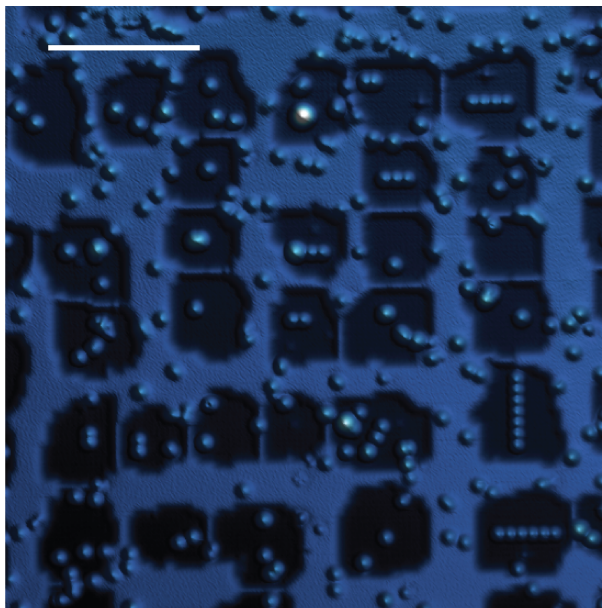


Figure 4.3: **Co chains on  $\text{Cu}_2\text{N}/\text{Cu}(100)$ .** STM topography of Co adatoms on nitride-reconstructed Cu(100) crystal. Co adatoms on both nitride islands and Cu patches can be seen. Artificially constructed Co chains of various lengths can be seen as well (2, 3, 4, 6 and 7 atoms long). Imaging settings:  $I = 5$  pA,  $V = 25$  mV; scale bar 10 nm.

This procedure allows for a reproducible Co adatom manipulation on nitride islands on Cu(100) enabling formation of Co atomic structures of geometry and size defined with sub-nanometer precision. Fig. 4.3 shows several instances of chains built of Co adatoms using the manipulation technique described here.

In the following section we will investigate the simplest multi-atom structures that can be engineered by means of STM manipulation: atomic dimers. We will focus on the influence that sub-nanometer placement differences of a neighboring adatom have on the single Co adatom's low-energy IETS spectrum.

#### 4.1.3. ATOMIC DIMERS – STUDY OF DIFFERENT CONFIGURATIONS

Here we discuss STM built pairs of Co atoms in UHV on a thin insulating  $\text{Cu}_2\text{N}/\text{Cu}(100)$  substrate. By adjusting the relative position and orientation of the atoms on the underlying crystal lattice we are able to tune their exchange interaction strength the sign of which is determined by IETS measurements in transverse magnetic field.

## COUPLING IN CO DIMERS

We modeled our Co dimers using the Hamiltonian presented in chapter 2, given by eq. 2.3, with axes defined as in Fig. 4.4e.

In most of our dimers, the coupling is much smaller than the anisotropy energy ( $|J| \ll \lambda^2 \Lambda_{zz}$ ) which makes for the lowest states of dimers to be dominated by combinations of  $\pm 1/2$  states. Therefore, spin excitations with lowest energies will be the ones between these  $\pm 1/2$  multiplet states – they will be in the order of the spin-spin coupling  $J$ . Spin excitations from this multiplet to higher lying multiplets (which contain also  $\pm 3/2$  states) will be detected at higher energies ( $2\lambda^2 \Lambda_{zz}$ ). Let us take a look at the lowest energy multiplets of the two dimers representative of the two types of coupling – AFM and FM.

### 4

From Fig. 4.4a,b it is evident that both the behaviour at zero field and the evolution in transverse field of the lowest four energy levels depend on the sign of coupling between the two spins.

We compare the zero field energy spectra for the two cases. In both cases the gap between the GS state and the highest excited state in this lowest multiplet amounts to  $4J$ . This excitation is clearly visible in  $dI/dV$  spectra in both dimers (Fig. 4.4c,d). The first point of difference between the two dimers is the gap from the GS to the first excited state – this gap is larger for the AFM case ( $\sim 5/2J$ ) compared to the FM one ( $\sim 3/2J$ ). Due to the small value of coupling for the AFM dimer, this gap is not resolved in the IETS spectrum of the AFM dimer (difference between  $5/2J = 0.55$  meV and  $4J = 0.88$  meV is the at the edge of our IETS sensitivity at 330 mK). This excitation in the FM dimer (with 3.6 times stronger coupling), on the other hand, is clearly visible in its IETS spectrum. In this way, by analyzing the zero field features in IETS spectra of the dimers one can infer both the sign and the strength of coupling between the atoms. However, if  $J$  is too small for the  $3/2J$  and  $5/2J$  to be resolved by the low temperature IETS-STM, one needs to analyze the spectra in presence of field.

We will now take a look at the lowest states' evolution in transverse field for both dimer types. For a dimer with AFM coupling ( $J > 0$ ), the first excitation energy drops until a critical field value  $B_c$  is reached. At this point ground state and first excited state swap and dimer enters a new ground state for  $B > B_c$ . For  $B > B_c$  this ground state is separated by an ever-growing energy gap to the first excited state<sup>1</sup>. For the FM coupled dimer, however, a qualitatively different behavior is expected. Namely, the ground state never crosses any of the higher lying excited states with the increasing field, but only becomes more stable as the field increases (gap to first excited state grows with field).

This provides us with a tool to map the inter-atomic interactions in Co dimers by extracting the coupling values from the measured  $dI/dV$  curves. The result is presented in Fig. 4.4e. In this map we take a center Co atom as a dimer building reference and we mark positions of the second Co atom by a color denoting the coupling sign and the color in-

<sup>1</sup>A complete field evolution, up to 9 T, for an AFM dimer in this geometry can be found in a later chapter, in Fig. 5.4a, where this crossing is evident in  $dI/dV$  maps taken in a range of fields above both atoms of the dimer.

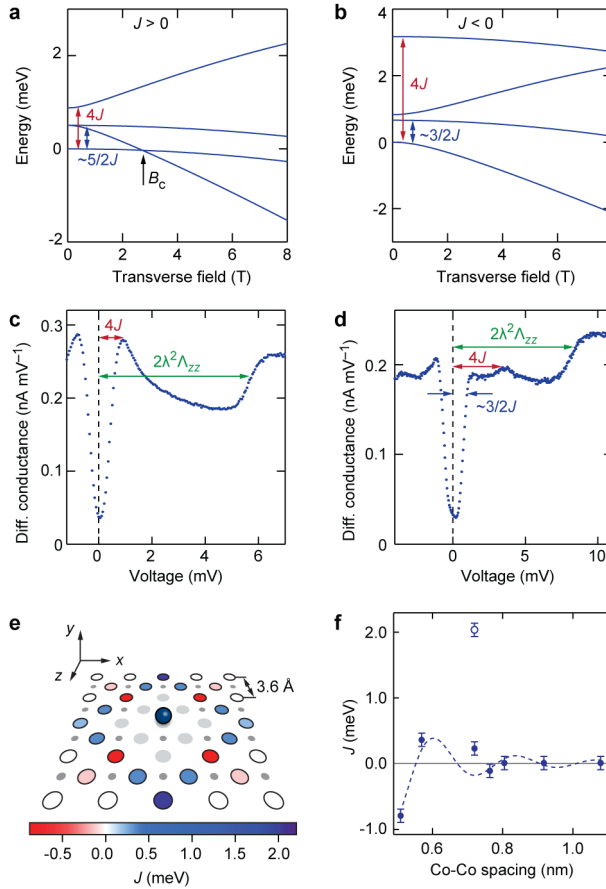


Figure 4.4: **Coupling in Co dimers – sign and strength.** **a, b** Energy diagram in transverse field for two dimer configurations whose IETS spectra are shown in **(c, d)** and represent examples of AFM ( $J > 0$ ) and FM ( $J < 0$ ) coupling respectively. The first two excitation energies accessible in an STM-IETS experiment are labeled in blue and red for both cases as a function of coupling  $J$ . Dimer with AFM coupling is characterized also by a ground state crossing at  $B_c$ . **c, d** IETS spectra taken at 0 field for the two dimers from **(a, b)**. In addition to showing coupling energies from energy diagrams in **(a, b)**, anisotropy energies are indicated as well (green). **e** Colour map showing intra-dimer coupling strength and sign. Values are extracted from fitting the experimental  $dI/dV$  curves. Atom position diagram as follows: blue atom in the center – reference Co adatom; blue and red circles on the surface – Co adatom positions on the  $\text{Cu}_2\text{N}$  surface forming a dimer with the reference adatom with AFM and FM coupling, respectively; light gray circles – Cu positions too close to the reference atom for another Co adatom to be placed by an STM tip and dimer formed; white and small gray circles are Cu and N atoms of the underlying  $\text{Cu}_2\text{N}$  surface (unit cell 0.36 nm), respectively. Coordinate system chosen as:  $z$  is the N direction,  $x$  the vacancy direction and  $y$  the out of plane direction. **f** Coupling strength as a function of adatom spacing in a dimer. For comparative purposes, an isotropic three-dimensional RKKY curve with Fermi wavelength of bulk Cu and horizontal offset of 0.15 nm, corresponding to a phase shift of  $1.3\pi$ , is shown (dashed line). The open circle point corresponds to a  $\{2, 0\}$  dimer which stands out in coupling strength and cannot be accounted for by RKKY coupling only.

tensity denoting the coupling strength. The underlying surface dictates a discrete set of allowed Cu positions (big circles) for the second adatom to be placed atop. Certain Cu positions (gray) are too close to the reference atom for a successful STM manipulation to take place.

We plot the coupling as a function of dimer size (inter-atomic distance as obtained from STM topographies) in Fig. 4.4f. Data points for almost every dimer are reasonably well followed by a simulated curve accounting for isotropic RKKY coupling [126–128] strengthening the proposal of this type of exchange coupling to be dominating in our dimers as was predicted for Co adatoms in theory [60] and also measured for Co adatoms indirectly utilizing Kondo effect [129] and directly for Fe adatoms [33]. We do note that we do not know to what extent this model is applicable to our adatoms as they are separated by an insulating layer of nitride from the conduction electrons of the bulk Cu(100) that mediate this type of interaction. Also, we do not take into account anisotropies of the Fermi surface of the substrate which result in directional RKKY as demonstrated in [130].

The only dimer with a large coupling discrepancy when compared to the isotropic RKKY model of exchange is the  $\{2,0\}$  type<sup>2</sup>. Our proposal is that superexchange plays an important role for this type as this is the only dimer type that has no  $90^\circ$  angles in the path connecting the two adatoms via Co-N and Co-Cu bonds which facilitate this interaction [131, 132].

## MEASUREMENTS ON DIFFERENT DIMER CONFIGURATIONS

Fig. 4.5b-f gives an overview containing every Co dimer type built on this substrate where the coupling was detectable in the IETS spectra (i.e. showing only dimers where spectra of the atoms were different from the single Co case shown in Fig. 4.5a). The spectra are shown together with the simulated curves derived from the Hamiltonian described.

Data are reproduced by a scattering model taking into account interaction of tunnelling electrons with the spin of the adatoms via a scattering term  $\mathbf{S}\cdot\sigma$  where  $\sigma$  corresponds to Pauli matrices for spin-1/2 electrons and  $\mathbf{S}$  to the spin of the adatom. For all the dimers except  $\{2,0\}$  one (Fig. 4.5b-e), spectra are fitted with anisotropy parameters  $\Lambda_{yy}$  and  $\Lambda_{zz}$  varying between  $6.1$  and  $7 \text{ eV}^{-1}$  and  $\Lambda_{xx} = 0$ . On the other hand, instances of dimer  $\{2,0\}$  on this surface are fitted by a variety of values for  $\Lambda_{zz}$ , varying almost by a factor of 2 (with  $\Lambda_{xx} = 0$  and  $\Lambda_{yy} = 6.2 \text{ eV}^{-1}$ ).<sup>3</sup> The instance of  $\{2,0\}$  dimer shown in Fig. 4.5f was fitted with  $\Lambda_{zz} = 2\Lambda_{yy} = 12.7 \text{ eV}^{-1}$ . An overview of all the dimers studied with their corresponding fitting anisotropy parameters can be found in Table 4.1.

The model includes scattering events up to third order in matrix elements [116] and captures not only position of the IETS steps but also additional contribution coming from second and third order processes that give a Kondo-like enhancement in  $dI/dV$  curves at or near the step positions. Within this model, coupling between the spin of the adatom

<sup>2</sup>We label the dimer types with the following notation:  $\{N, \nu\}$ , where  $N$  and  $\nu$  are  $\text{Cu}_2\text{N}$  unit cell multiplication numbers representing relative position of the second Co adatom along N and N-vacancy directions, respectively.

<sup>3</sup>In Chapter 6, where we discuss chains built by extending this dimer type, an overview of different dimer instances of type is shown with the corresponding anisotropy  $\Lambda_{zz}$  parameters (Fig. 6.10).

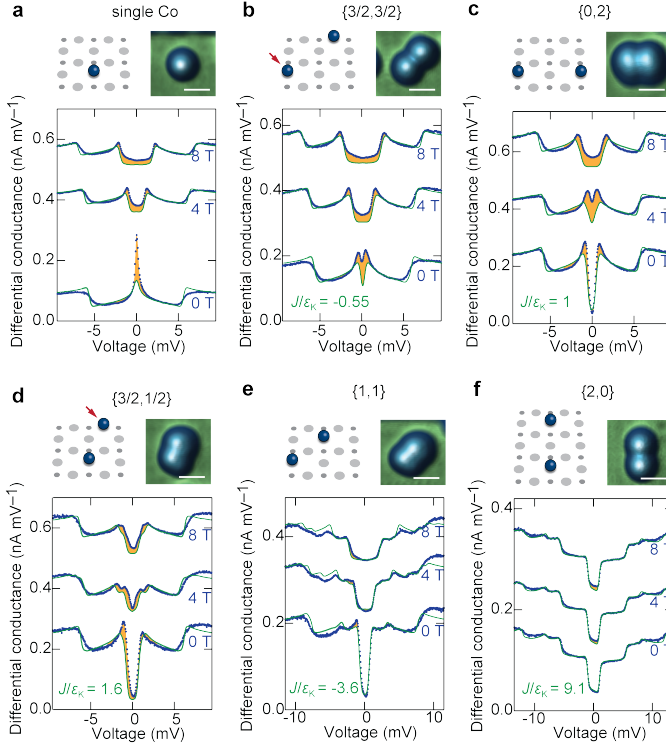


Figure 4.5: **Complete set of Co dimer configurations.** **a-f** Comparison of  $dI/dV$  measurements (blue dots) and simulations (green lines). Panels **(a-f)** are ordered by an increasing value of  $|J/\epsilon_K|$  (indicated in each dimer panel), with  $\epsilon_K = 0.22 \pm 0.02$  meV, at three field values (0 T, 4 T and 8 T) perpendicular to the sample surface. Orange shaded regions represent the difference between the measured and the simulated curves in the voltage range from  $-3$  to  $+3$  mV. Spectra in each panel offset for clarity. IETS performed at 330 mK. A corresponding atomic diagram shown for each type of dimer. Large and small grey circles represent, respectively, Cu and N atoms; the blue spheres the Co atoms. Scale bar in topographic STM images 1 nm. Dimers **(b)** and **(d)** are the only ones in which the spectra differ on the two atoms – the arrows indicate the atom of the dimer whose spectra are shown.

and the conduction electrons is AFM and its strength quantified by an exchange parameter  $J_K \rho_s$ , where  $J_K$  is the Kondo scattering parameter and  $\rho_s$  density of states of sample electrons around the Fermi level. For all dimers with adatom coupling much stronger than the Kondo interaction with substrate electrons, i.e.  $J/\epsilon_K \gg 1$ , the model fits the observed spectra very well (Fig. 4.5e,f). In all simulations,  $J_K \rho_s = 0.15$  was used.

This model still does not faithfully reproduce the intensity of certain spectral features observed in both the single Co atom (Fig. 4.5a) and dimers where  $J/\epsilon_K \gg 1$  does not hold (Fig. 4.5b-d). The reason for this can be found in the model neglecting scattering terms of order higher than 3. These terms could account for emergence of a correlated state resulting in an increase of density of states around Fermi energy and, therefore, increased conductance around zero-bias.

	$J_K\rho_s$	$\Lambda_{xx}$ (eV <sup>-1</sup> )	$\Lambda_{yy}$ (eV <sup>-1</sup> )	$\Lambda_{zz}$ (eV <sup>-1</sup> )	$J$ (meV)	$D$ (meV)	$E$ (meV)	$g_x$	$g_y$	$g_z$
single Co	0.15	0	6.4	6.4	–	2.8	0	2.0	2.3	2.3
{3/2, 3/2}										
atom 1 (marked)	0.15	0	6.3	6.3	0.12	2.8	0	2.0	2.3	2.3
atom 2	0.15	0	6.4	6.2	0.12	2.8	0.04	2.0	2.3	2.3
{0,2}	0.15	0	6.1	6.1	–0.22	2.7	0	2.0	2.3	2.3
{3/2, 1/2}										
atom 1 (marked)	0.15	0	6.2	6.4	–0.35	2.8	0.04	2.0	2.3	2.3
atom 2	0.15	0	7.0	7.0	–0.35	3.1	0	2.0	2.3	2.3
{1,1}	0.15	0	6.1	6.4	0.8	2.8	0.07	2.0	2.3	2.3
{2,0}	0.15	0	6.2	11.2	–2.0	3.8	1.1	2.0	2.3	2.5

Table 4.1: **Fitting parameters for calculated IETS spectra of Co dimers.** Complete set of fitting parameters for simulated IETS spectra of Co dimers presented in Fig. 4.5. Anisotropy parameters –  $\Lambda_{xx}$ ,  $\Lambda_{yy}$  and  $\Lambda_{zz}$  – are used to obtain  $D$ ,  $E$  and  $g_{x,y,z}$  values. Atoms denoted as "marked" correspond to the atoms indicated by red arrows in Fig. 4.5b,d.

4

## 4.2. COPPER-NITRIDE ON Cu<sub>3</sub>Au(100)

In this section we present results on the nitride reconstruction on a copper-gold (100) crystal (Cu<sub>3</sub>Au(100) from now on) (4.2.1) and end the section with preliminary results on single Co adatoms deposited onto it (4.2.2).

### 4.2.1. COPPER-NITRIDE RECONSTRUCTION

Despite its success in STM-IETS studies, a limitation in working on Cu<sub>2</sub>N/Cu(100) surface arises from the relatively small island sizes. These make it difficult to build e.g. atomic chains longer than ~ 10 adatoms with a two Cu<sub>2</sub>N unit cell inter-atomic separation which borders the proximity limit to which one can position an adjacent adatom in a controlled manner on this surface. The size limitation of Cu<sub>2</sub>N islands on Cu(100) could be overcome by using a crystal substrate with a better lattice match to Cu<sub>2</sub>N. The surface of a Cu<sub>3</sub>Au(100) crystal induces a tensile stress of only 0.8% onto the nitride layer which is reflected in formation of islands as large as ~ 100 nm leading to formation of insulating areas that are several tens of times larger compared to the ones on Cu(100), as confirmed by STM (Fig. 4.6).

Nitride preparation settings on Cu<sub>3</sub>Au(100) is similar to Cu<sub>2</sub>N/Cu(100). We varied a number of preparation parameters as to optimize the nitride coverage on Cu<sub>3</sub>Au and found that the annealing temperature post-N<sub>2</sub> sputtering influences the size of nitride islands the strongest. We report this temperature to be ~ 550°C, i.e. approx. 150°C higher than for nitride on Cu(100), for the largest nitride islands we observed on Cu<sub>3</sub>Au(100) (Fig. 4.6). IETS spectra on nitride islands on Cu<sub>3</sub>Au(100) are shown in Fig. 4.7a, revealing an onset of a conduction band at ~ 1.8 eV.

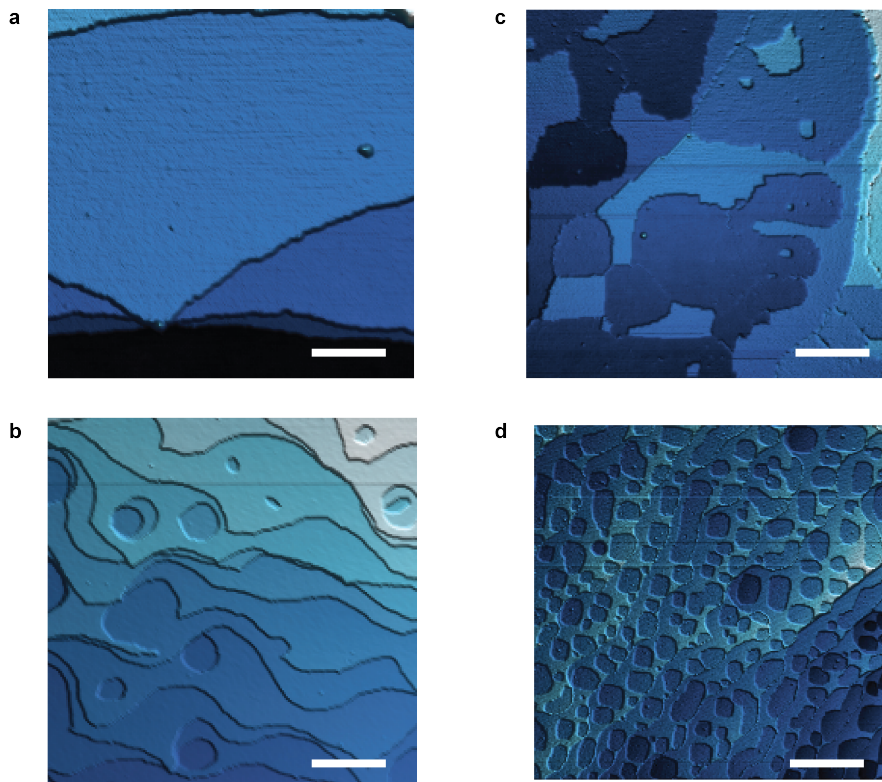


Figure 4.6: **Copper-nitride on  $\text{Cu}_3\text{Au}(100)$ .** **a** STM topography of a clean  $\text{Cu}_3\text{Au}(100)$  crystal. A terrace  $\sim 100$  nm wide can be seen. Imaging settings:  $I = 5$  pA,  $V = 20$  mV,  $T = 1.5$  K; scale bar 20 nm. **b** STM topography of clean  $\text{Cu}_3\text{Au}(100)$  crystal. Terraces as wide as 100 nm can be seen. Imaging settings:  $I = 500$  pA,  $V = 500$  mV,  $T = 1.5$  K; scale bar 100 nm. **c** STM topography of copper-nitride reconstruction of  $\text{Cu}_3\text{Au}(100)$  surface after  $\text{N}_2$  sputtering. Nitride islands with tens of nm's in both horizontal and vertical directions can be seen. Imaging settings:  $I = 5$  pA,  $V = 20$  mV,  $T = 1.5$  K; scale bar 20 nm. **d** STM topography of copper-nitride reconstruction of  $\text{Cu}_3\text{Au}(100)$  surface after  $\text{N}_2$  sputtering. Nitride islands with tens of nm's in both horizontal and vertical directions can be seen. Imaging settings:  $I = 400$  pA,  $V = 200$  mV,  $T = 1.5$  K; scale bar 100 nm.

#### 4.2.2. CO ADATOMS ON COPPER-NITRIDE ON $\text{Cu}_3\text{Au}(100)$ – SPECTROSCOPY AND MANIPULATION

Fig. 4.7b shows IETS on a Co adatom on a nitride island on  $\text{Cu}_3\text{Au}(100)$ . The Co adatom exhibits the same strong Kondo signature on this surface, similar to  $\text{C}_2\text{N}/\text{Cu}(100)$ , as well as a single anisotropy step. However, anisotropy step appears at a position 70% higher compared to the Co on  $\text{Cu}_2\text{N}/\text{Cu}(100)$  (9.5 mV in comparison to 5.5 mV). This is in agreement with the finding in [8] where a similar value was reported for Co on a large ( $20 \times 20 \text{ nm}^2$ ) nitride island on  $\text{Cu}(100)$ . In contrast to their findings, we do not observe a decrease in Kondo screening together with the large shift of the anisotropy step.

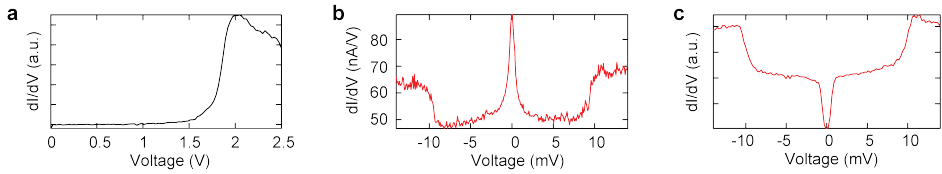


Figure 4.7: **IETS of Co adatoms on nitride islands on  $\text{Cu}_3\text{Au}(100)$ .** **a** IETS of nitride on  $\text{Cu}_3\text{Au}(100)$ . Spectrum is averaged over three spectra taken on three nitride islands from Fig. 4.6c, at positions  $\geq 5$  nm away from the edges. IETS settings:  $V_{\text{mod}} = 5$  mV,  $T = 2.1$  K. **b** IETS of a Co adatom on a nitride island on  $\text{Cu}_3\text{Au}(100)$ , positioned 5 nm away from the nearest island edge. IETS settings:  $V_{\text{mod}} = 100$   $\mu\text{V}$ ,  $T = 330$  mK. **c** IETS of a Co adatom on a nitride island on  $\text{Cu}_3\text{Au}(100)$ . Spectrum is averaged over three spectra taken on three distinct atoms positioned 2, 5 and 10 nm away from the nearest island edge. IETS settings:  $V_{\text{mod}} = 100$   $\mu\text{V}$ ,  $T = 330$  mK.

## 4

We emphasize our report being on an initial finding and further experimental confirmation is necessary before discussing the origin of the IETS step and its relation to Kondo on this surface. For instance, a thorough dependence of both the low energy spectra of the Co adatom and the nitride bandgap on  $\text{Cu}_3\text{Au}(100)$  on the distance from the edge of the island should be done. This will help discern whether strain in the nitride reconstruction is a major contributor to the Co's anisotropy shift or a Kondo exchange renormalizes the anisotropy energy as demonstrated in [8].

However, a more common IETS spectrum of a Co adatom on this surface (Fig. 4.7c) has a step rising at zero-bias instead of a Kondo feature and a similar position of the higher IETS step (9.9 mV). Spectra of this type with almost identical relative IETS step height were seen on adatoms both in the proximity of the island edge (2 nm) and considerably further away (10 nm). This suggests no influence of the nitride reconstruction on the binding site of the Co adatom.

As stated for the adatom type with a zero-bias peak, further experiments as a function of position within an island need to be performed to get a statistically significant result. Also, magnetic field dependence should be established to verify both Kondo for the adatom shown in 4.7b and the magnetic origin of the IETS steps for both adatom types (4.7b and 4.7c).

We made a few successful attempts in vertically manipulating Co adatoms on this surface. Initial findings point towards similar manipulation settings as for Co adatoms on  $\text{Cu}_2\text{N}/\text{Cu}(100)$ .

### 4.3. CL-RECONSTRUCTED $\text{Cu}(111)$ SURFACE

This part of the chapter describes an STM study of a surface platform with a hexagonal pattern of reconstruction – a chlorine monolayer on  $\text{Cu}(111)$ . Here we present an experimental realization of this surface reconstruction with different monolayer coverages. For all coverages obtained by means of thermal evaporation of  $\text{CuCl}_2$  powder onto  $\text{Cu}(111)$  crystal, a full monolayer of hexagonally reconstructed copper-chloride on  $\text{Cu}(111)$  was formed with flat and clean terraces as wide as several hundreds of nanometers providing a platform with potential for future building of atomic structures of unprecedented sizes

by means of STM manipulation. Recently, our group demonstrated a large scale STM manipulation on Cl-reconstructed Cu(100) by utilizing and manipulating the surface reconstruction defects, namely the missing Cl atoms, in defining memory bits and coding text by controlling positions of vacant Cl sites [133]. For Cl reconstruction on Cu(111), we will not be investigating in depth reconstructions with surface defects, but instead focus will be directed towards defect-free surfaces which can be used as templates for building structures with magnetic adatoms.

An insulating layer of Cl was deposited onto a clean Cu(111) surface by means of in-situ thermal evaporation of  $\text{CuCl}_2$  powder. The evaporation takes place at a partial  $\text{CuCl}_2$  pressure of  $\sim 3.5 \times 10^{-8}$  mbar of  $\text{CuCl}_2$  after current-induced heating of the crucible containing the powder. Evaporation is performed for  $\sim 40 - 50$  s, and we found the coverage to be very sensitive to evaporation time in at these evaporation pressures (5 – 10 s of difference in evaporation time lead to a crossover from a surface with missing Cl atoms to an over-saturated Cl-reconstruction). The sample was heated to 400 K prior to evaporation and kept at room temperature for 20 – 30 min before pre-cooling on the  $\text{N}_2$  thermal shield.

### SATURATED 1/3 CL MONOLAYER ON CU(111)

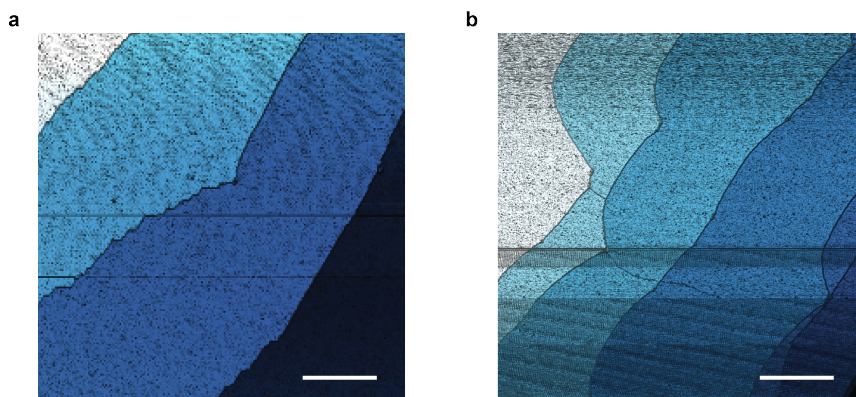


Figure 4.8: **Chlorine-terminated Cu(111) surface.** **a** STM topographic image of clean Cu(111) surface. Flat terraces as wide as 200 nm can be seen. Imaging settings:  $I = 100$  pA,  $V = 500$  mV; scale bar 100 nm. **b** STM topographic image of a Cl-terminated Cu(111) surface. Flat terraces as wide as 200 nm can be seen. Imaging settings:  $I = 100$  pA,  $V = -500$  mV; scale bar 100 nm.

Here we show results on 1/3 Cl ML  $\sqrt{3} \times \sqrt{3}R30^\circ$  on Cu(111) as a result of in-situ  $\text{CuCl}_2$  evaporation. Fig. 4.8a shows a clean Cu(111) crystal surface with terraces in the order of hundreds of nanometers wide. Post- $\text{CuCl}_2$  deposition STM image is shown in Fig. 4.8b, where large terraces of clean Cl-reconstructed Cu(111) can be seen.

Fig. 4.9a shows a small scale STM scan of this Cl surface from which the inter-atomic distance of  $d = 0.45$  nm is extracted corresponding to the  $\sqrt{3} \times \sqrt{3}R30^\circ$  reconstruction. Previous DFT studies show that the Cl atoms on Cu(111) surface prefer the hollow fcc site over the other possible sites: hollow hcp, bridge or atop a Cu atom from the outmost

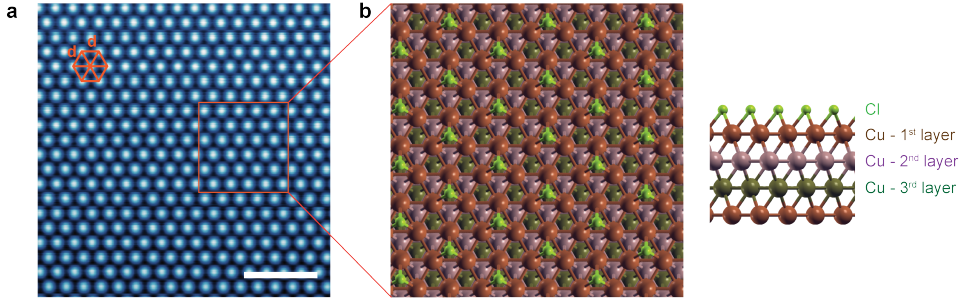


Figure 4.9:  $1/3\text{ML } \sqrt{3} \times \sqrt{3}R30^\circ$  reconstruction of Cl-terminated Cu(111) surface. **a** STM topographic image ( $I = 100$  pA,  $V = +20$  mV,  $T = 1.17$  K) showing hexagonal chlorine reconstruction on the Cu(111) surface. Distance between 2 neighbouring Cl atoms denoted by  $d$  measured to be 0.45 nm. Scale bar 2 nm. **b** Top (left) and side (right) view of the Cl-reconstruction on the Cu(111) surface as obtained from relaxation calculations by Quantum Espresso. Cl atoms sit in hollow fcc sites of the Cu(111) crystal rotated  $30^\circ$  w.r.t. the top layer of copper.

4

layer [134–137]. The fcc binding site for a Cl atom in  $\sqrt{3}R30^\circ$  reconstruction has been also experimentally verified in an STM study in [137]. Our DFT results (Fig. 4.9b) also result in fcc as preferred to other binding sites for Cl on top of Cu(111) surface, with an energy barrier of 32 meV to the next favorable binding site, the hollow hcp.

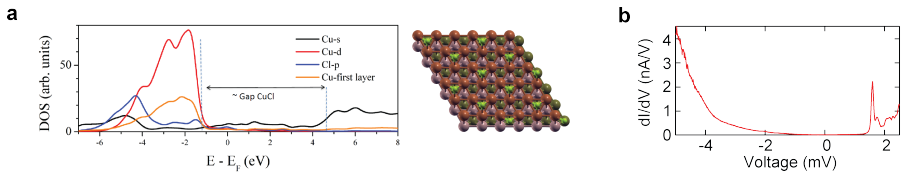


Figure 4.10: **Bandgap of the insulating Cl-terminated Cu(111) surface.** **a** DFT calculations for a unit cell depicted on the right, showing contributions from both the Cl atoms and the Cu atoms from the top layer. Color code same as in Fig. 4.9. Bandgap induced by Cl states  $\sim 6$  eV. **b** IETS spectrum of a  $\sqrt{3} \times \sqrt{3}R30^\circ$  Cl-reconstructed Cu(111). A bandgap of  $\sim 5 - 5.5$  eV was found. Spectrum mirrored about  $E = E_F$  compared to DFT due to opposite tip-sample bias convention taken.

DFT predicts a bandgap of  $\sim 6$  eV of this insulating layer (Fig. 4.10a), which deviates only by  $\sim 10 - 20\%$  from our IETS result (Fig. 4.10b).

## OTHER CL MONOLAYER COVERAGES

In an attempt to develop a full Cl monolayer with hexagonal reconstruction, we noticed a strong dependence of the Cl coverage with  $\text{CuCl}_2$  evaporation time at an evaporation pressure in the order of  $10^{-8}$  mbar. In addition to obtaining the saturated hexagonal monolayer, we report on additional two surface reconstructions: an under-saturated hexagonal reconstruction with missing Cl atoms and an over-saturated reconstruction with alternating fcc and hcp Cl domains, both shown in Fig. 4.11.

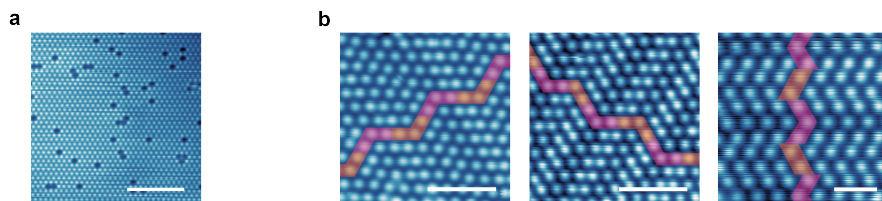


Figure 4.11: **Under- and over-saturated Cl-terminated Cu(111) surfaces.** **a** STM topography of an under-saturated  $1/3\text{ML } \sqrt{3} \times \sqrt{3} R30^\circ$  Cl-reconstruction with missing Cl atoms (appearing as dark blue features). Imaging:  $I = 100 \text{ pA}$ ,  $V = -500 \text{ mV}$ ; scale bar  $5 \text{ nm}$ . **b** STM topography of a saturated Cl-reconstructed surface. Three distinct pattern types observed under STM shown here. Notice that regular hexagonal reconstruction is established only locally with alternating fcc and hcp domains of  $< 1 \text{ nm}$  width. Imaging settings for topographies, left to right:  $I = 200/100/100 \text{ pA}$ ,  $V = +20 \text{ mV}$   $T = 1.17 \text{ K}$ ; scale bar, left to right:  $2/2/1 \text{ nm}$ .

The under-saturated Cl reconstruction on Cu(111), shown in Fig. 4.11a, is of the desired geometry ( $\sqrt{3} \times \sqrt{3} R30^\circ$ ), but the missing Cl atoms (appearing as depressions in topography of  $\sim 25 \text{ pm}$  depth) in the surface reconstruction hinder its potential for studying adatoms. Here, we will briefly summarize the results on Co adatoms on this surface reconstruction. First, it is often difficult to identify binding sites for adatoms. For example, STM cannot discern whether an adatom is sitting atop a Cl atom or in a Cl vacancy site. Also, the adatoms appear often pinned to defects in the underlying Cl reconstruction, although we cannot claim the adatom evaporation causes the emergence of defects, as the pristine Cl surface (due to missing Cl atoms) is also presented with many defects in its reconstruction. This results in areas of the desired and defect-free Cl reconstructions to be in the order of  $\leq 5 \text{ nm}$ . As a direct consequence of the many surface defects, the Co adatoms adopt many different binding sites as confirmed by STM topography (chapter 7). This binding site ambiguity is reflected in IETS spectra on Co adatoms and we, therefore, discard this surface reconstruction as suitable for further Co adatom studies.

The over-saturated Cl reconstruction shown in Fig. 4.11b, also presents only locally the required  $\sqrt{3} R30^\circ$  reconstruction and on an even smaller length scale – Cl atoms switch from fcc to hcp binding sites (and vice versa) after no more than 2 – 3 successive sites of the same hollow site type, rendering sub-nano stripe-like features in the reconstruction. Three patterns of this surface reconstruction have been observed and they are shown in Fig. 4.11b. Unlike in the case of under-saturated Cl surface, the Co adatoms appear with less variety in topography (more on this in chapter 7).



# 5

## SPIN CHAINS TEST OF QUANTUM CRITICALITY

*In this chapter we describe physical realization of a particular model-system for theoretical studies on quantum criticality and quantum phase transitions (QPTs) – spin-1/2 Heisenberg chain with anisotropic XXZ coupling. For a finite transverse (X) magnetic field this chain in thermodynamic limit undergoes a QPT from antiferromagnetic at low fields to paramagnetic state beyond the critical field [78] (2.3.1 and 5.1). Finite-size atomic chains with isotropic exchange coupling of lengths from  $N = 1$  to  $N = 9$  atoms were constructed via STM vertical manipulation of spin-3/2 Co adatoms on  $\text{Cu}_2\text{N}/\text{Cu}(100)$  (5.2). The chains were engineered such that the crystal field of the surface leaves the ground state of the chains dominated by spin-1/2 states at zero magnetic field and low temperatures allowing for treatment of these chains as effective spin-1/2 chains with intrachain exchange interactions of the XXZ type (5.4). Chain site resolved STM probing in transverse field revealed ground state crossings the near critical field density of which rises with chain length indicating an onset of quantum criticality in these chains (5.5).*

---

This chapter describes work published as a journal article [30]. Theory results supporting this chapter were obtained by R. van den Berg<sup>†</sup>, I.S. Eliens<sup>†</sup> and J.-S.Caux<sup>†</sup>.

<sup>†</sup> Institute for Theoretical Physics, University of Amsterdam, Amsterdam, The Netherlands.

## 5.1. INTRODUCTION

The ability to manipulate single atoms has opened up the door to constructing interesting and useful quantum structures from the ground up [138]. On the one hand, nanoscale arrangements of magnetic atoms are at the heart of future quantum computing and spintronic devices [24, 139]; on the other hand, they can be used as fundamental building blocks for the realization of textbook many-body quantum models [140], illustrating key concepts such as quantum phase transitions, topological order or frustration as a function of system size. In this chapter, we describe how we employed STM to construct and measure arrays of magnetic atoms on a surface, designed to behave like spin-1/2 XXZ Heisenberg chains in a transverse field, for which a quantum phase transition from an antiferromagnetic to a paramagnetic phase is predicted in the thermodynamic limit [78].

Since the birth of quantum mechanics, lattice spin systems [141] have represented a natural starting point for understanding collective quantum dynamics. Today, scanning tunnelling microscopy (STM) techniques allow one to experimentally build and probe realizations of exchange-coupled lattice spins in different geometries [22, 25, 33]. In linear arrangements, quantum effects are strongest [142] and notions such as quantum phase transitions [143] are most easily understood, the simplest illustration being the Ising model in a transverse field [71, 144]. In this work, using STM, we construct finite-size versions of a model in the same universality class, namely the spin-1/2 XXZ chain in a transverse field [78], which has previously been realized in the bulk material  $\text{Cs}_2\text{CoCl}_4$  [88, 93]. Our set-up allows us to probe the chains with single-spin resolution while tuning an externally applied transverse field through the critical regime.

5

## 5.2. STM REALIZATION OF SPIN-1/2 XXZ HEISENBERG CHAINS

To construct the above discussed spin chain type in our lab, we make use of STM vertical manipulation at 1.5 K in our UHV Unisoku STM system the details of which were laid out in section 4.1.2.

The obvious choice for a building element of these spin-1/2 atomic chains would be a magnetic adatom with a total spin of 1/2 as the ground state (GS) of such a system would truly be of spin-1/2 character. However, magnetic adatoms on surfaces usually have spins larger than 1/2. We use Co adatoms with a total spin of 3/2 as building blocks, so in principle their GS can be occupied by either spin-3/2 or spin-1/2 states the selection of which at zero field will depend on the anisotropy the spin of the Co adatom is experiencing on this surface as a consequence of the crystal field. We use the IETS technique [2, 145] to determine the anisotropy of each atom [61]. In [3] it was shown that Co adatom on this surface experiences a strong uniaxial hard-axis anisotropy perpendicular to the bond it makes with neighboring N atoms. This lowers the energy of spin-1/2 states making them reside in the GS separated by 5.5 meV from the higher lying spin-3/2 states. In this way, as long as all energy scales involved ( $k_B T$ ,  $\mu_B B$ ,  $eV_{\text{mod}}$ ) are well below the 5.5 meV anisotropy barrier, we can treat the Co adatom as an effective spin-1/2 system and extend it to an effective spin-1/2 chain by adding more Co adatoms to it along a certain direction on this surface. In this discussion we neglect the effect of transverse anisotropy. Note that even for a non-negligible transverse anisotropy, the ground state degeneracy

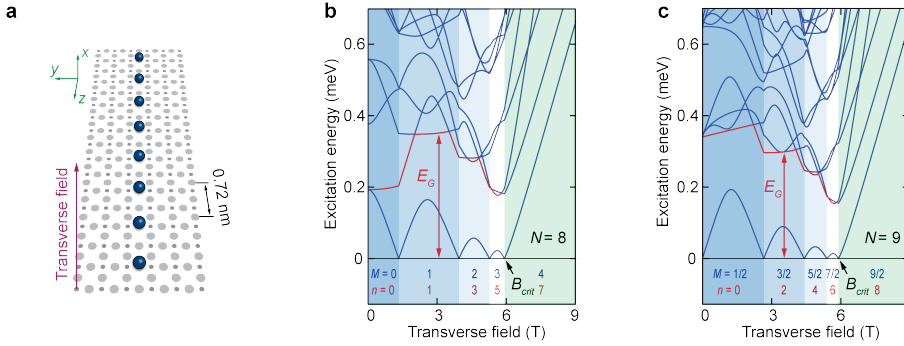


Figure 5.1: **Construction of XXZ chains.** **a** Atomic design for XXZ chains and indication of the transverse field direction. Large (small) grey circles represent Cu ( $N$ ) atoms. **b** Lowest excitation energies of an  $N = 8$  chain for a transverse field up to 9 T.  $E_G$  and  $B_{\text{crit}}$  are indicated, as well as the transverse magnetization  $M$  and average number of domain walls  $n$  between each ground state change. **c** Same as **(b)** for  $N = 9$ .

for  $\mathbf{B} = 0$  would not be broken for a non-integer spin (Co atom), due to Kramer's degeneracy. IETS measurements were conducted at  $T = 330$  mK with a modulation voltage of  $V_{\text{mod(rms)}} = 70 \mu\text{V}$  on a system with a maximum field of  $B_{\text{max}} = 9$  T which makes for all the energies to be within this anisotropy gap and justifies our treatment of Co atoms as spin-1/2 systems.

The choice of building direction for atomic chains (Fig. 5.1a) is motivated by a combination of the experimental findings presented in 4.1.3 on Co dimers in different configurations on this surface [63] and theoretical relations coming from the effective Hamiltonian shown in 2.3.2. In 4.1.3 we saw that the coupling between two Co adatoms separated by two unit cells (0.72 nm) along a N-vacancy direction is antiferromagnetic in nature which is the first condition we need to meet to construct the chains in question. Next, the strength of this AFM interaction defines the transverse field necessary to break the AFM order in the chains. In 4.1.3 we saw this strength amounts to  $J = 0.22$  meV. We need to relate this value to exchange interactions within the effective spin-1/2 Hamiltonian defined in 2.3.2, namely:  $J_z$ ,  $J_{\perp}$  and  $J_{\perp}^{\text{nnn}}$  (eq. 2.7).

As shown in 4.1.2, our  $\text{Cu}_2\text{N}$  islands are typically  $5 \times 5 \text{ nm}^2$  in size, which makes them too small for anisotropy inhomogeneity reported in [8] where they measured changes in anisotropy barrier of a factor of two between Co adatoms located in the center as opposed to adatoms located near island edges. This big difference comes from the fact their  $\text{Cu}_2\text{N}$  islands are  $\sim 20 \times 20 \text{ nm}^2$  in size. We don't see anything close to such variety in anisotropy energy of Co atoms on our nitride islands and will, in the discussion that follows, take magnetic anisotropy  $D$  to be the same for all atoms in our chains and equal to the single ion anisotropy for Co on this surface:  $D = 2.75$  meV.

Now we have the necessary ingredients to calculate the effective Hamiltonian exchange interactions (eq. 2.7), which in our case translates to:

$$J_{\perp} = 0.88 \text{ meV}, \quad J_z = 0.105 \text{ meV}, \quad J_{\perp}^{\text{nnn}} = -0.064 \text{ meV}.$$

Note that indeed, for our chains,  $J_{\perp}^{\text{nnn}} \ll J_{\perp}, J_z$ , so we can neglect this term ( $J_{\perp}^{\text{nnn}} = 0$ ). This, as mentioned in 2.3.2, reduced the effective spin-1/2 Hamiltonian (eq. 2.6) to the spin-1/2 XXZ Hamiltonian in transverse field (eq. 2.2) for which the quantum phase transition is predicted in thermodynamic limit [78].

The effective spin-1/2 Hamiltonian bulk/boundary g-factors (eq. 2.8) are:

$$g_{\text{bulk}} = 1.707g, \quad g_{\text{boundary}} = 1.853g,$$

where  $g = 2.3$  [3].

If we make the following approximations:

$$J_z/J_{\perp} = 1/8, \quad J_{\perp}^{\text{nnn}} = 0, \quad g_{\text{bulk}} = g_{\text{boundary}} \cong g_{\text{eff}},$$

the resulting spin-1/2 XXZ Hamiltonian yields the following relation between the effective transverse coupling and critical value for the transverse field [78]:

$$g_{\text{eff}}\mu_B B_{\text{crit}} \approx 1.5J_{\perp}.$$

If we take  $g_{\text{eff}} \approx 1.8g$ , we get for a critical field value in the thermodynamic limit:  $B_{\text{crit}} \approx 5.5$  T, which is experimentally accessible in our lab.

## 5

### 5.3. FINITE CHAINS PREDICTIONS

Now that the mathematical formalism that transposes the isotropic spin-3/2 system to an effective spin-1/2 XXZ system has been established in the thermodynamic limit, let us take a look at the theoretical predictions that follow for chains of finite size in transverse field as those will be a system of study in our experiments. Fig. 5.1b,c displays low-energy calculations as a function of transverse field for a system with an even number of atoms ( $N = 8$  in panel b) and a system with an odd number of atoms ( $N = 9$  atoms in panel c). The two energy diagrams are composed of a number of lowest excitation energies for the two chains (energies one needs to provide the chain for it to reach a certain excited state starting from the ground state). This means the lowest energy curve corresponds to the energy difference between the GS and the 1<sup>st</sup> excited state, the next higher one to the energy difference between the GS and the 2<sup>nd</sup> excited state and so on. None of the curves in the excitation spectra of these two chains, but the lowest two, will be a matter of discussion here.

First observation we will make relates to the parity in the atom number in these chains. Comparing the lowest excitation energy spectrum for the two chains, it is clear that there is no energy gap for odd-numbered chains at zero field as compared to the even-numbered ones. This means that at zero field the Néel-like order in odd chains results in a degenerate GS state with a gap to higher states whereas even chains host a non-degenerate GS state with no energy gap to the closest higher state. For large AFM chains with half-integer spins ( $N \rightarrow \infty$ ), the GS and the 1<sup>st</sup> excited state become degenerate at zero field like for the case of finite odd chains [146]. In the  $N \rightarrow \infty$  limit this degenerate state stays separated from the higher lying excitation spectra (which in that case form a continuous band) by the energy gap  $E_G$  which collapses only at  $B_{\text{crit}}$ . It is right before this field value that spin-liquid state is predicted [78].

The second observation tackles the arising complexity with the chain length. From the  $N = 8$  and  $N = 9$  panels it is obvious that adding one atom (spin) to the 8-atom chain results in introducing an extra node in the lowest excitation spectrum with the critical field not being significantly changed which densifies the already existing nodes. These nodes (zero-points in the lowest excitation curve) are defined by field values at which the two lowest energy levels of the chain cross each other, or in other words, points in which a chain changes its ground state. Thus, with chain length increasing, more ground states changes the chain will go through before finally entering a paramagnetic phase beyond the critical field. In terms of domains walls separating regions of AFM coupled spins in a chain structure, each of these nodes marks the entry of a new domain wall into the chain and a step-wise increase of the total magnetization of the chain (Fig. 5.2).

Lower panels in Fig. 5.2 presenting first excitation mode of a spin-3/2 isotropic Hamiltonian for  $N = 1$  to  $N = 9$  chains capture both the atom number parity effect in finite chains and the increasing density of ground state changes with chain length. We will present experimental evidence for these theoretical predictions in the next section.

## 5.4. EXPERIMENT AND COMPARISON TO SPIN-1/2 XXZ MODEL

We constructed chains of Co atoms of various length and performed low-temperature IETS measurements ( $T = 330 \text{ mK} < E_G/k_B$ ) on each atom in a chain while varying the strength of the transverse field.

IETS measurements on Co atoms were realized by recording  $dI/dV$  spectra employing a lock-in technique with an excitation voltage amplitude of  $70 \mu\text{V}_{\text{rms}}$  at 928 Hz. Unless specified otherwise, in all measurements the applied magnetic field (up to 9 T) was oriented perpendicular to the sample surface. To obtain an extensive data set, a fully automated measurement sequence was employed. IETS measurements were performed at intervals of 200 mT, forming a set of 46 spectra per atom (except for the seven-atom chain, for which only 44 spectra up to 8.6 T were performed). To achieve a substantial reduction of the data acquisition time, an automated procedure was developed. After taking spectra on each atom at a given field, the tip returned to the first atom and retracted 2 nm, followed by a 50 mT automated field sweep. Following each sweep, the tip was brought back into the tunnelling range (50 pA, 15 mV), following which potential drift was corrected for through an automated atom-locking procedure. The field should be increased by 50 mT or less in each sweep to avoid the drift being larger than one atom radius. For data presented in this section, IETS measurements were performed after every fourth field sweep to give an interval of 200 mT. Using this method, obtaining a data set for fields ranging from 0 T to 7 T required performing the experiment continuously for 7 h on a single Co atom to 28 h on a  $N = 9$  chain. Spectra taken above 7 T were obtained manually for each atom of every chain, owing to tip instabilities disabling proper atom locking when sweeping the field in that range.

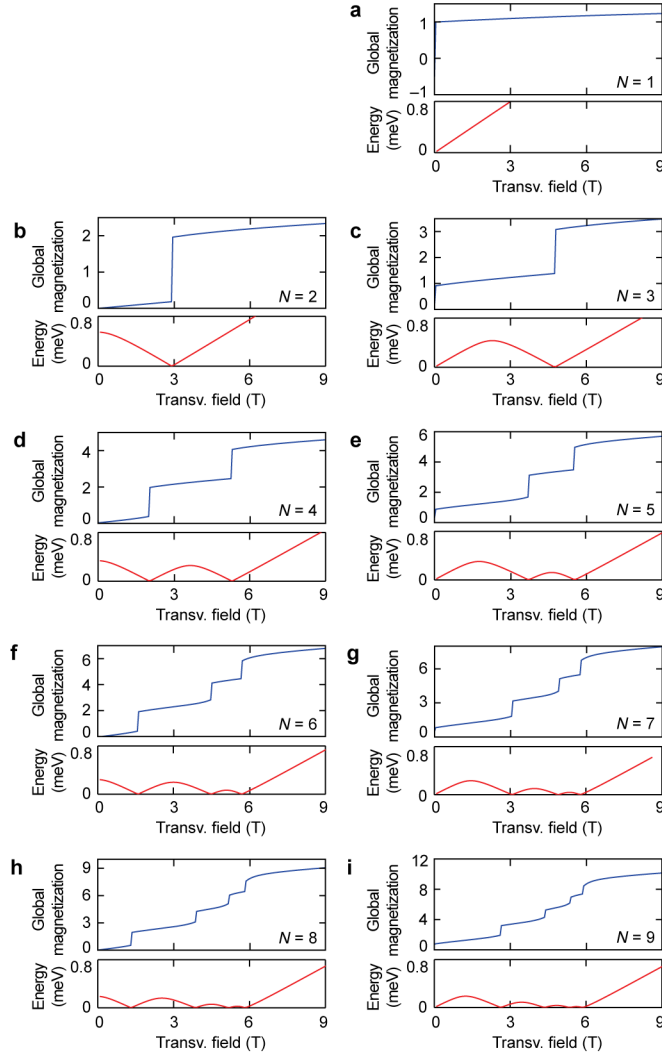


Figure 5.2: **Chain magnetization.** **a-i** Total magnetization calculations along the field direction (blue) for chains  $N = 1$  to 9 as calculated from the  $H_{3/2}$  model. Below: lowest excitation energy calculations (red) following from the same model.

Fig. 5.3a,b shows measurements taken on the first atom of an odd-length (5 atoms) and an even-length chain (6 atoms), respectively, recorded for every 200 mT from 0 to 9 T. At voltages below 5.5 mV, transitions within the manifold of  $m_z = \pm 1/2$  states are observed; excitations at higher voltages correspond to transitions to the  $m_z = \pm 3/2$  manifold. The spectra show sudden changes in both excitation energy and intensity at field values corresponding to expected ground state crossings: near 3.5 T for  $N = 5$  and near 1.5 T and 4 T for  $N = 6$ .

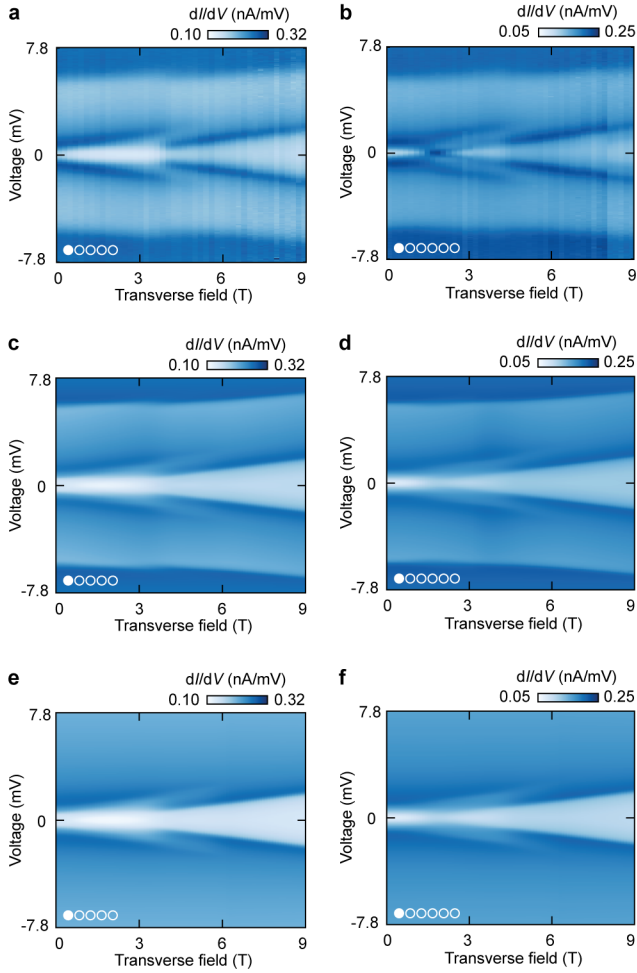


Figure 5.3: **Comparison to theory.** **a** IETS spectra taken on atom 1 of an  $N = 5$  chain in transverse fields ranging from 0 T to 9 T, in increments of 200 mT. **b** Same as **(a)**, but taken on atom 1 of an  $N = 6$  chain. IETS curves were normalized to correct for tip height variations. Conductance values listed at the colour bars are indicative only: owing to normalization, scaling between spectra may vary by  $\sim 20\%$ . **c, d** Theoretical spectra corresponding to **(a, b)** respectively, calculated using a spin-3/2 model. The Kondo peak appearing at the first ground state crossing in **(b)** is under-represented in the theory **(d)**. **e, f** Same as **(c, d)** but calculated using a spin-1/2 XXZ model).

To simulate the differential conductance spectra, we employed a perturbative transport model [63, 116, 145, 147]. Steps related to the spectrum are found in good agreement with the data using the  $S = 3/2$  Hamiltonian (Fig. 5.3c, d). Calculations using the  $S = 1/2$  XXZ Hamiltonian (Fig. 5.3e, f) show similar agreement, except for the excitations to the  $m_z = \pm 3/2$  multiplet near  $\pm 5.5$  mV, which are not modelled. This agreement justifies our

effective spin-1/2 treatment. A notable quantitative discrepancy between theory and experiment is found near 1.5 T in the  $N = 6$  chain. At this field value, a two-fold ground state degeneracy occurs, resulting in a zero-bias Kondo resonance in the data, which is only partly reproduced in the third-order perturbative analysis [63, 116, 148–150].

## 5.5. OBSERVATION OF ONSET OF QUANTUM CRITICALITY IN FINITE ATOMIC CHAINS

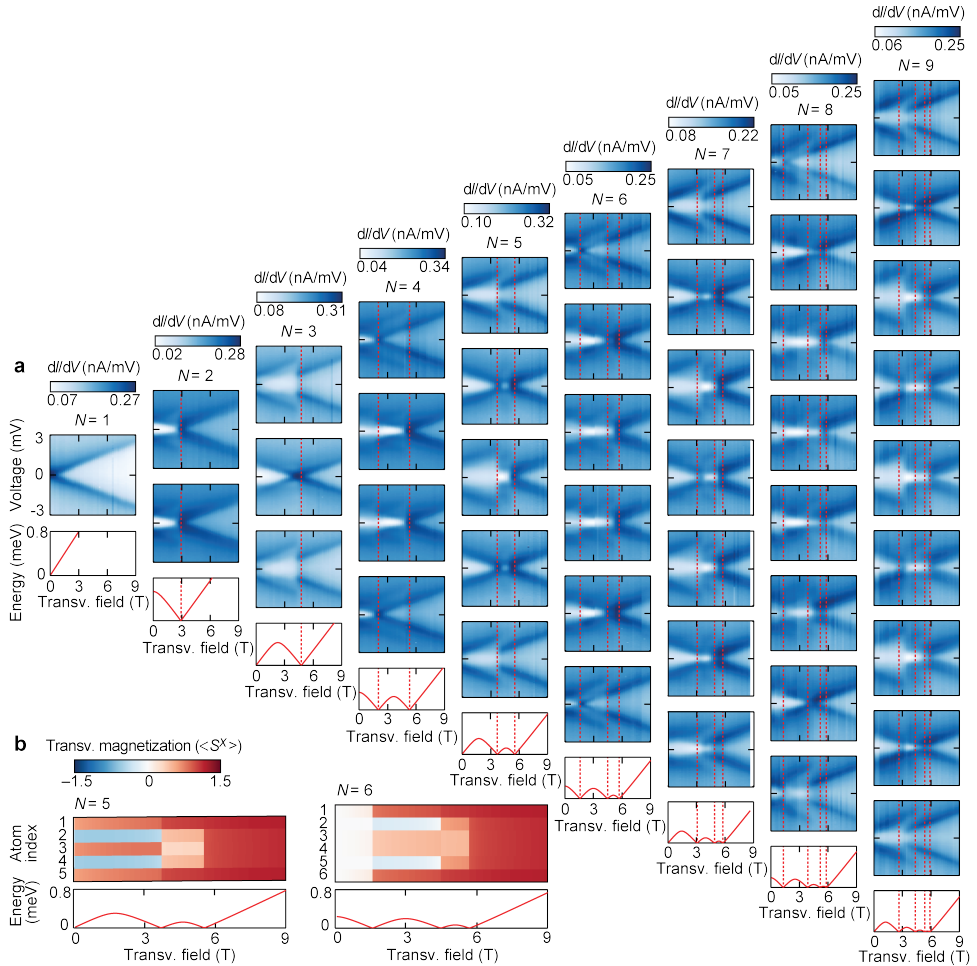


Figure 5.4: **Experimental results on chains of one to nine atoms.** **a** IETS spectra from 0 T to 9 T transverse field (in 200 mT increments) obtained on each atom of every chain up to a length of nine atoms (up to 8.6 T for  $N = 7$ ). Calculated lowest excitation energies are shown below each chain data set. Red dashed lines indicate positions of expected calculated ground state crossings. Owing to normalization, scaling of individual spectra may differ by  $\sim 20\%$  from values listed at the colour bars. **b** Site-resolved transverse magnetization ( $\langle S^x \rangle$ ) for  $N = 5$  and  $N = 6$  as calculated from the  $H_{3/2}$  model. Excitation energies (red) same as in (a).

In Fig. 5.4a, field-dependent measurements are shown for all atoms of chains of 1 to 9 atoms, featuring a total of 2,056 IETS spectra. Here, we focus on the  $\pm 3$  mV range corresponding to the  $m_z = \pm 1/2$  multiplets. As chain length increases, more features become visible, each marking a change of the ground state as the field is increased. When comparing these to the calculated ground state crossing positions (lower panels), we find that for chains up to length  $N = 6$  each feature lines up with one of the crossings. The IETS data also reveal the positions within each chain which are affected most by each of the ground state crossings; these findings are supported by local magnetization calculations along the field direction (Fig. 5.4b and Fig. 5.5).

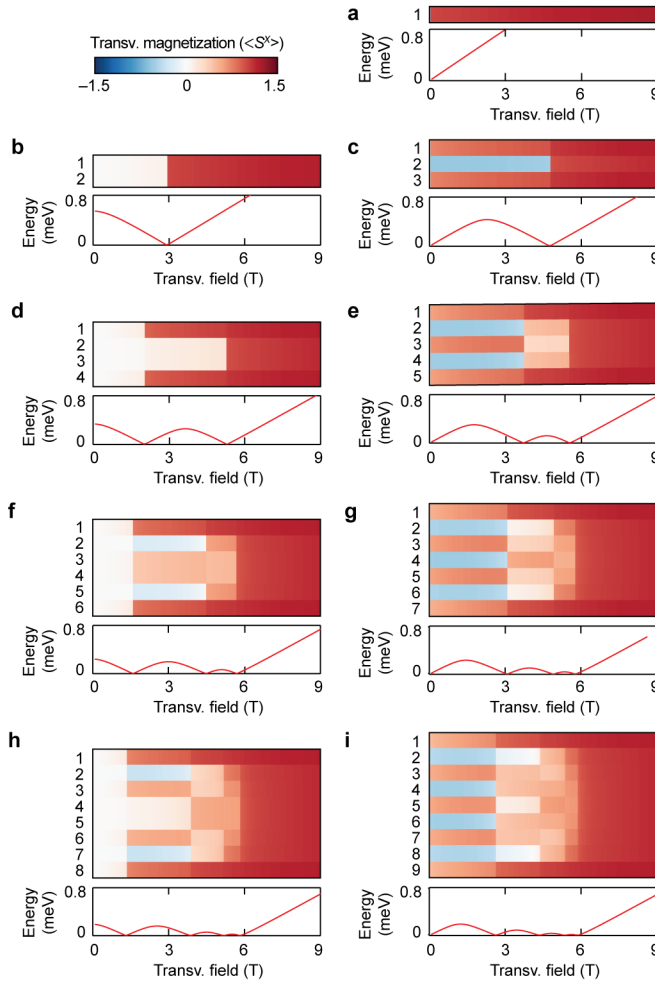


Figure 5.5: **Magnetization per site.** a-i Calculated magnetization ( $\langle S^x \rangle$ ) for the  $H_{3/2}$  model along the field direction per site for  $N = 1$  to 9 chains. Each magnetization plot is accompanied with the  $H_{3/2}$  lowest excitation energy curve (red). Changes in local magnetization correspond to the experimentally observed field evolution of  $dI/dV$  features per site shown in Figs. 5.4 and 5.6.

For longer chains, the positions of the gap closings in the IETS data deviate slightly from the calculated values, although qualitatively the observed data evolve as expected. A possible explanation for this discrepancy is the presence of long-range interactions: including an additional ferromagnetic next-nearest neighbour coupling of  $0.05J$  gives a better agreement with the data even in longer chains (see Fig. 5.6). However, we believe that a number of other effects may contribute to the discrepancy as well; a full resolution of the mismatch would necessitate an extensive study of both the electronic and magnetic properties of the substrate and the adatoms.

On atoms in the bulk of the chain (two or more sites away from an edge), a continuous featureless region is observed between 3 T and 6 T, which widens as chain length increases. In this field range, ground state crossings become too close to be individually resolved. The energy difference between the ground state and the zero mode also decreases, such that their thermal occupations become comparable. This further reduces the ability to resolve the crossings.

## 5

A simplified picture in terms of spin-1/2 product states and spin flip operations [33] provides a qualitative understanding of the IETS spectra. In even chains, for small fields, the two Néel orderings are equally mixed in the ground state. Here the first crossing is predominantly found on the outer atoms, because at this crossing the number of domain walls  $n$  increases by 1 only. In odd-length chains, the magnetic field selects one of these Néel states leading to a definite staggered magnetization profile: flipping the spin of an odd (even) atom points it against (along) the magnetic field, leading to a state increasing (decreasing) in energy with increasing field. At fields above the critical field, the ground state is essentially polarized and we can obtain a similar understanding in terms of magnon physics.

The semiclassical reasoning outlined above is further confirmed by measurements taken on a seven-atom chain with a spin-polarized (SP) STM tip, shown in Fig. 5.7. In contrast to SP-STM measurements taken at a fixed voltage, these spectra reveal spin contrast in energy-dependent phenomena such as spin excitations. Let us first take a look at the SP-tip used for this measurement. A spin-filtering tip was created by attaching several Co atoms to the tip and applying a field of 3 T perpendicular to the surface. Spin polarization was verified by performing spectroscopy on a single Co atom. As shown in Fig. 3.4, the relative heights of the peaks were found to be opposite to those recently reported [117], indicating that the ultimate atom of the tip was polarized opposite to the external field owing to exchange forces within the tip. If we take a look at the SP-IETS of a 7-atom chain now, at 3 T we see, in addition to the even-odd pattern in the excitation energies, an alternating pattern in spin excitation intensities [33] (Fig. 5.7c). For positive sample bias, in which case an excess of spin-down electrons from the tip is injected into the chain (Fig. 3.4), excitations on odd-site spins are enhanced. At negative voltage, excitations are enhanced on the even sites. This alternating pattern is found to disappear as the field is swept through the critical value (Fig. 5.7d). Additional SP-STM data are shown in Fig. 5.8.

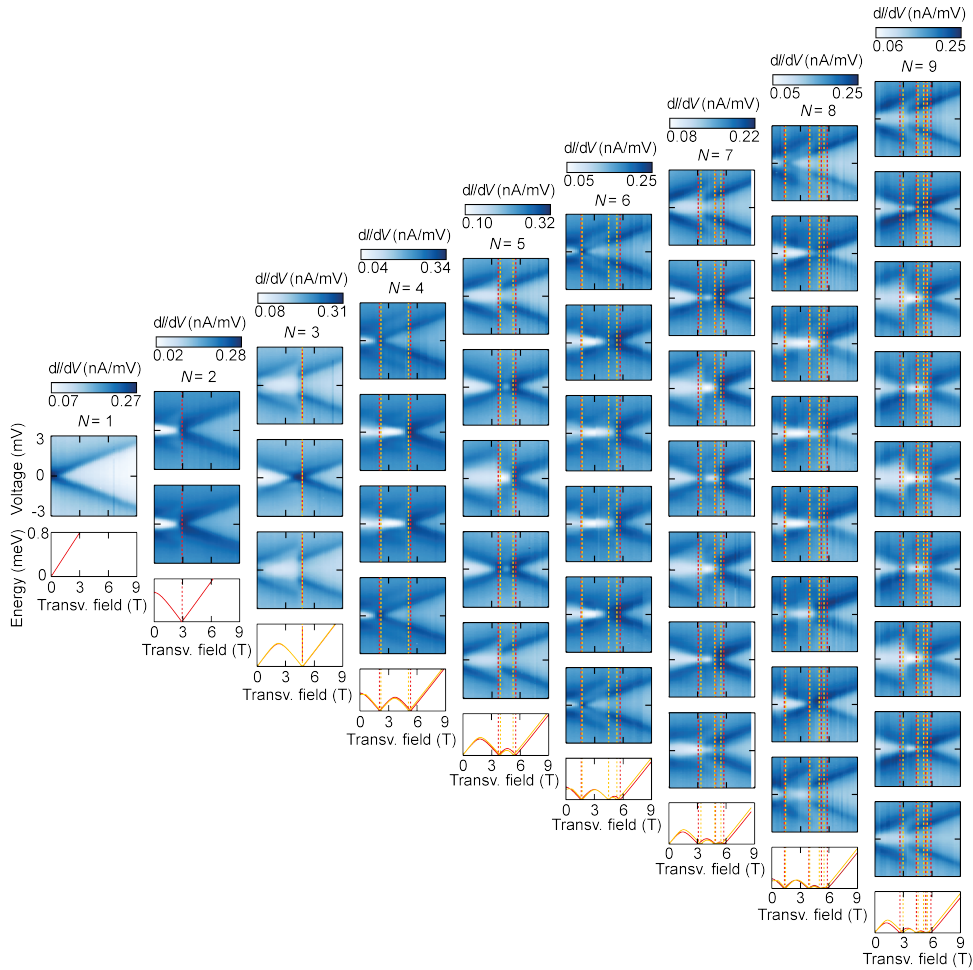


Figure 5.6: **Experimental results on chains of 1 to 9 atoms – comparison with  $H_{3/2}$  taking into account next-nearest neighbor (nnn) interaction.**  $\pm 3$  mV IETS spectra from 0 T to 9 T transverse field (in 200 mT increments) obtained on each atom of every chain up to a length of 9 atoms (up to 8.6 T for  $N = 7$ ). Red dashed lines indicate positions of expected ground state crossings calculated from the  $H_{3/2}$  model with antiferromagnetic nn coupling  $J$  only (same as in Fig. 5.4b). Orange dashed lines come from the same model but accounting for ferromagnetic nnn coupling of  $0.05J$ . Same color coding applies to the energy calculations below each chain data set. Due to normalization, scaling of individual spectra may differ by  $\sim 20\%$  from values listed at the color bars.

## 5.6. CONCLUSIONS

We have built chains of effective  $S = 1/2$  spins realizing the XXZ model in a transverse field, and obtained detailed site-resolved information about the spectrum as a function of chain length and applied field. Increasing the chain length shows a growing number of ground state crossings, a precursor of the Ising quantum phase transition occurring in the thermodynamic limit. Site-resolved measurements on these finite-size realizations

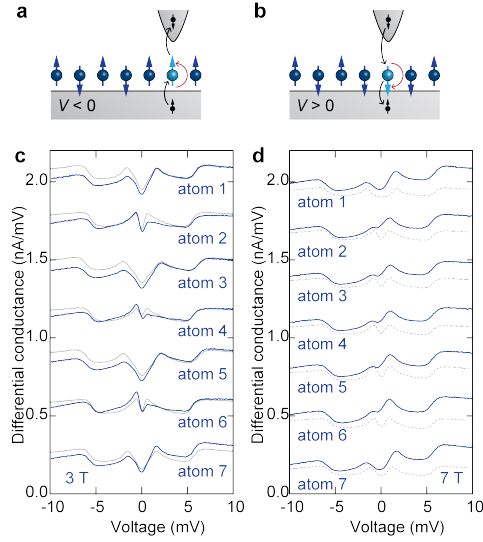


Figure 5.7: **Spin-polarized spectroscopy.** **a, b** Schematics showing allowed spin excitations in the case of a fully polarized (in the spin-down direction, see Fig. 3.4) STM tip for negative and positive sample voltages, respectively. **c** Spin-polarized IETS spectra taken in a 3 T transverse field on an  $N = 7$  chain (blue curves). Corresponding spectra taken with an unpolarized tip are shown in grey. **d** Same as (c) but in a 7 T transverse field. Here the unpolarized data (dotted grey lines) were taken on a different, but identical chain.

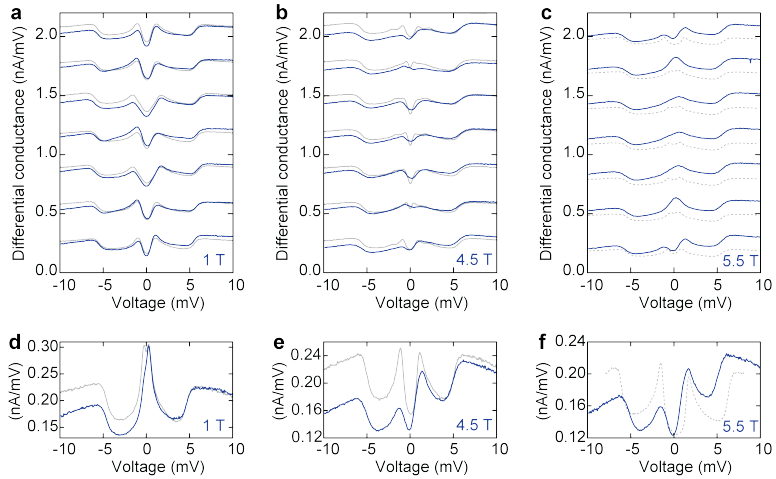


Figure 5.8: **Additional SP-IETS measurements on a 7-atom Co chain.** **a-c** Spin-polarized IETS spectra taken at 1 T, 4.5 T and 5.5 T transverse field in an  $N = 7$  chain (blue curves). Corresponding spectra taken with an unpolarized tip are shown in grey. **d-e** IETS spectra taken on a single Co atom at the same field values as in (a-c) with the same spin-polarized tip (blue) and with a spin-unpolarized tip (grey). Dashed spin-unpolarized curves were taken on a different instance of the chain/atom than the corresponding spin-polarized curves.

reveal a number of sudden ground state changes when the field approaches the critical value, each corresponding to a new domain wall entering the chains. We observe that these state crossings become closer for longer chains, suggesting the onset of critical behaviour.

Our results present opportunities for further studies on quantum behaviour of many-body systems, as a function of their size and structural complexity. The origin of the discrepancy between the theoretical positions of ground state crossings and those observed in longer chains remains an open issue that requires a better understanding of the electronic and magnetic structure of the chains and their supporting surface. Our work demonstrates that STM-built spin lattices offer a viable platform, complementary to, for example, ultracold neutral atoms and trapped ions, for experimentally testing quantum magnetism with local precision.



# 6

## CONTROLLING SPIN AND ORBITAL INELASTIC TUNNELING IN ATOMIC CHAINS

*The inelastic portion of the tunnel current through an individual magnetic atom grants unique access to read out and change the atom's spin state, but it also provides a path for spontaneous relaxation and decoherence. Controlled closure of the inelastic channel would allow for the latter to be switched off at will, paving the way to coherent spin manipulation in single atoms. In this chapter we present a study that demonstrates complete closure of the inelastic channels for both spin and orbital transitions due to a controlled geometric modification of the atom's environment, using STM. The observed suppression of the excitation signal, which occurs for Co atoms assembled into chains on a  $\text{Cu}_2\text{N}$  substrate, indicates a structural transition affecting the  $d_{z^2}$  orbital, effectively cutting off the STM tip from the spin-flip cotunneling path.*

---

This chapter describes work published as a journal letter [27]. Theory results supporting this chapter were obtained by A. Ferrón<sup>†§</sup>, J. L. Lado<sup>†</sup> and J. Fernández-Rossier<sup>†⊥</sup>.

<sup>†</sup> International Iberian Nanotechnology Laboratory (INL), Braga, Portugal

<sup>§</sup> Instituto de Modelado e Innovación Tecnológica (CONICET-UNNE), Corrientes, Argentina

<sup>⊥</sup> Departamento de Física Aplicada, Universidad de Alicante, Alicante, Spain

## 6.1. INTRODUCTION

Cotunneling is a two-step process that may happen whenever an electron-confining island (e.g., an atom, molecule, or quantum dot) is weakly coupled to two electrodes; an electron hops from the first electrode to the island and another electron hops from the island to the second electrode. If the final state has a different energy than the initial state, the cotunneling process is inelastic and can only occur if sufficient bias voltage is applied. This effect has proven highly useful in probing, for example, molecular vibrations [104, 106], excitations of quantum dots [151] and carbon nanotubes [152], and spin-flip excitations on molecules [19, 23, 153] and single atoms [2, 7, 154, 155]. Inelastic processes involving a spin-flip can only occur when tunneling into a singly occupied level [156]. Inelastic cotunneling also opens an inelastic decay channel [20, 25, 32], limiting spin lifetimes; it would therefore be desirable to be able to switch the inelastic path on and off.

Atomic assembly of magnetic nanostructures allows for fine control of parameters such as spin coupling [5, 33, 63] and single atom magneto-crystalline anisotropy. The anisotropy of single atoms and molecules can be modified by the application of local strain, either induced by the placement of neighboring atoms [61, 62] or applied using a scanning probe tip [20, 157]. Here we show, using both spin and orbital inelastic excitation spectra, that local strain can result in complete closure of an inelastic cotunneling channel, due to orbital hybridization leading to modification of the effective orbital filling. For Co atoms assembled into chains, we observe a complete suppression of all spin excitations and of certain newly observed orbital excitations.

6

## 6.2. SUPPRESSION OF SPIN AND ORBITAL EXCITATIONS IN CO ATOMIC CHAINS

Fig. 6.1 shows an STM topographic image and IETS measurements of a dimer of Co atoms, constructed using vertical atom manipulation on a  $\text{Cu}_2\text{N}$  surface, and also of a Co trimer and tetramer constructed as extensions of the dimer. Measurements were carried out at 330 mK in ultrahigh vacuum ( $< 2 \times 10^{-10}$  mbar). All nanostructures were constructed with two unit-cell spacing along the direction of the neighboring N atoms ( $x$ -axis). The dimer spectra differ from the single Co case [3] but can be fitted with simulated spin excitation spectra [63] by including an antiferromagnetic exchange coupling of 2 meV (Fig. 6.2). A remarkable effect occurs for chains of three atoms or longer (Fig. 6.1b,c); the end atoms of the chains show spin excitation steps around 8 and 13 mV but no steps are seen on the inner atoms, even up to 75 meV (see Fig. 6.3). The theoretical maximum energy for a single  $\Delta S = 1$  spin flip transition is  $\delta_{\max} = \lambda \Delta S_{L_{\max}} = 66$  meV [9], between orbital states split by the spin-orbit coupling  $\lambda = 22$  meV with maximum unquenched orbital momentum  $L_{\max} = 3$ .

Fig. 6.4 shows IETS spectra of a Co hexamer on  $\text{Cu}_2\text{N}$ , again without steps on the inner atoms. Significant changes are also seen in spectroscopy performed at higher bias voltage. In spectra taken on the end atoms up to  $\pm 1$  V, a prominent peak at +500 mV is observed (Fig. 6.4c); single Co atoms show similar spectra (red curve). But for the inner

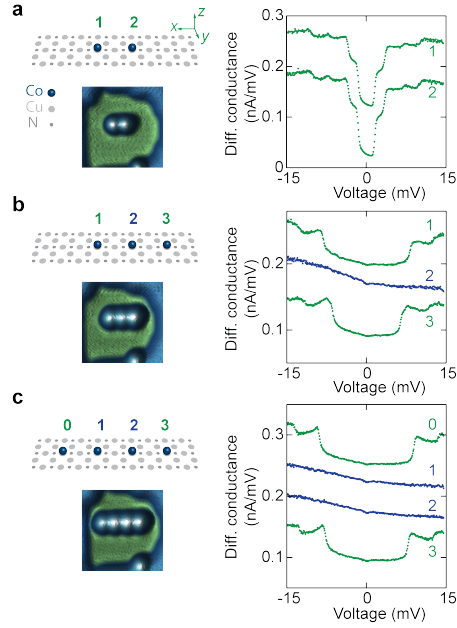


Figure 6.1: **Suppression of spin inelastic excitations in Co nanostructures.** Structural model, STM topograph, and IETS spectra of a Co dimer built by atom manipulation on  $\text{Cu}_2\text{N}$  (a), and a Co trimer (b) and tetramer (c) built as extensions of the dimer. The spectra of the dimer, and the edge atoms of the trimer and tetramer (shown in green) show spin IETS steps. Spectra of the inner atoms of the trimer and tetramer (blue) show no spin excitations. For the STM images a sample bias of 15 mV and tunnel current of 5 pA was used. Spectra were recorded with a lock-in amplifier, using a modulation of  $50 \mu\text{V}_{\text{rms}}$ , at a typical conductance of  $1 \mu\text{S}$ .

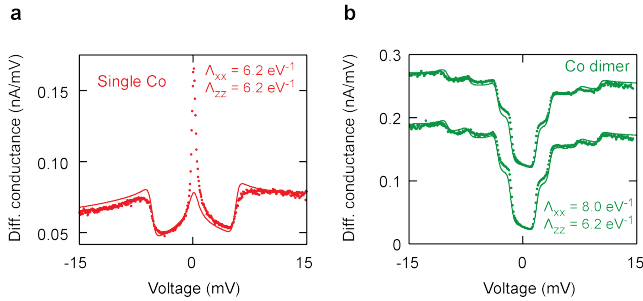


Figure 6.2: **Comparison of single Co and Co dimer spectra.** a  $dI/dV$  spectrum of a single Co atom on  $\text{Cu}_2\text{N}$  (dots). The solid line is a simulated spin IETS spectrum using  $S = 3/2$ ,  $\Lambda_{xx} = \Lambda_{zz} = 6.2 \text{ eV}^{-1}$ ,  $\Lambda_{yy} = 0$ , equivalent to  $D = 2.7 \text{ meV}$ ,  $E = 0$ . Interactions with substrate electrons are taken into account up to 3rd order, using an antiferromagnetic Kondo-exchange coupling  $J_K \rho_s = -0.15 \text{ meV}$ . However, this still underestimates the height of the Kondo peak. b  $dI/dV$  spectra of each atom of a Co dimer on  $\text{Cu}_2\text{N}$  (dots). This is the same dimer as shown in Fig. 6.1. Solid lines are simulated spin IETS spectra including an antiferromagnetic spin coupling of 2 meV.  $\Lambda_{xx} = 8.0 \text{ eV}^{-1}$ ,  $\Lambda_{zz} = 6.2 \text{ eV}^{-1}$ ,  $\Lambda_{yy} = 0$ ,  $J_K \rho_s = -0.08 \text{ meV}$ . Importantly, only the anisotropy term along the dimer (x) axis is changed from the single atom case.

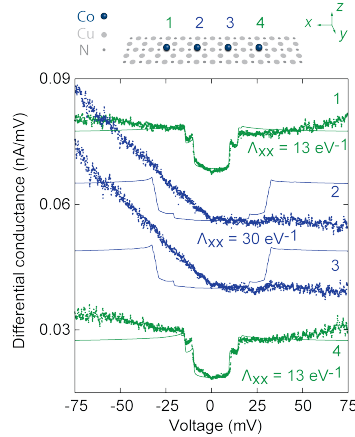


Figure 6.3: **Spectra of a Co tetramer up to 75 mV.**  $dI/dV$  spectra (dots) of each atom of a Co tetramer, similar to Fig. 6.1c and Fig. 6.7a, at up to 75 mV. On the inner atoms, no spin excitation steps are seen. The solid lines are simulated spin excitation spectra. Although no spin excitations are observed on the inner atoms, it is necessary that the inner atom  $x$ -axis anisotropy  $\Lambda_{xx} > 25 \text{ eV}^{-1}$  to reproduce the end atom spectra. For the model shown, for all atoms  $S = 3/2$ ,  $J_K \rho_s = -0.05 \text{ meV}$ ,  $\Lambda_{zz} = 6.2 \text{ eV}^{-1}$ ,  $\Lambda_{yy} = 0$  and the antiferromagnetic spin coupling is 2.5 meV. For the end atoms  $\Lambda_{xx} = 13 \text{ eV}^{-1}$ , for the inner atoms  $\Lambda_{xx} = 30 \text{ eV}^{-1}$ . The model reproduces the end atom spectra accurately: for the inner atoms it predicts a step at 30 meV which is not observed, since spin excitations on these atoms are suppressed due to the strongly hybridized  $d_{z^2}$  orbital.

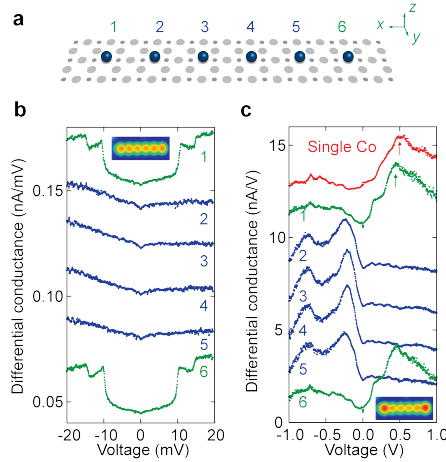


Figure 6.4: **Orbital and spin excitations in a Co nanostructure.** **a** Structure of a Co N-row hexamer on  $\text{Cu}_2\text{N}$ . **b** Spin IETS spectra of a Co hexamer, showing suppression of IETS steps on inner atoms (blue). A topographic image at +20 mV is shown (inset). **c** Higher bias spectra on the same hexamer with a single Co atom (red) for comparison. The peak at +500 mV sample bias seen on the single Co (indicated) is attributed to an orbital excitation; the same peak is seen on the end atoms of the hexamer (green), though slightly shifted. In the inner atoms of the hexamer (blue), all positive bias spectral features are suppressed. A topographic image at +500 mV is shown (inset). The conductance was  $1 \mu\text{S}$  for the 20 mV spectra and 2 nS for 1 V.

atoms, all spectroscopic features at positive voltage, including the peak at +500 mV, disappear. Also, spectral features at negative bias are more pronounced on the inner atoms. The correspondence between suppression of steps at low voltage and high positive voltage is found for all Co atoms on  $\text{Cu}_2\text{N}$ .

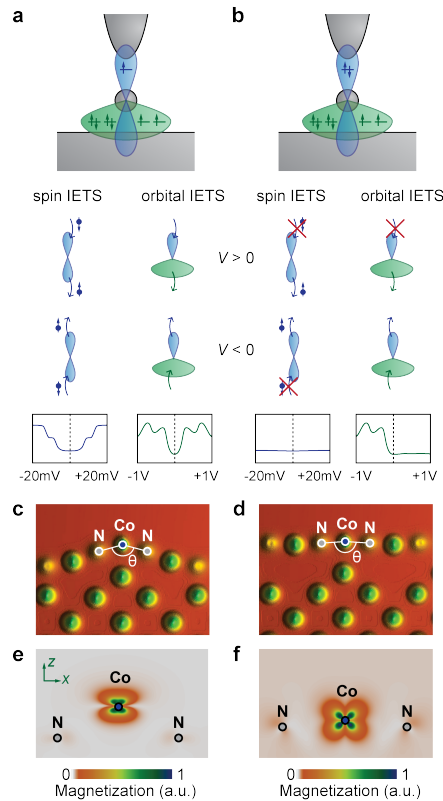


Figure 6.5: **Suppression of orbital and spin IETS transitions.** **a** Schematic of spin and orbital inelastic transitions. The  $d_{z^2}$  orbital (blue) couples to the tip and the substrate; the other  $d$  orbitals (green) couple only to the substrate. In the case of a magnetic atom with a half filled  $d_{z^2}$  orbital (**a**), spin IETS and orbital IETS transitions are allowed for both tunneling directions (bias polarities). In the case of a fully filled  $d_{z^2}$  orbital (**b**), spin excitations are blocked and orbital excitations are only possible for negative sample bias. **c** DFT calculated relaxed structure for Co monomer and (**d**) infinite double-spaced Co chain on  $\text{Cu}_2\text{N}$ . Calculated magnetization density is shown for (**e**) a Co monomer and (**f**) the infinite chain.

The spectral feature at +500 mV may be associated with an inelastic excitation that involves a change in orbital filling, as observed previously in quantum dots [151, 158]. A schematic of spin and orbital excitation processes is shown in Fig. 6.5. Spin IETS transitions involve a single spin flip and thus cost the Zeeman and/or magnetic anisotropy energy of a few millielectronvolts; electrons tunnel onto and off the same orbital. Or-

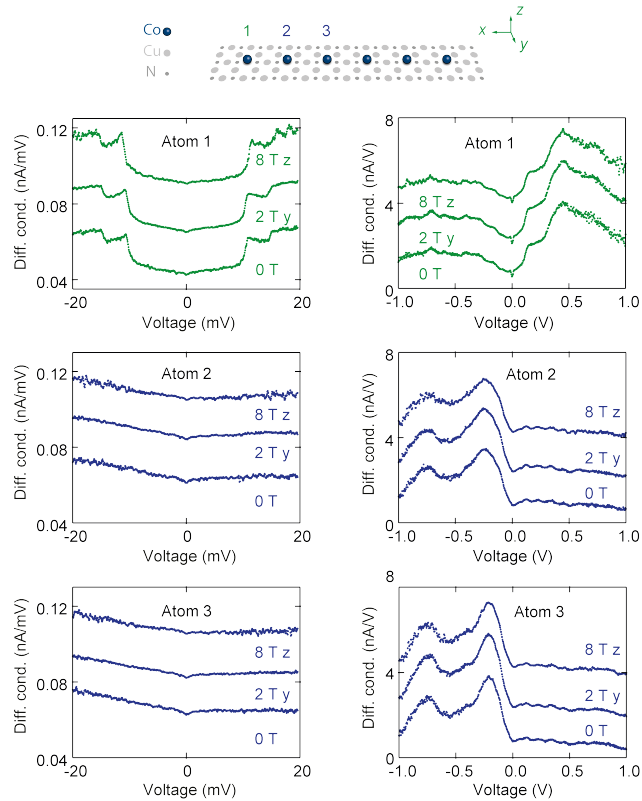


Figure 6.6: **Effect of magnetic field on spin and orbital excitation spectra of a Co nanostructure.**  $dI/dV$  spectra of the same Co hexamer as shown in Fig. 6.4, including data taken with magnetic field applied in the out of plane direction ( $z$ ) and in-plane, perpendicular to the chain direction ( $y$ ). Only the first three atoms are shown. For the end atom spin IETS spectra up to 20 mV, only the expected small Zeeman shift in excitation energies is observed. For the orbital IETS spectra up to 1 V, no change in the spectra is seen with applied field.

bital IETS transitions involve tunneling on and off different orbitals, creating an orbital excited state. The energy cost of these transitions will be the crystal field splitting, which is of order several hundred millielectronvolts [5]. No substantial change in either spin or orbital IETS spectra are seen with applied magnetic field (Fig. 6.6).

### 6.3. SUPPRESSION MECHANISM IN SPIN AND ORBITAL EXCITATIONS

The combined suppression of both spin IETS and orbital IETS transitions can be understood in terms of a simple qualitative model. The  $d_{z^2}$  orbital of the magnetic atom dominates transport between the tip and the atom; the other  $d$  orbitals couple only to the substrate. Therefore, all spin and orbital cotunneling excitations must involve the  $d_{z^2}$  orbital [159]. In case the  $d_{z^2}$  orbital is half-filled (Fig. 6.5a), spin and orbital excitations

are allowed for both voltage polarities. This is the case for single Co atoms and for outer atoms of chains. If the  $d_{z^2}$  orbital is fully occupied, however, spin excitations are blocked completely and orbital excitations can occur only at negative sample voltage (Fig. 6.5b), as observed for inner atoms.

The change in filling of the  $d_{z^2}$  orbital may be due to changes in the crystal environment of the Co atom, particularly the N ligands. Density functional theory (DFT) calculations, carried out using Quantum Espresso (QE)26 with PAW pseudopotentials and PBE exchange correlation functional, (Fig. 6.5c,d) indicate that for inner atoms of Co chains, the N-Co-N angle  $\theta$  is almost collinear ( $175^\circ$ ), whereas for a single Co atom  $\theta = 150^\circ$ . This drastic change in structure influences the atom's magnetocrystalline anisotropy.

## 6.4. MAGNETIC ANISOTROPY OF CO ATOMIC CHAINS

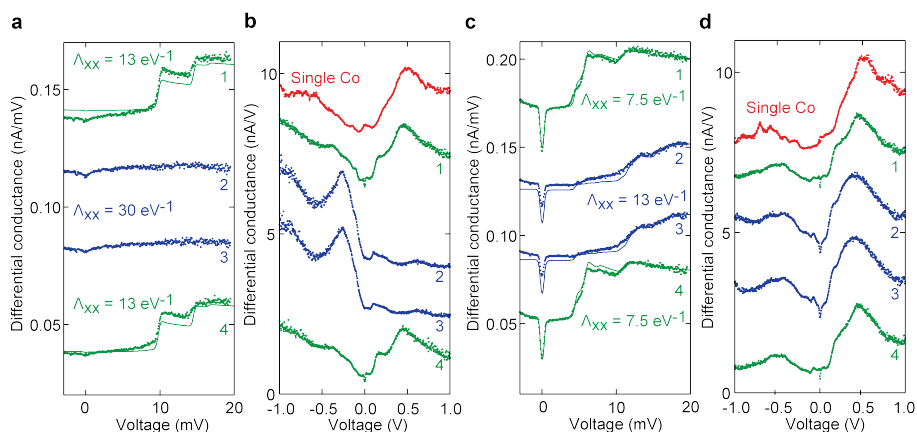
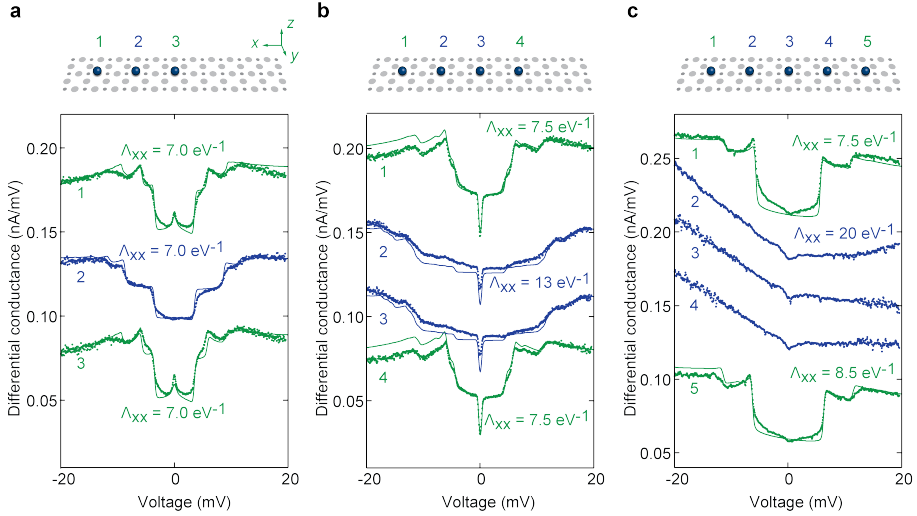


Figure 6.7: **Magnetic anisotropy of Co nanostructures.** **a** IETS spectra of each atom of a Co tetramer built on  $\text{Cu}_2\text{N}$ . Solid lines are simulated spectra allowing the anisotropy parameter  $\Lambda_{xx}$  to vary as indicated between the end (green) and inner (blue) atoms.  $\Lambda_{zz} = 6.0 \text{ eV}^{-1}$  and  $\Lambda_{yy} = 0$  in all cases, the antiferromagnetic spin coupling is  $2.5 \text{ meV}$ . Single Co may be fitted with  $\Lambda_{xx} = 6.2 \text{ eV}^{-1}$ . Simulated spectra are not shown for inner atoms since the spin IETS transitions are suppressed. **b** Higher bias spectra on the same tetramer as **(a)**. Note suppression of the positive bias spectral features in the inner atoms (blue). **c** IETS spectra of each atom of another Co tetramer built on  $\text{Cu}_2\text{N}$  in which spin excitations are not suppressed. Simulated spectra are shown as for **(a)**. The antiferromagnetic spin coupling is  $2 \text{ meV}$ . **d** Higher bias spectra on the same tetramer as **(c)**. The spectra are all observed to be similar to that of a single Co atom (red). The conductance was  $1 \mu\text{S}$  for the  $20 \text{ mV}$  spectra and  $2 \text{ nS}$  for  $1 \text{ V}$ .

The influence of the structural DFT prediction on anisotropy can be verified by spin IETS spectra, which show that Co atoms assembled into chains show a substantial anisotropy enhancement compared to single atoms. Fig. 6.7a,b show IETS spectra of a tetramer; as before, on the inner atoms spin excitations are suppressed as well as positive-bias orbital excitations. Without spin IETS steps on the inner atoms, we cannot directly measure their magnetic anisotropy. However, in a minority of cases (4 out of 20 structures) we observed Co N-row chains in which spin excitations on the inner atoms were not



**Figure 6.8: Co nanostructures with suppressed and unsuppressed spin excitations.** In most cases, Co chains longer than two atoms built on  $\text{Cu}_2\text{N}$  showed suppressed spin excitations on the inner atoms (6.1). In a minority of cases (4 out of 20 structures), Co chains up to four atoms long were observed to have unsuppressed spin excitations. This effect was specific to certain locations on the substrate, and is presumably due to variations in local strain induced by subsurface defects. **a**  $dI/dV$  spectra of each atom of a Co trimer and **(b)** a Co tetramer, as shown in Fig. 6.7c, constructed as an extension of the trimer. Both structures show unsuppressed spin excitations. Simulated spin IETS spectra are shown (solid lines), for all atoms  $S = 3/2$ ,  $\Lambda_{zz} = 6.2 \text{ eV}^{-1}$ ,  $\Lambda_{yy} = 0$ . The trimer may be fitted with  $\Lambda_{xx} = 7.0 \text{ eV}^{-1}$  for all atoms: for the tetramer  $\Lambda_{xx} = 7.5 \text{ eV}^{-1}$  for the end atoms and  $13 \text{ eV}^{-1}$  for the inner atoms. For both structures the antiferromagnetic spin coupling is  $2 \text{ meV}$ ,  $J_K \rho_s = -0.05 \text{ meV}$  for inner atoms and  $-0.15 \text{ meV}$  for the end atoms. **c**  $dI/dV$  spectra of a Co pentamer constructed as an extension of **(b)**. In this case no spin IETS steps are seen on the inner atoms: suppression of spin excitations was observed on all structures longer than four atoms. We may conclude that the strain induced by adding a Co atom to the structure overcomes the local lattice strain, pushing all inner atoms of the structure beyond the critical N-Co-N angle that leads to suppression of spin excitations. The end atom spectra may be simulated using a similar model to Fig. 6.3: for all atoms  $S = 3/2$ ,  $J_K \rho_s = -0.05 \text{ meV}$ ,  $\Lambda_{zz} = 6.2 \text{ eV}^{-1}$ ,  $\Lambda_{yy} = 0$ , the antiferromagnetic spin coupling is  $2 \text{ meV}$ . For the end atoms  $\Lambda_{xx} = 7.5$  and  $8.5 \text{ eV}^{-1}$ , for the inner atoms  $\Lambda_{xx} = 20 \text{ eV}^{-1}$ . Note that the anisotropy values are smaller than in Fig. 6.3, illustrating the effect of the local strain.

6

suppressed (Fig. 6.7c and Fig. 6.8). Significantly, in these cases all atoms also show the prominent orbital IETS peak close to  $+500 \text{ mV}$  (Fig. 6.7d), reinforcing the correlation of suppression of spin and positive-bias orbital transitions. We believe that in these minority cases all the atoms of the chain have a partially occupied  $d_{z^2}$  orbital.

We can fit simulated spin IETS spectra to all the atoms of the “unsuppressed” chain (Fig. 6.7c) and the end atoms of the “suppressed” chain (Fig. 6.7a) by varying only the component  $\Lambda_{xx}$  of the anisotropy tensor  $\Lambda$ , [62, 91] corresponding to the chain axis ( $x$ ) direction. Simulated IETS spectra are produced by diagonalization of a spin Hamiltonian that includes nearest-neighbor Heisenberg exchange interaction as well as magnetic anisotropy in terms of a second-order perturbative treatment of the spin-orbit coupling [62, 63]. Resulting lineshapes are generated by taking interactions with the substrate electrons into account up to third order [116, 150]. The anisotropy of the inner atoms of the “suppressed” chain may be estimated by its effect on the outer atom spectra. We find

that all atoms have a larger  $\Lambda_{xx}$  than a single Co atom and that the inner atoms of both chains have a larger  $\Lambda_{xx}$  than the outer atoms. Moreover, all atoms of the “suppressed” chain have a larger anisotropy than those of the “unsuppressed” chain. This effect may be understood in terms of changes in the crystal field: as  $\theta$  approaches  $180^\circ$  the crystal field approaches the high-symmetry linear case, and the magnetic anisotropy increases rapidly [5]. Because the inner atoms of the “suppressed” chain have the largest  $\Lambda_{xx}$  we can infer that they have  $\theta$  closest to  $180^\circ$ . End atoms of chains have smaller  $\theta$  because they have only one Co neighbor: hence they have smaller  $\Lambda_{xx}$  than the inner atoms.

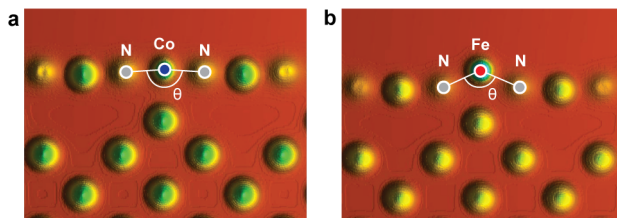


Figure 6.9: **Comparison of Co chains and Fe chains on Cu<sub>2</sub>N.** **a** Section through DFT-computed relaxed structure of an infinite chain of Co atoms on Cu<sub>2</sub>N, as shown in Fig. 6.5d. The N-Co-N angle  $\theta$  is  $175^\circ$ , leading to strong hybridization of the  $d_{z^2}$  orbital and suppression of spin excitations. **b** Relaxed structure of an infinite chain of Fe atoms on Cu<sub>2</sub>N. The N-Fe-N angle  $\theta$  is much smaller at  $133^\circ$ , so in this case the  $d_{z^2}$  orbital is not strongly hybridized and spin excitations are not suppressed.

We compared DFT simulations of the magnetization density for different Co structures on Cu<sub>2</sub>N (Fig. 6.5e,f). For a single Co atom, the magnetization profile in the  $xz$  plane has a  $d_{xz} + d_{z^2}$  character, but for an inner atom of a chain it shows the perfect 4-fold symmetry of the  $d_{xz}$  orbital, indicating that the  $d_{z^2}$  orbital is no longer contributing to magnetism. This is due in part to hybridization of the Co  $d_{z^2}$  orbital with the N ligand orbitals, which occurs because the N-Co-N angle  $\theta$  is almost  $180^\circ$ . The hybridization results in a nonmagnetic  $d_{z^2}$  projection and so is equivalent in its effect on the  $z$ -axis electron transport to a fully filled  $d_{z^2}$  orbital. Thus, we have a mechanism whereby a transition to a higher-symmetry crystal environment leads to a modification of the orbital filling and an effectively fully filled, nonmagnetic  $d_{z^2}$  orbital. This effect is not observed for chains of Fe on Cu<sub>2</sub>N [32]; these show a smaller  $\theta$  (Fig. 6.9) and hence are not expected to show strong hybridization effects. Similarly, Co dimers and the end atoms of Co chains have smaller  $\theta$  than inner atoms due to their asymmetric environment. Thus, they always show a smaller magnetic anisotropy and unsuppressed spin excitations.

DFT calculations using relaxed structures consistently overestimate orbital hybridization [160], thereby reducing the Co spin. This overestimation means that while we can model the qualitative effect of changing  $\theta$ , it is not possible to theoretically predict the precise angle  $\theta$  at which the transition to a nonmagnetic  $d_{z^2}$  orbital occurs. To demonstrate the correlation between  $\theta$  and the magnetization profile, we have shown in Fig. 6.5c a monomer with reduced N-Co-N angle  $\theta = 110^\circ$  for which  $S = 3/2$ , which is in agreement with experiment.

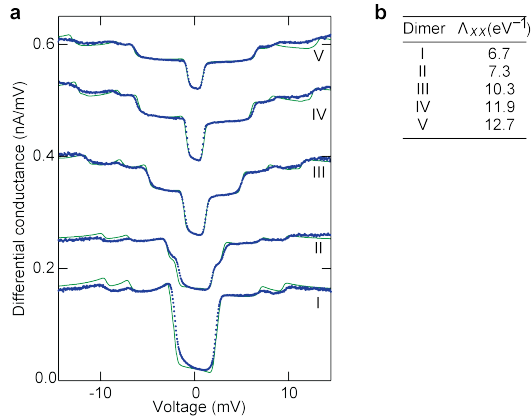


Figure 6.10: **Anisotropy variation in Co dimers.** **a**  $dI/dV$  spectra (dots) and simulated spin IETS spectra (solid lines) recorded on five instances of Co dimers, all constructed in the same way with two unit-cell spacing along the direction of the neighboring N atoms ( $x$ -axis), on a  $\text{Cu}_2\text{N}$  substrate. Substantial variation in spectroscopic features was observed. **b** Best fit values for  $\Lambda_{xx}$  for all dimers shown in (a): for all atoms  $S = 3/2$ ,  $J_K\rho_s = -0.15$  meV,  $\Lambda_{zz} = 6.2 \text{ eV}^{-1}$ ,  $\Lambda_{yy} = 0$  and the antiferromagnetic spin coupling is 2 meV. No correlation was found between the  $\Lambda_{xx}$  values and either the distance of the dimer from the edge of the  $\text{Cu}_2\text{N}$  island, or the size of the supporting island. Therefore, the variation in anisotropy is attributed to strain induced by subsurface defects. The anisotropy is highly sensitive to small changes in strain, since the N-Co-N angle  $\theta$  is already close to  $180^\circ$ .

## 6

We can account for the two different types of N-row structures shown in Fig. 6.7 by variation in local strain. Single Co atoms on  $\text{Cu}_2\text{N}$  show just a  $\pm 5\%$  variation in anisotropy; this is similar to that observed for Fe atoms and dimers on the same surface, which was attributed to local lattice strain caused by subsurface defects [61, 62]. Co N-row dimers and chains however are highly sensitive to strain; dimers were observed to show nearly a factor of 2 variation in anisotropy (Fig. 6.10 and [63]). This occurs because  $\theta$  is already close to  $180^\circ$ , so a small change in lattice strain can drive a large change in anisotropy. Strain can also cause  $\theta$  to reach the critical value that triggers the transition to a hybridized  $d_{z^2}$  orbital, suppressing spin and orbital excitations. All structures longer than four atoms were observed to have suppressed spin transitions on the inner atoms; when extended to four or five atoms, structures were observed to revert to “suppressed” behavior (Fig. 6.8), suggesting that the nanostructure’s own strain field can overcome the local lattice strain for sufficiently long chains.

## 6.5. CONCLUSIONS

We have demonstrated how modifications in the crystal environment of a single Co atom can result in complete closure of both spin and orbital cotunneling paths. A small variation in an external parameter (strain) can effectively turn spin excitations on and off, similar to the role of a gate voltage changing the occupancy of a quantum dot from odd to even [156]. In the present experiment, we can controllably modify this strain by

adding an extra atom to a nanostructure (Fig. 6.1 and Fig. 6.8). We suggest that if magnetic nanostructures were assembled on a piezoelectric substrate, it would be possible to control the global strain, providing a method to tune orbital occupancy, and thereby inelastic channel closure, through a separate voltage signal.



# 7

## PROBING ORBITAL-SPECIFIC EXCITATIONS IN SINGLE ATOMS

*As already shown in previous chapters of this thesis, STM at low temperature is a successful tool for probing local density of states with atomic precision. In certain cases – such as molecules adsorbed directly on metals [161–169] or on thin insulating layers [170–175] and impurity bound states in superconductors [176] – the spatial resolution of the STM allows even tunneling into specific electron orbitals. However, due to the finite curvature of the STM tip, orbital-specific topography is much more difficult to obtain on individual atoms. Here we report on a 1 K STM study of the spatial distribution of inelastic excitation intensity on individual Co adatoms on a Cl-reconstructed Cu(111) surface. By performing IETS along three crystallographically equivalent directions of a Co atom in the Cl surface plane, we find a continuous evolution in the asymmetry of IETS steps as a function of position, with the symmetry reaching a maximum in the vicinity of the three binding Cl neighbors. The observations can be explained qualitatively when considering the expected locations of uncompensated electron spins in the crystal field split atomic  $d$  orbitals. Further confirmation is provided by density functional theory (DFT) calculations, supporting our interpretation of inelastic spectroscopy with subatomic resolution.*

---

This chapter describes work in preparation for journal submission by **R. Toskovic**, M.C. Martinez Velarte, J. Girovsky, M. Kokken, J.W. González<sup>§</sup>, F. Delgado<sup>†</sup>, and A.F. Otte. Theory results supporting this chapter were obtained by J.W. González<sup>§</sup> and F. Delgado<sup>†</sup>.

<sup>§</sup> Materials Physics Center, San Sebastián, Spain

<sup>†</sup> Departamento de Física, Universidad de La Laguna, San Cristóbal de La Laguna, Spain

## 7.1. CO ADATOMS ON CL-RECONSTRUCTED CU(111) SURFACE

As shown in chapter 4, we obtained an insulating hexagonal Cl-reconstruction on Cu(111) crystal that provides clean flat areas for adatom evaporation and manipulation. Upon evaporation, STM topography reveals both single Co adatoms and larger structures atop the Cl surface network, with individual adatoms dominating the landscape. The two characteristic topographic features appear as rotationally symmetric over  $120^\circ$  and  $360^\circ$ . The features resemble the shapes of equilateral triangles (Fig. 7.1) and arrows (Fig. 7.3), respectively. DFT predictions on the possible binding sites for Co on this surface show a good match with the adatom shapes we see in topography.

First, we will focus on the features with triangular topographic appearance. These come in two varieties. The first one is mentioned above ( $120^\circ$  symmetric feature shown in Fig. 7.1) and causes almost no visible displacement in the position of the Cl atoms in the underlying lattice appearing rotated w.r.t. to the Cl-lattice (we call this a rotated triangle or an RT type). This is also the ground state for the binding site for a Co adatom on this surface as found by DFT. The second type is always associated with a Cl-lattice defect (1D displacement of Cl atoms of lengths up to tens of nanometers, missing Cl atoms etc.) and appears as either an upwards pointing triangle (U) or a downwards pointing triangle (D) (shown in Fig. 7.2). For reasons of symmetry and because it is predicted to be the ground state binding configuration, we will focus our study on the RT type.

### RT ADATOM

As can be seen in Fig. 7.1b, the RT adatom comes in two distinguishable forms (denoted with  $RT_1$  and  $RT_2$ ). DFT reveals the binding site to be the hollow (fcc) position, equidistantly separated from the three nearest Cl neighbors. Moreover, there are exactly two positions a Co adatom can occupy under that condition on this surface (Fig. 7.1a). Dependent on which of the two positions it sits on, the Co adatom is expected to induce an equal rotation of the three neighboring Cl atoms in a clockwise ( $RT_1$ ) or an anti-clockwise ( $RT_2$ ) manner. Comparison to STM topography indeed shows only these two configurations for this adatom type and a good match with the measured rotation angle ( $15^\circ$ ). Topography does not allow for imaging of the Cl atoms forming bonds with the Co adatom, which is supported by the theoretical finding that the orbitals close to Fermi level contributing dominantly to the density of states are  $d$  orbitals of Co with  $p$  orbitals of three Cl neighbors contributing with  $< 10\%$  each. Nevertheless, the subtle displacement of the underlying Cl atoms is, with a very sharp tip, to an extent apparent in topography.

IETS on the RT adatom type ( $RT_1$  and  $RT_2$  configurations are indistinguishable in spectroscopy) reveals asymmetric peak positions at  $-4.4$  mV and  $+8.4$  mV and, overall, an asymmetric spectrum shape (Fig. 7.1c), which is atypical of spin excitations on magnetic adatoms. In section 7.2 we will discuss further the spectroscopy signature of this adatom type. RT adatoms are observed also on an undersaturated Cl surface (Fig. 7.4a). Coverage of Cl plays a role in IETS features we detect on RT adatoms. Namely, on the RT adatoms on the undersaturated surface presented in Fig. 7.4a we see a small shift to the left in the IETS features compared to the saturated case for negative voltages (here, the IETS peaks are detected at  $-5$  mV and  $+7.6$  mV).

### U/D ADATOM

Next to the discussed RT form, triangular adatoms frequently appear in a U/D configuration (Fig. 7.2a). The exact Cl surface reconstruction associated with this binding site is not unique and stems from particular defects in the underlying Cl reconstruction. Also, DFT does not predict this triangular configuration for a Co adatom. Therefore, the exact binding site of this type of adatom will not be analyzed further.

Compared to the RT spectrum, IETS on U/D reveals a shift and broadening of the peak on the negative side (positioned at  $-6.2$  mV) and a suppression of the peak on the positive side that is for U/D barely detectable. U and D are indistinguishable in spectra (Fig. 7.2b). U/D adatom type appears on over-saturated Cl surfaces as well (Fig. 7.4b). Its IETS spectrum is very similar to the U/D found on the saturated surface, with the negative bias peak pushed to lower energies: here it is found at  $-5.7$  mV.

### A ADATOM

The next Co binding site on this surface we will discuss is of the arrow type (A). This type appears in three distinct directions on this surface, labeled as "East" (E), "North-West" (NW) and "South-West" (SW) (Fig. 7.3a). This finding is supported by DFT which shows a Co adatom with this binding site to be equidistantly positioned between two Cl atoms, occupying a position between the Cu site from the top layer and a neighboring hollow site along the Cl-Co-Cl direction not occupied by a Cl atom (Fig. 7.3b). In addition to this, DFT predicts the Cl atom closer to the Cu site to be higher compared to the other Cl atom (both Cl atoms are predicted to be higher than the Co adatom), with a 20 pm difference. This is in agreement with the 1D adatom shape with the adatom appearing higher at one end, always pointing in one of three directions, defining an arrow-like adatom shape.

IETS on the A-type adatom has an asymmetric V-shape around zero-bias, with a 1.6 mV sharp feature on the negative voltage side and an approx. 3 times broader slope for positive voltages. Spectra on A-type adatoms in the three directions (E, NW, SW) are identical (Fig. 7.3c). A-type adatoms appear on the undersaturated surface as well (Fig. 7.4a) with a more symmetric V-shape IETS spectrum compared to the case on the saturated surface (here, IETS peaks are detected at  $-2.4$  mV and  $+3$  mV). Note the slope on the positive voltage side is 2 times higher compared to an A-adatom on the saturated surface.

## 7.2. ORBITAL-SPECIFICITY IN INELASTIC EXCITATIONS

Ideally, the non-spin polarized IETS spectrum of magnetic adatoms is characterized by symmetrically positioned steps symmetric around zero voltage (neglecting higher order tunnelling terms and saturation effects) [116]. A peculiarity in the excitation spectrum of the RT adatom embodied in the asymmetric spectrum with the negative bias side having a significantly higher spectral weight and the positive bias peak barely distinguishable initiated performing IETS spectroscopy off the center of the adatom. We performed line spectroscopy with 40 pm resolution along the three symmetry directions of the adatoms and found that as the STM tip is moved from the adatom center towards a corner of the adatom, symmetry is gained until the symmetric IETS steps are recovered in the corner. The result is shown in Fig. 7.5. The behavior follows a 3-fold symmetry as it is observed in all three RT corners (see Fig. 7.6).

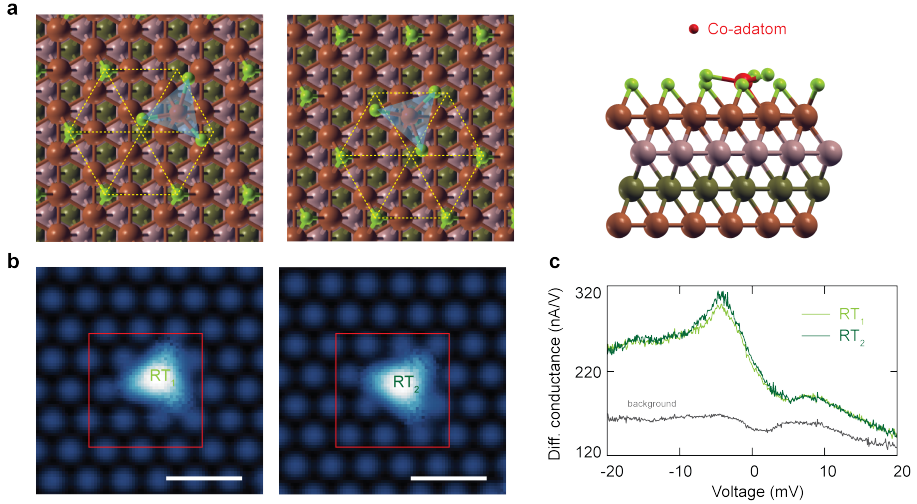


Figure 7.1: **Ground state binding configuration for Co adatom on 1/3ML  $\sqrt{3} \times \sqrt{3}R30^\circ$  Cl-reconstructed Cu(111) – “rotated triangle” (RT).** **a** Two equivalent ground state (GS) binding configurations for Co adatom on a  $\sqrt{3} \times \sqrt{3}R30^\circ$  Cl-reconstructed Cu(111) as obtained from DFT. Left: top view showing the Co adatom in a hollow fcc site forming 3 equidistant bonds with nearest Cl neighbours slightly pulling them away from their original (fcc) positions towards the neighbouring hollow (hcp) positions in a CW manner. Middle: Its counterpart formed by a  $15^\circ$  CCW rotation of its 3 closest Cl neighbours. Right: side view showing the Co adatom position as slightly lower compared to the bonding Cl atoms. Color code as in Fig. 4.9b. **b** STM topographic images ( $I = 100$  pA,  $V = 20$  mV,  $T = 1.17$  K) depicting the two configurations (RT<sub>1</sub> and RT<sub>2</sub>) in which we find Co adatoms on this surface corresponding to DFT findings in (a). Red squares encircle DFT areas shown in (a). The adatoms appear as equilateral triangles formed by a  $15^\circ$  CW (left) or a CCW (right) rotation of its 3 closest Cl neighbours (c.w. left and middle panels in (a)). Scale bar 1 nm. **c** IETS taken on instances of these two types of adatoms. No differences observed in spectral shape and feature position and intensity. Spectroscopy settings:  $V_{\text{mod}} = 100$   $\mu$ V,  $T = 1.17$  K.

In an attempt to understand the origin of these excitations, we will take a look at the DFT and multiplet calculations.

DFT results point towards  $d$  orbitals of the Co adatom to be responsible for most of the DOS seen in  $dI/dV$  signal. Fig. 7.7a shows that, around Fermi level, Co's  $d$  orbitals contribute dominantly to the total DOS. Looking into individual orbitals, DFT finds the in-plane orbitals of the Co adatom,  $d_{x^2-y^2}$  and  $d_{xy}$  to be degenerate and closest to the Fermi level (upper panel in Fig. 7.7b), indicating they are partially filled and responsible for spin excitations in the Co adatom. Contribution of the  $p$  orbitals of the three neighboring Cl atoms seems to be non-negligible around the Fermi level while the  $d$  orbitals of the nearest three Cu neighbors don't play an important role at this energy scale. Therefore, we conclude that the low-energy IETS on the RT adatom is influenced by both transport through its  $d$  orbitals and transport through the  $p$  orbitals of the neighboring Cl atoms which are presumably hybridized. Before analyzing this further, let us take a look at the effect of the exact electronic configuration on the  $d$  orbitals of the RT adatom.

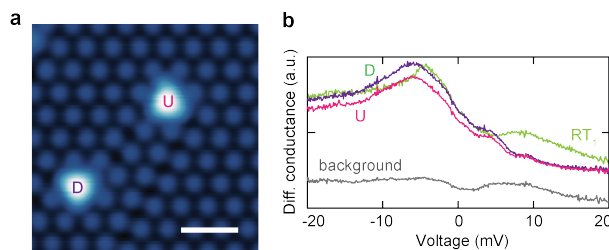


Figure 7.2: **Observation of the “up/down” (U/D) triangle binding site for Co-adatom on  $1/3$  ML  $\sqrt{3}R30^\circ$  Cl-reconstructed Cu(111).** **a** Topography shows the two configurations (“up” and “down”) of this type of triangular adatom. Notice the changes in the underlying Cl lattice that always accompany this adatom type. Imaging setpoint:  $I = 100$  pA,  $V = 20$  mV,  $T = 1.17$  K; scale bar 1 nm. **b** Corresponding IETS spectra taken on instances of these two triangle adatom types with the same STM tip used for spectroscopy on RT adatoms from Fig. 7.1. For comparison, a spectrum for RT<sub>1</sub> adatom from Fig. 7.1 is plotted as well. For U/D adatoms, the peak shifts towards higher energies for negative voltage polarities in comparison to the ground state (RT) configuration. Notice the difference in sharpness of this peak compared to the RT adatom. Also, peak on the positive voltage side rises at a higher energy compared to the RT case. Background offset for clarity. IETS settings:  $V_{\text{mod}} = 100$   $\mu$ V,  $T = 1.17$  K.

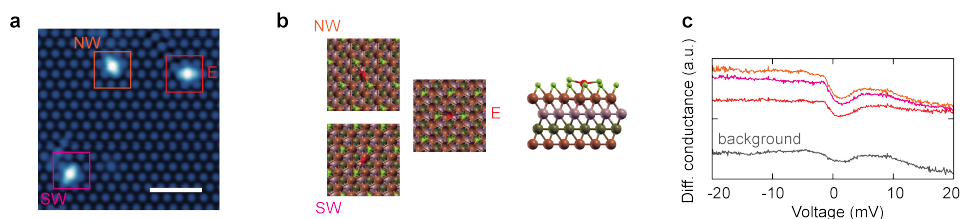


Figure 7.3: **First excited state binding configuration for Co adatom on  $1/3$ ML  $\sqrt{3}R30^\circ$  Cl-reconstructed Cu(111) – “arrow” (A).** **a** STM topography of three Co adatoms in a linear geometry configuration. Each Co adatom connects two Cl atoms along three  $120^\circ$ -split directions, forming arrow-like features. The only three possible pointing directions for arrow-like adatoms – North-West (NW), East (E) and South-West (SW) – are shown here. Imaging setpoint:  $I = 100$  pA,  $V = 20$  mV,  $T = 1.17$  K; scale bar 2 nm. **b** Corresponding binding sites as obtained from DFT. Areas correspond to the squares encircling adatoms in topography in (a). Co adatom has two nearest Cl neighbours and occupies the hollow hcp site in-between resulting in its non-equidistant placement between the two Cl atoms and therefore unique pointing vector in all three directions. To the far right a side view for this binding configuration showing Co adatom with a bonding asymmetry along the Cl-Co-Cl direction appearing slightly lower compared to the Cl atoms it binds to. Color code for DFT results as in Figs. 4.9b and 7.1a. **c** Corresponding IETS spectra taken on instances of these three arrow types with the same STM tip used for spectroscopy on RT adatoms from Fig. 7.1. Notice no difference in spectroscopy for the three pointing directions. Spectra offset for clarity. IETS settings:  $V_{\text{mod}} = 100$   $\mu$ V,  $T = 1.17$  K.

Multiplet calculations take into account the effect of crystal field, orbital hopping, spin-orbit coupling and magnetic field. We analyze the low-energy spectrum of a Co adatom that emerges as a result of these interactions. The multiplet calculations were performed for three values of  $d$  orbital occupancy, namely  $d^7$ ,  $d^8$  and a mixed<sup>1</sup> configuration  $d^{7.82}$ .

<sup>1</sup>This number for the mixed configuration,  $n_d = 7.82$ , follows from the analysis of the occupancy vs. on-site energy of the  $d$  orbital (energy needed to add an electron to an initially empty  $d$  orbital) (Fig. 7.8a).

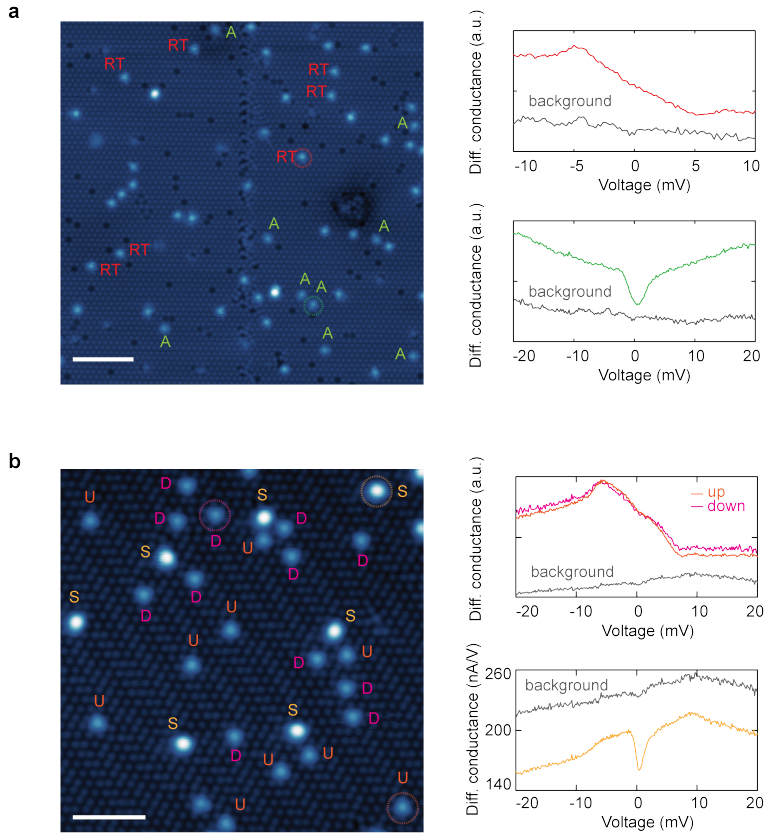


Figure 7.4: Co adatoms on under- and over-saturated Cl-reconstructed Cu(111) surfaces. **a** Left: STM topography of under-saturated Cl surface after Co evaporation. Many different features can be observed with only two reproducible adatom types: arrow (A) as the more common one and rotated triangle (RT). Imaging setpoint:  $I = 10$  pA,  $V = -30$  mV; scale bar 5 nm. Right: Characteristic IETS spectra for these two adatom types (RT in red, A in green). Selected adatoms for IETS encircled by dashed lines in topography on the left. Background spectrum offset for clarity for both adatoms. IETS settings:  $V_{\text{mod}} = 200$   $\mu$ V,  $T = 1.16$  K. **b** Left: STM topography depicting an area of over-saturated Cl-reconstructed Cu(111) after Co evaporation. Notice a higher degree of reproducibility compared to (a). Surface features appear in two varieties predominantly: up/down pointing triangles (U/D) and irregular spherical-like objects (S). Imaging setpoint:  $I = 100$  pA,  $V = 20$  mV,  $T = 1.17$  K; scale bar 3 nm. Right: Characteristic IETS spectra for these two feature types. Notice no difference between U and D configurations. Selected features for IETS encircled by dashed lines in topography on the left. Background spectrum offset for clarity for U/D adatoms. IETS taken at  $T = 1.16$  K.

Our IETS measurements reveal one step excitation in a  $dI/dV$  spectrum, at  $\pm 5.5$  mV (Fig. 7.5). Also, IETS reveals this step retaining its position as magnetic field is increased up to 3 T (Fig. 7.6). The lower extreme for  $d$  orbital occupancy, the  $d^7$  configuration, is discarded as the possibility due to the multiplet calculations predicting eight low-energy states with energies  $\leq 5$  meV, which would suggest more than one step in the low bias IETS spectrum of the adatom. For the case of higher  $d$  orbital occupancy extreme,  $d^8$ , multiplet unravels in a form of two energy levels below 10 meV and their field depen-

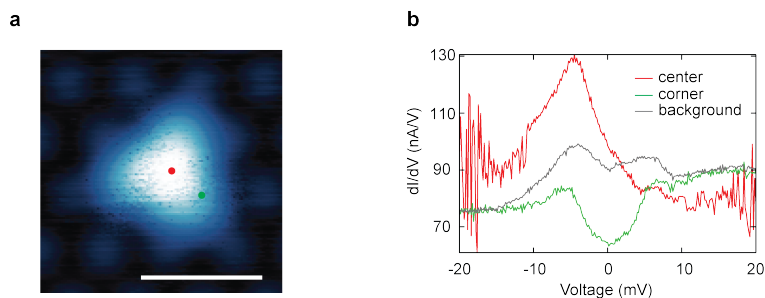


Figure 7.5: **Off-center spectroscopy on RT adatom.** **a** STM topographic image of an RT adatom type. Positions where the IETS spectra shown in **(b)** are marked in red (center) and green (corner). Dot size corresponds to the lateral spatial resolution with which IETS was done (40 pm). Imaging performed at  $I = 100$  pA,  $V = 20$  mV,  $T = 1.28$  K; scale bar 1 nm. Distance between the positions  $d = 0.32$  nm and the angle with the horizontal  $38.4^\circ$ . **b** IETS taken in the center and one corner of the RT adatom, together with the background. Symmetric excitations observed only at the corner position. IETS settings:  $V_{\text{mod}} = 160$   $\mu\text{V}$ ,  $T = 1.28$  K.

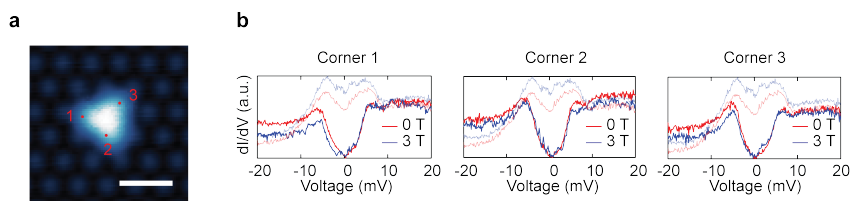


Figure 7.6: **Magnetic field IETS measurements in RT corners.** **a** STM topographic image of an RT adatom type. Corner positions where the IETS spectra shown in **(b)** are marked with green dots and labeled with numbers 1–3. Dot size corresponds to the lateral spatial resolution with which IETS was done (50 pm). Imaging performed at  $I = 100$  pA,  $V = 20$  mV,  $T = 1.28$  K; scale bar 1 nm. **b** IETS taken at three corners of the RT adatom at 0 T (red) and 3 T (blue) out-of-plane of the sample, shown together with the background (opaque dashed lines; field color coding the same as for the corners). IETS settings:  $V_{\text{mod}} = 160$   $\mu\text{V}$ ,  $T = 1.28$  K.

dence is small ( $\sim 1$  meV / 10 T). This is more in accordance with our adatom spectrum. The final, and most probable  $d$  orbital configuration as obtained by DFT,  $d^{7.82}$ , gives similar findings in terms of low-energy excitations, namely two lowest excitations below 10 meV and small field dependence (Fig. 7.8b).

The notion of the  $d^{7.82}$  occupancy as the most realistic case is further reinforced by transport calculations. They considered coupling of the STM tip (taken as an  $s$  orbital) to both Co adatom and three neighboring Cl atoms. More specifically, the coupling to following orbitals were considered separately:  $d_{z^2}$  of the Co adatom and  $p_x$ ,  $p_y$  and  $p_z$  of the Cl's. Individual effect of each of these orbitals was accounted for in the transport calculation for the low energy  $dI/dV$  curves. These simulations show IETS steps around 5 meV when tip is coupled to the  $d_{z^2}$  orbital of Co only for configurations  $d^{7.82}$  and  $d^8$  (Fig. 7.9a). When the tip is coupled to  $p_x$  and  $p_y$  orbitals of neighboring Cl atoms, IETS steps around 5 meV are reproduced as well, and in this case only for the transition configuration  $d^{7.82}$  (Fig. 7.9b). The latter finding is of particular interest to us as it provides a

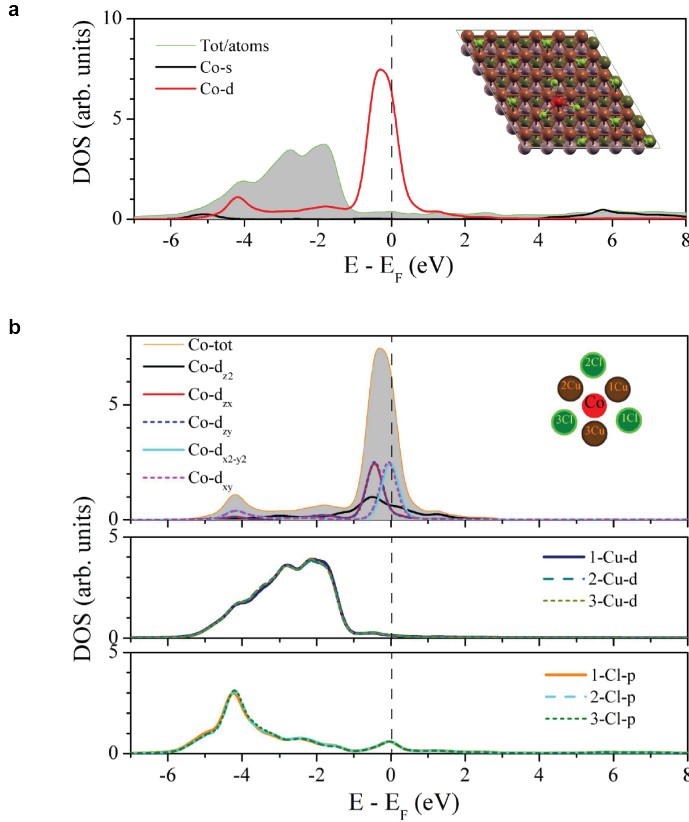


Figure 7.7: **Density of states (DOS) on the RT adatom – contribution of different atomic orbitals.** **a** DOS in  $(-8 : 8)$  V bias window with total contributions of  $d$  and  $s$  orbitals of the Co adatom together with total contribution from Cu and Cl atoms in the unit cell used for calculations (depicted in inset). DOS contributions shown are normalized by the number of corresponding atoms in the DFT unit cell. **b** Partial (normalized) most significant contributions to the DOS:  $d$  orbitals of the Co adatom,  $d$  orbitals of the nearest three Cu atoms and  $p$  orbitals of the nearest three Cl atoms (all relevant atoms depicted in inset).

hint towards understanding the symmetrization of IETS steps near the corners of the RT adatom. Therefore, current theory understanding suggests we are probing not only the orbitals from the Co adatom, but also the in-plane orbitals of the three Cl atoms that form bonds with the Co adatom.

Low excitation energies in IETS (order of meV) on a  $3d$  adatom together with DFT prediction of spin-1 system for  $d^{7.82}$  (Fig. 7.8c) suggest we are probing spin excitations. However, exposing the adatom to 3 T perpendicular to the sample surface causes no observable shift at 1 K in IETS spectra (Fig. 7.6). This experimental finding poses the question of the nature of the excitation we are seeing in our spectra. The multiplet does show a small variation of the lowest excitation energy with field. However, the highest magnetic field available on the system we used for studying this adatom (JT STM) was

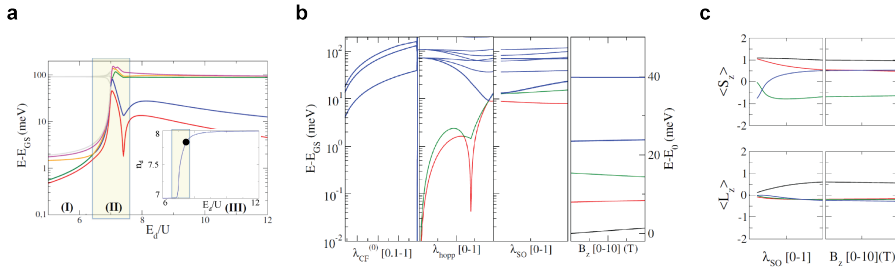


Figure 7.8: **Multiplet calculations for the RT adatom.** **a** Lowest five energy excitations evolving through a charge transition  $d^7 x^1 \rightarrow d^8 x^0$  ( $x$  – any orbital that is not a Co  $d$  orbital in the calculations) as a function of on-site energy of the  $d$  orbitals of Co ( $E_d$ ). Left region (I) has a  $d^7$  electronic configuration and region on the right (III)  $d^8$ . Charge transition region (II) in between is captured with a rectangle. Inset shows Co's  $d$  orbital occupancy ( $n_d$ ) as a function of  $E_d$ . Panels **(b)** and **(c)** show calculations for  $n_d = 7.82$  (black dot in the inset). **b** Multiplet calculations showing, from left to right, effects of crystal field ( $\lambda_{CF}$ ), hopping between orbitals ( $\lambda_{hop}$ ), spin-orbit coupling ( $\lambda_{SO}$ ) and magnetic field ( $B_z$ ). **c** Expectation values for the spin ( $\langle S_z \rangle$ ) and orbital ( $\langle L_z \rangle$ ) angular momenta along field direction.

3 T (for which a change of less than a 0.5 meV is expected) which, when taking into account broadening by 1 K and 100  $\mu$ V IETS modulation, is at the detection limit. Without applying higher magnetic field and observable step shift with field we cannot claim this excitation is magnetic in origin. We made an attempt on repeating this experiment on the  $^3\text{He}$  STM, where 9 T out of plane is available. This was unfortunately unsuccessful as we could not obtain individual Co adatoms on the Cl surface, presumably due to the evaporation taking place on a sample at a temperature  $> 60$  K.

### 7.3. ADATOM MANIPULATION

To manipulate the Co adatoms on the hexagonal Cl-reconstructed Cu(111), we used two methods – a vertical method of voltage pulsing and a lateral method of atom dragging. By performing voltage pulsing in the 1 – 2 nm vicinity of two Co adatoms, we can create a Co dimer. Higher level of control over directional movement was achieved through dragging adatoms and we are able to bring two Co adatoms to a sub-nanometer distance and resolve them individually.

Fig. 7.10a shows an example of voltage pulsing performed on two RT-type adatoms with initial positions shown in panel 1, resulting in the final configuration of two A-type adatoms in 8. This type of manipulation is performed with STM tip at one of the corners of the RT adatom (no preference for the corner) with feedback on and 100 pA tunneling current and voltage pulse applied for  $\Delta t = 5 - 10$  s. A number of observations will be reported.

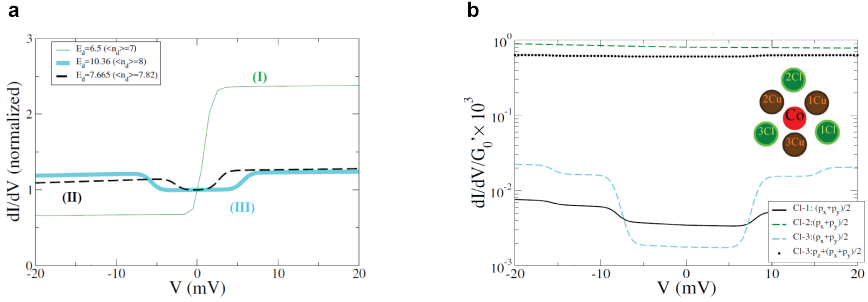


Figure 7.9: **Individual atomic orbital contributions to  $dI/dV$  of the RT adatom.** **a** STM tip is coupled to the  $d_{z^2}$  orbital of the Co adatom. Results shown for all 3 charge regions. Simulated  $dI/dV$  curves normalized by conductance value at  $V = 0$  (line thicknesses show relative intensities of  $dI/dV(V = 0)$ ). **b** STM tip is coupled to  $p$  orbitals of the three nearest Cl atoms. Numbering of Cl atoms same as in Fig. 7.7b (see inset). Results shown for the transition region, with  $n_d = 7.82$ .

As long as the pulse applied is  $120 \text{ mV} \leq V_{\text{pulse}} \leq 140 \text{ mV}$ , the RT adatom will either change its configuration (i.e. change its configuration type from  $RT_1$  to  $RT_2$  or vice versa) or it will undergo a translation to another position on the Cl-lattice (with or without changing its configuration type). Unfortunately, direction of adatom's movement after pulsing is random, which makes building of atomic structures challenging. These events are depicted in panels 1–3. From those panels, it can be seen that the the RT movement does not induce changes in the underlying Cl-reconstruction.

## 7

In the pulse range  $150\text{--}190 \text{ mV}$ , the RT adatom changes its binding site and this is accompanied with a defect creation in the underlying lattice (panels 3–4 or 6–7). The resulting binding site is no longer of the RT type and the adatom appears differently in topography. This adatom is more stable compared to the RT-type and cannot be converted back to the RT-type. These adatoms that are associated with Cl-lattice deformations are irregular in shape and will not be a subject of any further analysis (their IETS spectra, like their topographic appearance, is not uniform and resembles the one of the RT-type).

Upon applying pulses  $200 \text{ mV}$  (or higher), the adatom assumes a new binding configuration – the one of the A-type (panels 4–5 or 7–8). Once this configuration is reached, no further manipulation is possible – the A-configuration is stable up to  $\pm 1 \text{ V}$  (higher pulses applied atop this adatom type typically result in the tip change).

Direction reproducibility problems associated with pulsing manipulation have been overcome by the dragging technique. Here, the STM tip is positioned at the corner of the RT adatom, as in the case of pulsing, but with a higher current setpoint,  $700 \text{ pA}$ . The dragging is performed by directing the tip in between the Cl atoms with the voltage of  $+120 \text{ mV}$  applied. As can be seen from Fig. 7.10b, this type of manipulation does not lead to deformations of the underlying surface. Also, this is a faster approach to move adatoms to a desired location as the randomness in movement is much smaller compared to applying high voltage pulses at one corner.

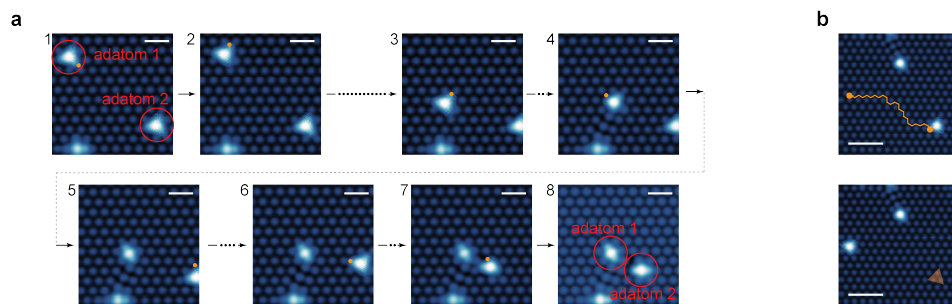


**Figure 7.10: Single Co adatom manipulation.** **a** Manipulation by voltage pulsing. Two atoms in their GS binding configuration (RT adatoms in panel 1) are brought in proximity by means of voltage pulsing. Pulsing was done at RT corners as depicted by orange dots. A full arrow represents one pulsing event and arrow with dots several, the number of which is indicated by the relative arrow lengths. Manipulation chronology as follows: 1→2 adatom 1 changes binding site from RT<sub>1</sub> to RT<sub>2</sub>; 2→3 adatom 1 moved by a series of successive pulses; 3→4 change of binding configuration for RT<sub>1</sub> and creation of defect in the underlying lattice; 4→5 RT<sub>1</sub> converted into an A-type adatom pointing NW; 5→6 movement of adatom 2 towards adatom 1; 6→7 change of binding configuration for RT<sub>2</sub> and creation of defect in the underlying lattice; 7→8 RT<sub>2</sub> converted into an A-type adatom pointing E. Topographies taken at  $I = 100$  pA,  $V = 20$  mV,  $T = 1.17$  K; scale bar 1 nm. **b** Manipulation by dragging. Feedback on with 700 pA. Tip positioned at one of the corners of the RT adatom as depicted by the orange dot in the topography on the top. With  $V = +120$  mV adatom is dragged along a zigzag path in-between the Cl atoms as depicted in the same image (orange line in top panel) until its final position shown in topography below (orange triangle indicates the initial position). Topographies taken at  $I = 100$  pA,  $V = 20$  mV,  $T = 1.17$  K; scale bar 2 nm.

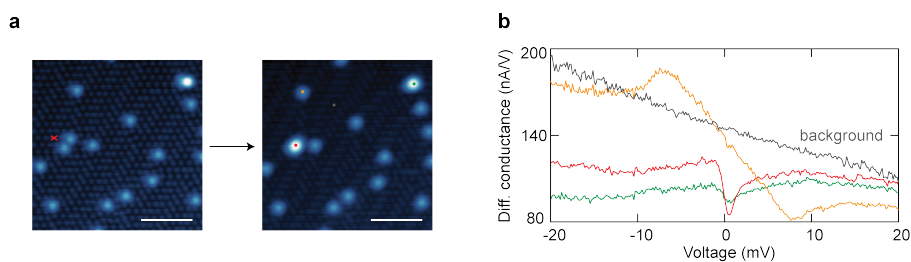


**Figure 7.11: Co dimers.** **a** Formation of a Co dimer. Left: A voltage pulse ( $V_{\text{pulse}} = 2.5$  V,  $t = 2$  s) is applied between the two adatoms as depicted in the topography (feedback on with  $I = 100$  pA). Right: A dimer is formed. Imaging performed at  $I = 100$  pA,  $V = 20$  mV; scale bar 3 nm. **b** Spectroscopy of the Co dimer (IETS settings:  $V_{\text{mod}} = 100$   $\mu$ V,  $T = 1.17$  K). IETS on the pulse-created dimer shown in red as compared to the naturally found round-shaped feature with similar topographic appearance with spectrum shown in green. Notice the characteristic dip around zero-bias for both cases. For comparison, an IETS of a down-pointing triangle is shown in orange.

Manipulation of single adatoms of Co on this surface has been employed to create atomic dimers as well by means of both dragging (explained above) and voltage pulsing. The voltage pulsing for generating artificial dimers was done by equidistantly positioning the STM tip typically within 1–2 nm away from the two adatoms and applying +2.5 V for  $\Delta t = 2 - 5$  s with 100 pA tunneling current feedback.

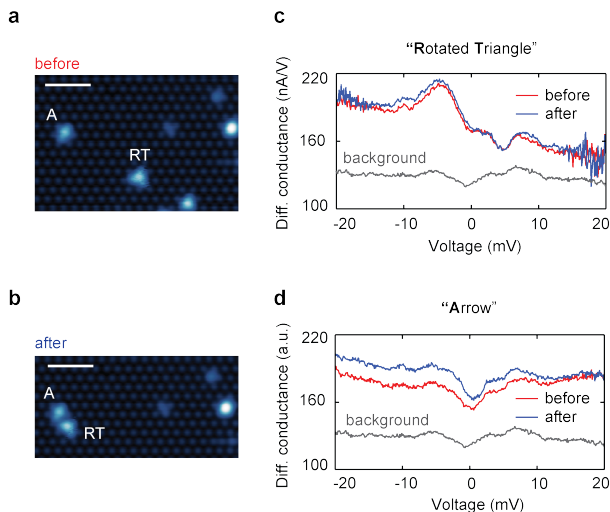


Figure 7.12: **Exchange interaction between Co adatoms.** Two Co adatoms are brought to proximity by means of STM manipulation. **a, b** STM topographic images taken before (**a**) and after (**b**) manipulating the RT-type Co adatom towards the A-type Co adatom. Imaging performed at  $I = 100$  pA,  $V = 20$  mV,  $T = 1.17$  K; scale bar 2 nm. **c, d** IETS taken before and after manipulation on the RT (**c**) and the A (**d**) Co adatom ( $V_{\text{mod}} = 200$   $\mu$ V,  $T = 1.17$  K). No differences observed when adatoms are brought to 0.7 nm proximity (**d**) as compared to the case of isolated adatoms (**c**) with 3.8 nm separation. In (**d**) red curve is offset for clarity.

## 7

The Co dimers appear as somewhat irregular round features in STM topography, broader and noticeably higher than the single adatoms (typical height:  $\sim 200$  pm). They are found together with single adatoms after Co evaporation (e.g. Fig. 7.4b and Fig. 7.11a). A characteristic IETS signature is a V-shaped spectrum, with an excitation around zero-bias (Fig. 7.4b and Fig. 7.11b). The IETS spectra on these naturally occurring dimers were used as an additional test to verify that the objects we created by placing two adatoms to sub-nanometer proximity are artificial dimers indeed. To verify this, a comparison between IETS of a naturally occurring dimer and an artificial one is given in Fig. 7.11b. The characteristic spectrum shape is present in both dimers, with a dip around zero voltage and the asymmetry in bias polarity.

To study potential exchange interaction between Co adatoms on this surface, we employed our dragging technique to bring two Co adatoms close together. The result is shown in Fig. 7.12. Positions of the two adatoms ("A" and "RT") prior to and after the STM manipulation are shown in panels **a** and **b**. Corresponding IETS spectra on the two adatoms are shown in panels **c** (on the "RT" adatom) and **d** (on the "A" adatom). By comparing the spectra taken on individual adatoms (situation in **a** – distance 3.8 nm) and when brought together (situation in **b** – distance 0.7 nm) do not seem to differ suggesting no exchange interaction is taking place between Co adatoms on this surface. With our technique, 0.7 nm is the limit to which we can bring the adatoms together without either converting an adatom into another adatom type (more specifically, "RT" into "A") or creating a dimer (when identifying individual adatoms is no longer possible).

## 7.4. CONCLUSIONS

We have shown for the first time a study on a  $3d$  adatom of Co on a Cl-reconstructed Cu(111) surface. Individual Co adatoms have been observed in STM topography and two commonly found bindings sites (RT and A) identified with a good match to DFT predictions. IETS reveals low-energy (meV) excitations on Co adatoms and we find strong and reproducible dependence of the IETS spectra on the binding site. RT adatom type was identified as the ground state binding configuration for Co adatom on this surface.

The surface, for geometry reasons, holds promise for building magnetically frustrated structures and we demonstrated a dragging manipulation technique able to bring two Co adatoms to sub-nanometer proximity. The adatoms do not seem to interact, however, indicating Co is not a good choice for building frustrated magnetic atomic structures on this surface. Moreover, the magnetic origin of the IETS excitations observed is inconclusive as we saw no shift in excitation energies with magnetic field.

Asymmetry in IETS seen on the RT adatom disappears atop Cl atoms forming bonds with the adatom. This, supported by DFT and transport calculations for the RT binding site, suggests STM tip is probing the in-plane  $d$  orbitals that are expected to be partially filled. To our knowledge, this is the first report of spatial mapping of individual atomic orbitals, demonstrating the capability of STM of performing spectroscopy with subatomic resolution.



# REFERENCES

- [1] V. Madhavan, W. Chen, T. Jamneala, M. Crommie, and N. Wingreen, *Tunneling into a single magnetic atom: spectroscopic evidence of the Kondo resonance*, *Science* **280**, 567 (1998).
- [2] A. Heinrich, J. Gupta, C. Lutz, and D. Eigler, *Single-atom spin-flip spectroscopy*, *Science* **306**, 466 (2004).
- [3] A. F. Otte, M. Ternes, K. Von Bergmann, S. Loth, H. Brune, C. P. Lutz, C. F. Hirjibehedin, and A. J. Heinrich, *The role of magnetic anisotropy in the Kondo effect*, *Nature Physics* **4**, 847 (2008).
- [4] F. Meier, L. Zhou, J. Wiebe, and R. Wiesendanger, *Revealing magnetic interactions from single-atom magnetization curves*, *Science* **320**, 82 (2008).
- [5] A. Otte, M. Ternes, S. Loth, C. Lutz, C. Hirjibehedin, and A. Heinrich, *Spin excitations of a Kondo-screened atom coupled to a second magnetic atom*, *Physical Review Letters* **103**, 107203 (2009).
- [6] S. Loth, M. Etzkorn, C. P. Lutz, D. Eigler, and A. J. Heinrich, *Measurement of fast electron spin relaxation times with atomic resolution*, *Science* **329**, 1628 (2010).
- [7] A. A. Khajetoorians, T. Schlenk, B. Schweflinghaus, M. dos Santos Dias, M. Steinbrecher, M. Bouhassoune, S. Lounis, J. Wiebe, and R. Wiesendanger, *Spin excitations of individual Fe atoms on Pt (111): impact of the site-dependent giant substrate polarization*, *Physical Review Letters* **111**, 157204 (2013).
- [8] J. C. Oberg, M. R. Calvo, F. Delgado, M. Moro-Lagares, D. Serrate, D. Jacob, J. Fernández-Rossier, and C. F. Hirjibehedin, *Control of single-spin magnetic anisotropy by exchange coupling*, *Nature Nanotechnology* **9**, 64 (2014).
- [9] I. G. Rau, S. Baumann, S. Rusponi, F. Donati, S. Stepanow, L. Gragnaniello, J. Dreiser, C. Piamonteze, F. Nolting, S. Gangopadhyay, *et al.*, *Reaching the magnetic anisotropy limit of a 3d metal atom*, *Science* **344**, 988 (2014).
- [10] T. Choi and J. A. Gupta, *Building blocks for studies of nanoscale magnetism: adsorbates on ultrathin insulating Cu<sub>2</sub>N*, *Journal of Physics: Condensed Matter* **26**, 394009 (2014).
- [11] F. Donati, A. Singha, S. Stepanow, C. Wäckerlin, J. Dreiser, P. Gambardella, S. Rusponi, and H. Brune, *Magnetism of Ho and Er atoms on close-packed metal surfaces*, *Physical Review Letters* **113**, 237201 (2014).
- [12] S. Baumann, W. Paul, T. Choi, C. P. Lutz, A. Ardavan, and A. J. Heinrich, *Electron paramagnetic resonance of individual atoms on a surface*, *Science* **350**, 417 (2015).
- [13] S. Baumann, F. Donati, S. Stepanow, S. Rusponi, W. Paul, S. Gangopadhyay, I. Rau, G. Pacchioni, L. Gragnaniello, M. Pivetta, *et al.*, *Origin of perpendicular magnetic anisotropy and large orbital moment in Fe atoms on MgO*, *Physical Review Letters* **115**, 237202 (2015).

- [14] A. Khajetoorians, M. Steinbrecher, M. Ternes, M. Bouhassoune, M. dos Santos Dias, S. Lounis, J. Wiebe, and R. Wiesendanger, *Tailoring the chiral magnetic interaction between two individual atoms*, Nature Communications **7**, 10620 (2016).
- [15] F. Donati, S. Rusponi, S. Stepanow, C. Wackerlin, A. Singha, L. Persichetti, R. Baltic, K. Diller, F. Patthey, E. Fernandes, *et al.*, *Magnetic remanence in single atoms*, Science **352**, 318 (2016).
- [16] M. Steinbrecher, A. Sonntag, M. dos Santos Dias, M. Bouhassoune, S. Lounis, J. Wiebe, R. Wiesendanger, and A. Khajetoorians, *Absence of a spin-signature from a single Ho adatom as probed by spin-sensitive tunneling*, Nature Communications **7** (2016).
- [17] W. Paul, K. Yang, S. Baumann, N. Romming, T. Choi, C. P. Lutz, and A. J. Heinrich, *Control of the millisecond spin lifetime of an electrically probed atom*, Nature Physics **13**, 403 (2017).
- [18] F. D. Natterer, K. Yang, W. Paul, P. Willke, T. Choi, T. Greber, A. J. Heinrich, and C. P. Lutz, *Reading and writing single-atom magnets*, Nature **543**, 226 (2017).
- [19] N. Tsukahara, K.-i. Noto, M. Ohara, S. Shiraki, N. Takagi, Y. Takata, J. Miyawaki, M. Taguchi, A. Chainani, S. Shin, *et al.*, *Adsorption-induced switching of magnetic anisotropy in a single iron (II) phthalocyanine molecule on an oxidized Cu(110) surface*, Physical Review Letters **102**, 167203 (2009).
- [20] B. W. Heinrich, L. Braun, P. J. I., and F. K. J., *Protection of excited spin states by a superconducting energy gap*, Nature Physics **9**, 765 (2013).
- [21] P. Jacobson, T. Herden, M. Muenks, G. Laskin, O. Brovko, V. Stepanyuk, M. Ternes, and K. Kern, *Quantum engineering of spin and anisotropy in magnetic molecular junctions*, Nature Communications **6**, 8536 (2015).
- [22] C. F. Hirjibehedin, C. P. Lutz, and A. J. Heinrich, *Spin coupling in engineered atomic structures*, Science **312**, 1021 (2006).
- [23] X. Chen, Y.-S. Fu, S.-H. Ji, T. Zhang, P. Cheng, X.-C. Ma, X.-L. Zou, W.-H. Duan, J.-F. Jia, and Q.-K. Xue, *Probing superexchange interaction in molecular magnets by spin-flip spectroscopy and microscopy*, Physical Review Letters **101**, 197208 (2008).
- [24] A. A. Khajetoorians, J. Wiebe, B. Chilian, and R. Wiesendanger, *Realizing all-spin-based logic operations atom by atom*, Science **332**, 1062 (2011).
- [25] A. Spinelli, B. Bryant, F. Delgado, J. Fernandez-Rossier, and A. F. Otte, *Imaging of spin waves in atomically designed nanomagnets*, Nature Materials **13**, 782 (2014).
- [26] S. Nadj-Perge, I. K. Drozdov, J. Li, H. Chen, S. Jeon, J. Seo, A. H. MacDonald, B. A. Bernevig, and A. Yazdani, *Observation of Majorana fermions in ferromagnetic atomic chains on a superconductor*, Science **346**, 602 (2014).
- [27] B. Bryant, R. Toskovic, A. Ferron, J. L. Lado, A. Spinelli, J. Fernandez-Rossier, and A. F. Otte, *Controlled complete suppression of single-atom inelastic spin and orbital cotunneling*, Nano Letters **15**, 6542 (2015).
- [28] S. Yan, D.-J. Choi, J. A. Burgess, S. Rolf-Pissarczyk, and S. Loth, *Control of quantum magnets by atomic exchange bias*, Nature Nanotechnology **10**, 40 (2015).

- [29] D.-J. Choi, R. Robles, S. Yan, J. A. Burgess, S. Rolf-Pissarczyk, J.-P. Gauyacq, N. Lorente, M. Ternes, and S. Loth, *Entanglement-induced Kondo screening in atomic spin chains*, arXiv preprint arXiv:1507.04785 (2015).
- [30] R. Toskovic, R. van den Berg, A. Spinelli, I. Eliens, B. van den Toorn, B. Bryant, J.-S. Caux, and A. Otte, *Atomic spin-chain realization of a model for quantum criticality*, *Nature Physics* **12**, 656 (2016).
- [31] K. Yang, Y. Bae, W. Paul, F. D. Natterer, P. Willke, J. L. Lado, A. Ferrón, T. Choi, J. Fernández-Rossier, A. J. Heinrich, *et al.*, *Engineering the eigenstates of coupled spin-1/2 atoms on a surface*, *Physical Review Letters* **119**, 227206 (2017).
- [32] S. Loth, S. Baumann, C. P. Lutz, D. Eigler, and A. J. Heinrich, *Bistability in atomic-scale anti-ferromagnets*, *Science* **335**, 196 (2012).
- [33] A. A. Khajetoorians, J. Wiebe, B. Chilian, S. Lounis, S. Blügel, and R. Wiesendanger, *Atom-by-atom engineering and magnetometry of tailored nanomagnets*, *Nature Physics* **8**, 497 (2012).
- [34] S. Yan, L. Malavolti, J. A. Burgess, A. Droghetti, A. Rubio, and S. Loth, *Non-locally sensing the magnetic states of nanoscale antiferromagnets with an atomic spin sensor*, arXiv preprint arXiv:1601.02723 (2016).
- [35] I. Georgescu, S. Ashhab, and F. Nori, *Quantum simulation*, *Reviews of Modern Physics* **86**, 153 (2014).
- [36] M. Troyer and U.-J. Wiese, *Computational complexity and fundamental limitations to fermionic quantum Monte Carlo simulations*, *Physical Review Letters* **94**, 170201 (2005).
- [37] R. P. Feynman, *Simulating physics with computers*, *International Journal of Theoretical Physics* **21**, 467 (1982).
- [38] S. Lloyd, *Universal quantum simulators*, *Science* **273**, 1073 (1996).
- [39] E. Jané, G. Vidal, W. Dür, P. Zoller, and J. I. Cirac, *Simulation of quantum dynamics with quantum optical systems*, *Quantum Information & Computation* **3**, 15 (2003).
- [40] X.-L. Deng, D. Porras, and J. I. Cirac, *Effective spin quantum phases in systems of trapped ions*, *Physical Review A* **72**, 063407 (2005).
- [41] D. Porras, F. Marquardt, J. Von Delft, and J. I. Cirac, *Mesoscopic spin-boson models of trapped ions*, *Physical Review A* **78**, 010101 (2008).
- [42] A. Bermudez, D. Porras, and M. Martin-Delgado, *Competing many-body interactions in systems of trapped ions*, *Physical Review A* **79**, 060303 (2009).
- [43] G.-D. Lin, C. Monroe, and L.-M. Duan, *Sharp phase transitions in a small frustrated network of trapped ion spins*, *Physical Review Letters* **106**, 230402 (2011).
- [44] S. Korenblit, D. Kafri, W. C. Campbell, R. Islam, E. E. Edwards, Z.-X. Gong, G.-D. Lin, L. Duan, J. Kim, K. Kim, *et al.*, *Quantum simulation of spin models on an arbitrary lattice with trapped ions*, *New Journal of Physics* **14**, 095024 (2012).
- [45] J. J. Garcia-Ripoll, M. A. Martin-Delgado, and J. I. Cirac, *Implementation of spin Hamiltonians in optical lattices*, *Physical Review Letters* **93**, 250405 (2004).

- [46] J. Cho, D. G. Angelakis, and S. Bose, *Simulation of high-spin Heisenberg models in coupled cavities*, Physical Review A **78**, 062338 (2008).
- [47] A. Micheli, G. Brennen, and P. Zoller, *A toolbox for lattice-spin models with polar molecules*, Nature Physics **2**, 341 (2006).
- [48] D. I. Tsomokos, S. Ashhab, and F. Nori, *Using superconducting qubit circuits to engineer exotic lattice systems*, Physical Review A **82**, 052311 (2010).
- [49] D. Porras and J. I. Cirac, *Effective quantum spin systems with trapped ions*, Physical Review Letters **92**, 207901 (2004).
- [50] A. Friedenauer, H. Schmitz, J. T. Glueckert, D. Porras, and T. Schätz, *Simulating a quantum magnet with trapped ions*, Nature Physics **4**, 757 (2008).
- [51] E. Edwards, S. Korenblit, K. Kim, R. Islam, M.-S. Chang, J. Freericks, G.-D. Lin, L.-M. Duan, and C. Monroe, *Quantum simulation and phase diagram of the transverse-field Ising model with three atomic spins*, Physical Review B **82**, 060412 (2010).
- [52] B. P. Lanyon, C. Hempel, D. Nigg, M. Müller, R. Gerritsma, F. Zähringer, P. Schindler, J. Barreiro, M. Rambach, G. Kirchmair, *et al.*, *Universal digital quantum simulation with trapped ions*, Science **334**, 57 (2011).
- [53] K. Kim, M.-S. Chang, S. Korenblit, R. Islam, E. E. Edwards, J. K. Freericks, G.-D. Lin, L.-M. Duan, and C. Monroe, *Quantum simulation of frustrated Ising spins with trapped ions*, Nature **465**, 590 (2010).
- [54] K. Kim, S. Korenblit, R. Islam, E. Edwards, M. Chang, C. Noh, H. Carmichael, G. Lin, L. Duan, C. J. Wang, *et al.*, *Quantum simulation of the transverse Ising model with trapped ions*, New Journal of Physics **13**, 105003 (2011).
- [55] R. Islam, E. Edwards, K. Kim, S. Korenblit, C. Noh, H. Carmichael, G.-D. Lin, L.-M. Duan, C.-C. J. Wang, J. Freericks, *et al.*, *Onset of a quantum phase transition with a trapped ion quantum simulator*, arXiv preprint arXiv:1103.2400 (2011).
- [56] J. W. Britton, B. C. Sawyer, A. C. Keith, C.-C. J. Wang, J. K. Freericks, H. Uys, M. J. Biercuk, and J. J. Bollinger, *Engineered two-dimensional Ising interactions in a trapped-ion quantum simulator with hundreds of spins*, Nature **484**, 489 (2012).
- [57] M. Neeley, M. Ansmann, R. C. Bialczak, M. Hofheinz, E. Lucero, A. D. O'connell, D. Sank, H. Wang, J. Wenner, A. N. Cleland, *et al.*, *Emulation of a quantum spin with a superconducting phase qudit*, Science **325**, 722 (2009).
- [58] G. Roumpos, C. P. Master, and Y. Yamamoto, *Quantum simulation of spin ordering with nuclear spins in a solid-state lattice*, Physical Review B **75**, 094415 (2007).
- [59] M. Greiner, O. Mandel, T. Esslinger, T. W. Hänsch, and I. Bloch, *Quantum phase transition from a superfluid to a Mott insulator in a gas of ultracold atoms*, Nature **415**, 39 (2002).
- [60] E. Simon, B. Újfalussy, B. Lazarovits, A. Szilva, L. Szunyogh, and G. M. Stocks, *Exchange interaction between magnetic adatoms on surfaces of noble metals*, Physical Review B **83**, 224416 (2011).

- [61] C. F. Hirjibehedin, C.-Y. Lin, A. F. Otte, M. Ternes, C. P. Lutz, B. A. Jones, and A. J. Heinrich, *Large magnetic anisotropy of a single atomic spin embedded in a surface molecular network*, *Science* **317**, 1199 (2007).
- [62] B. Bryant, A. Spinelli, J. Wagenaar, M. Gerrits, and A. Otte, *Local control of single atom magnetocrystalline anisotropy*, *Physical Review Letters* **111**, 127203 (2013).
- [63] A. Spinelli, M. Gerrits, R. Toskovic, B. Bryant, M. Ternes, and A. Otte, *Exploring the phase diagram of the two-impurity Kondo problem*, *Nature Communications* **6** (2015).
- [64] P. Coleman and A. J. Schofield, *Quantum criticality*, *Nature* **433**, 226 (2005).
- [65] S. Sachdev, *Quantum criticality: competing ground states in low dimensions*, *Science* **288**, 475 (2000).
- [66] B. Lake, D. A. Tennant, C. D. Frost, and S. E. Nagler, *Quantum criticality and universal scaling of a quantum antiferromagnet*, *Nature Materials* **4**, 329 (2005).
- [67] P. Coleman, C. Pépin, Q. Si, and R. Ramazashvili, *How do Fermi liquids get heavy and die?* *Journal of Physics: Condensed Matter* **13**, R723 (2001).
- [68] J. Kurmann, H. Thomas, and G. Müller, *Antiferromagnetic long-range order in the anisotropic quantum spin chain*, *Physica A: Statistical Mechanics and its Applications* **112**, 235 (1982).
- [69] H. Bethe, *Zur theorie der metalle*, *Zeitschrift für Physik* **71**, 205 (1931).
- [70] P. W. Anderson, *Resonating valence bonds: A new kind of insulator?* *Materials Research Bulletin* **8**, 153 (1973).
- [71] E. Lieb, T. Schultz, and D. Mattis, *Two soluble models of an antiferromagnetic chain*, *Ann. Phys.* **16**, 407 (1961).
- [72] M. Mourigal, M. Enderle, A. Klöpperpieper, J.-S. Caux, A. Stunault, and H. M. Rønnow, *Fractional spinon excitations in the quantum Heisenberg antiferromagnetic chain*, *Nature Physics* **9**, 435 (2013).
- [73] P. Pfeuty, *The one-dimensional Ising model with a transverse field*, *Annals of Physics* **57**, 79 (1970).
- [74] S. Jalal and B. Kumar, *Edge modes in a frustrated quantum Ising chain*, *Physical Review B* **90**, 184416 (2014).
- [75] G. Vionnet, B. Kumar, and F. Mila, *Level crossings induced by a longitudinal coupling in the transverse field Ising chain*, *Physical Review B* **95**, 174404 (2017).
- [76] A. Y. Kitaev, *Unpaired Majorana fermions in quantum wires*, *Physics-Uspekhi* **44**, 131 (2001).
- [77] F. Mila, *Magnetic adatoms: When Ising meets Majorana*, *Nature Physics* (2016).
- [78] D. Dmitriev, V. Y. Krivnov, and A. Ovchinnikov, *Gap generation in the XXZ model in a transverse magnetic field*, *Physical Review B* **65**, 172409 (2002).
- [79] D. Dmitriev and V. Y. Krivnov, *Quasi-one-dimensional anisotropic Heisenberg model in a transverse magnetic field*, *JETP letters* **80**, 303 (2004).

- [80] L. Balents, *Spin liquids in frustrated magnets*, Nature **464**, 199 (2010).
- [81] X.-G. Wen, *Quantum orders and symmetric spin liquids*, Physical Review B **65**, 165113 (2002).
- [82] P. A. Lee, *An end to the drought of quantum spin liquids*, Science **321**, 1306 (2008).
- [83] F. Amiri, S. Mahdaviifar, H. Hadipour, and M. S. Naseri, *Thermodynamics of the Spin-1/2 Two-Leg Ladder Compound  $(C_5H_{12}N)_2CuBr_4$* , Journal of Low Temperature Physics **177**, 203 (2014).
- [84] F. Amiri, S. Mahdaviifar, and H. Hadipour, *Magnetization Process of the Spin-1/2 Two-Leg Ladder Compound  $(C_5H_{12}N)_2CuBr_4$ : The Jordan-Wigner Approach*, Journal of Superconductivity and Novel Magnetism **27**, 2379 (2014).
- [85] Z. Zhao, X. Liu, Z. He, X. Wang, C. Fan, W. Ke, Q. Li, L. Chen, X. Zhao, and X. Sun, *Heat transport of the quasi-one-dimensional Ising-like antiferromagnet  $BaCo_2V_2O_8$  in longitudinal and transverse fields*, Physical Review B **85**, 134412 (2012).
- [86] M. Matsuda, H. Onishi, A. Okutani, J. Ma, H. Agrawal, T. Hong, D. Pajerowski, J. Copley, K. Okunishi, M. Mori, *et al.*, *Magnetic structure and dispersion relation of the  $S = 1/2$  quasi-one-dimensional Ising-like antiferromagnet  $BaCo_2V_2O_8$  in a transverse magnetic field*, Physical Review B **96**, 024439 (2017).
- [87] Z. Saghafi, J. Jahangiri, S. Mahdaviifar, H. Hadipour, and S. F. Shayesteh, *Theoretical investigation of the behavior of  $CuSe_2O_5$  compound in high magnetic fields*, Journal of Magnetism and Magnetic Materials **398**, 183 (2016).
- [88] M. Kenzelmann, R. Coldea, D. Tennant, D. Visser, M. Hofmann, P. Smeibidl, and Z. Tylczynski, *Order-to-disorder transition in the XY-like quantum magnet  $Cs_2CoCl_4$  induced by noncommuting applied fields*, Physical Review B **65**, 144432 (2002).
- [89] O. Breunig, M. Garst, A. Rosch, E. Sela, B. Buldmann, P. Becker, L. Bohatý, R. Müller, and T. Lorenz, *Low-temperature ordered phases of the spin-1/2 XXZ chain system  $Cs_2CoCl_4$* , Physical Review B **91**, 024423 (2015).
- [90] D. Dmitriev, V. Y. Krivnov, A. Ovchinnikov, and A. Langari, *One-dimensional anisotropic Heisenberg model in the transverse magnetic field*, Journal of Experimental and Theoretical Physics **95**, 538 (2002).
- [91] D. Dai, H. Xiang, and M.-H. Whangbo, *Effects of spin-orbit coupling on magnetic properties of discrete and extended magnetic systems*, Journal of Computational Chemistry **29**, 2187 (2008).
- [92] A. F. Otte, *Magnetism of a single atom*, PhD thesis, Leiden University (2008).
- [93] O. Breunig, M. Garst, E. Sela, B. Buldmann, P. Becker, L. Bohatý, R. Müller, and T. Lorenz, *Spin-1/2 XXZ Chain System  $Cs_2CoCl_4$  in a Transverse Magnetic Field*, Physical Review Letters **111**, 187202 (2013).
- [94] B. Mühlischlegel, *Relation between the Anderson and Kondo Hamiltonians for the case of degenerate impurity orbitals*, Zeitschrift für Physik A Hadrons and Nuclei **208**, 94 (1968).
- [95] A. MacDonald, S. Girvin, and D. Yoshioka,  *$t/U$  expansion for the Hubbard model*, Physical Review B **37**, 9753 (1988).

- [96] M. Mancini, *Fermionization of spin systems*, MSc thesis, University of Perugia (2008).
- [97] P. Jordan and E. Wigner, *Über das Paulische Äquivalenzverbot*, *Zeitschrift für Physik* **47**, 631 (1928).
- [98] G. Binnig, H. Rohrer, C. Gerber, and E. Weibel, *Tunneling through a controllable vacuum gap*, *Applied Physics Letters* **40**, 178 (1982).
- [99] S. Pan, E. Hudson, and J. Davis,  *$^3\text{He}$  refrigerator based very low temperature scanning tunneling microscope*, *Review of Scientific Instruments* **70**, 1459 (1999).
- [100] J. Roebuck and H. Osterberg, *The Joule-Thomson effect in helium*, *Physical Review* **43**, 60 (1933).
- [101] J. Bardeen, *Tunnelling from a many-particle point of view*, *Physical Review Letters* **6**, 57 (1961).
- [102] J. Tersoff and D. Hamann, *Theory and application for the scanning tunneling microscope*, *Physical Review Letters* **50**, 1998 (1983).
- [103] J. Tersoff and D. Hamann, *Theory of the scanning tunneling microscope*, *Physical Review B* **31**, 805 (1985).
- [104] B. Stipe, M. Rezaei, and W. Ho, *Single-molecule vibrational spectroscopy and microscopy*, *Science* **280**, 1732 (1998).
- [105] M. A. Reed, *Inelastic electron tunneling spectroscopy*, *Materials Today* **11**, 46 (2008).
- [106] R. C. Jaklevic and J. Lambe, *Molecular vibration spectra by electron tunneling*, *Physical Review Letters* **17**, 1139 (1966).
- [107] J. Lambe and R. Jaklevic, *Molecular vibration spectra by inelastic electron tunneling*, *Physical Review* **165**, 821 (1968).
- [108] L. Lauhon and W. Ho, *Effects of temperature and other experimental variables on single molecule vibrational spectroscopy with the scanning tunneling microscope*, *Review of Scientific Instruments* **72**, 216 (2001).
- [109] M. Bode, *Spin-polarized scanning tunnelling microscopy*, *Reports on Progress in Physics* **66**, 523 (2003).
- [110] R. Wiesendanger, H.-J. Güntherodt, G. Güntherodt, R. Gambino, and R. Ruf, *Observation of vacuum tunneling of spin-polarized electrons with the scanning tunneling microscope*, *Physical Review Letters* **65**, 247 (1990).
- [111] D. T. Pierce, *Spin-polarized electron microscopy*, *Physica Scripta* **38**, 291 (1988).
- [112] R. Wiesendanger, *Spin mapping at the nanoscale and atomic scale*, *Reviews of Modern Physics* **81**, 1495 (2009).
- [113] T. K. Yamada, M. Bischoff, T. Mizoguchi, and H. Van Kempen, *Use of voltage pulses to detect spin-polarized tunneling*, *Applied Physics Letters* **82**, 1437 (2003).

- [114] L. Berbil-Bautista, S. Krause, M. Bode, and R. Wiesendanger, *Spin-polarized scanning tunneling microscopy and spectroscopy of ferromagnetic Dy(0001)/W(110) films*, Physical Review B **76**, 064411 (2007).
- [115] S. Loth, K. Von Bergmann, M. Ternes, A. F. Otte, C. P. Lutz, and A. J. Heinrich, *Controlling the state of quantum spins with electric currents*, Nature Physics **6**, 340 (2010).
- [116] M. Ternes, *Spin excitations and correlations in scanning tunneling spectroscopy*, New Journal of Physics **17**, 063016 (2015).
- [117] K. von Bergmann, M. Ternes, S. Loth, C. P. Lutz, and A. J. Heinrich, *Spin polarization of the split Kondo state*, Physical Review Letters **114**, 076601 (2015).
- [118] T. Choi, C. Ruggiero, and J. Gupta, *Incommensurability and atomic structure of  $c(2 \times 2) N/Cu(100)$* , arXiv preprint arXiv:0805.3324 (2008).
- [119] M. Ternes, A. J. Heinrich, and W.-D. Schneider, *Spectroscopic manifestations of the Kondo effect on single adatoms*, Journal of Physics: Condensed Matter **21**, 053001 (2008).
- [120] T. Choi, C. Ruggiero, and J. Gupta, *Tunneling spectroscopy of ultrathin insulating  $Cu_2N$  films, and single Co adatoms*, Journal of Vacuum Science & Technology B: Microelectronics and Nanometer Structures Processing, Measurement, and Phenomena **27**, 887 (2009).
- [121] N. Knorr, M. A. Schneider, L. Diekhöner, P. Wahl, and K. Kern, *Kondo effect of single Co adatoms on Cu surfaces*, Physical Review Letters **88**, 096804 (2002).
- [122] P. Wahl, L. Diekhöner, M. Schneider, L. Vitali, G. Wittich, and K. Kern, *Kondo temperature of magnetic impurities at surfaces*, Physical Review Letters **93**, 176603 (2004).
- [123] N. Néel, J. Kröger, L. Limot, K. Palotas, W. Hofer, and R. Berndt, *Conductance and Kondo effect in a controlled single-atom contact*, Physical Review Letters **98**, 016801 (2007).
- [124] M. Etzkorn, C. Hirjibehedin, A. Lehnert, S. Ouazi, S. Rusponi, S. Stepanow, P. Gambardella, C. Tieg, P. Thakur, A. Lichtenstein, *et al.*, *Comparing XMCD and DFT with STM spin excitation spectroscopy for Fe and Co adatoms on  $Cu_2N/Cu(100)$* , Physical Review B **92**, 184406 (2015).
- [125] A. Spinelli, *Quantum magnetism through atomic assembly*, PhD thesis, Delft University of Technology (2015).
- [126] M. A. Ruderman and C. Kittel, *Indirect exchange coupling of nuclear magnetic moments by conduction electrons*, Physical Review **96**, 99 (1954).
- [127] T. Kasuya, *A theory of metallic ferro- and antiferromagnetism on Zener's model*, Progress of Theoretical Physics **16**, 45 (1956).
- [128] K. Yosida, *Magnetic properties of Cu-Mn alloys*, Physical Review **106**, 893 (1957).
- [129] P. Wahl, P. Simon, L. Diekhöner, V. Stepanyuk, P. Bruno, M. Schneider, and K. Kern, *Exchange interaction between single magnetic adatoms*, Physical Review Letters **98**, 056601 (2007).
- [130] L. Zhou, J. Wiebe, S. Lounis, E. Vedmedenko, F. Meier, S. Blügel, P. H. Dederichs, and R. Wiesendanger, *Strength and directionality of surface Ruderman-Kittel-Kasuya-Yosida interaction mapped on the atomic scale*, Nature Physics **6**, 187 (2010).

- [131] J. Kanamori, *Superexchange interaction and symmetry properties of electron orbitals*, Journal of Physics and Chemistry of Solids **10**, 87 (1959).
- [132] J. B. Goodenough, *An interpretation of the magnetic properties of the perovskite-type mixed crystals  $La_{1-x}Sr_xCoO_{3-\lambda}$* , Journal of Physics and Chemistry of Solids **6**, 287 (1958).
- [133] F. Kalf, M. P. Rebergen, E. Fahrenfort, J. Girovsky, R. Toskovic, J. L. Lado, J. Fernández-Rossier, and A. F. Otte, *A kilobyte rewritable atomic memory*, Nature Nanotechnology **11**, 926 (2016).
- [134] S. Peljhan and A. Kokalj, *Adsorption of Chlorine on Cu(111): A Density-Functional Theory Study*, The Journal of Physical Chemistry C **113**, 14363 (2009).
- [135] K. Doll and N. Harrison, *Chlorine adsorption on the Cu(111) surface*, Chemical Physics Letters **317**, 282 (2000).
- [136] T. V. Pavlova, B. V. Andryushechkin, and G. M. Zhidomirov, *First-Principle Study of Adsorption and Desorption of Chlorine on Cu(111) Surface: Does Chlorine or Copper Chloride Desorb?* The Journal of Physical Chemistry C **120**, 2829 (2016).
- [137] B. Andryushechkin, V. Zheltov, V. V. Cherkez, G. Zhidomirov, A. Klimov, B. Kierren, Y. Fagot-Révurat, D. Malterre, and K. Eltsov, *Chlorine adsorption on Cu(111) revisited: LT-STM and DFT study*, Surface Science **639**, 7 (2015).
- [138] A. Heinrich, *Atomic spins on surfaces*, Physics Today **68**, 42 (2015).
- [139] S. Wolf, D. Awschalom, R. Buhrman, J. Daughton, S. Von Molnar, M. Roukes, A. Y. Chtchelkanova, and D. Treger, *Spintronics: a spin-based electronics vision for the future*, Science **294**, 1488 (2001).
- [140] A. Spinelli, M. Rebergen, and A. Otte, *Atomically crafted spin lattices as model systems for quantum magnetism*, Journal of Physics: Condensed Matter **27**, 243203 (2015).
- [141] W. Heisenberg, *Zur theorie des ferromagnetismus*, Zeitschrift für Physik **49**, 619 (1928).
- [142] T. Giamarchi, *Quantum physics in one dimension*, Vol. 121 (Oxford university press, 2004).
- [143] S. Sachdev, *Quantum Phase Transitions* (Cambridge University Press, 2011).
- [144] R. Elliott, P. Pfeuty, and C. Wood, *Ising model with a transverse field*, Physical Review Letters **25**, 443 (1970).
- [145] J. Fernández-Rossier, *Theory of single-spin inelastic tunneling spectroscopy*, Physical Review Letters **102**, 256802 (2009).
- [146] P. Lecheminant, *Frustrated spin systems* (World-Scientific, 2005).
- [147] J. Fransson, O. Eriksson, and A. Balatsky, *Theory of spin-polarized scanning tunneling microscopy applied to local spins*, Physical Review B **81**, 115454 (2010).
- [148] J. Kondo, *Resistance minimum in dilute magnetic alloys*, Progress of Theoretical Physics **32**, 37 (1964).
- [149] J. A. Appelbaum, *Exchange model of zero-bias tunneling anomalies*, Physical Review **154**, 633 (1967).

- [150] Y.-h. Zhang, S. Kahle, T. Herden, C. Stroh, M. Mayor, U. Schlickum, M. Ternes, P. Wahl, and K. Kern, *Temperature and magnetic field dependence of a Kondo system in the weak coupling regime*, *Nature Communications* **4** (2013).
- [151] S. De Franceschi, S. Sasaki, J. Elzerman, W. Van Der Wiel, S. Tarucha, and L. P. Kouwenhoven, *Electron cotunneling in a semiconductor quantum dot*, *Physical Review Letters* **86**, 878 (2001).
- [152] T. S. Jespersen, K. Grove-Rasmussen, J. Paaske, K. Muraki, T. Fujisawa, J. Nygård, and K. Flensberg, *Gate-dependent spin-orbit coupling in multielectron carbon nanotubes*, *Nature Physics* **7**, 348 (2011).
- [153] A. S. Zyazin, J. W. van den Berg, E. A. Osorio, H. S. van der Zant, N. P. Konstantinidis, M. Leijnse, M. R. Wegewijs, F. May, W. Hofstetter, C. Danieli, *et al.*, *Electric field controlled magnetic anisotropy in a single molecule*, *Nano Letters* **10**, 3307 (2010).
- [154] A. A. Khajetoorians, B. Chilian, J. Wiebe, S. Schuwalow, F. Lechermann, and R. Wiesendanger, *Detecting excitation and magnetization of individual dopants in a semiconductor*, *Nature* **467**, 1084 (2010).
- [155] F. Delgado and J. Fernández-Rossier, *Cotunneling theory of atomic spin inelastic electron tunneling spectroscopy*, *Physical Review B* **84**, 045439 (2011).
- [156] A. Kogan, S. Amasha, D. Goldhaber-Gordon, G. Granger, M. Kastner, and H. Shtrikman, *Measurements of Kondo and spin splitting in single-electron transistors*, *Physical Review Letters* **93**, 166602 (2004).
- [157] B. W. Heinrich, L. Braun, J. I. Pascual, and K. J. Franke, *Tuning the magnetic anisotropy of single molecules*, *Nano letters* **15**, 4024 (2015).
- [158] R. Schleser, T. Ihn, E. Ruh, K. Ensslin, M. Tews, D. Pfannkuche, D. Driscoll, and A. Gossard, *Cotunneling-mediated transport through excited states in the Coulomb-blockade regime*, *Physical Review Letters* **94**, 206805 (2005).
- [159] J. Kügel, M. Karolak, J. Senkpiel, P.-J. Hsu, G. Sangiovanni, and M. Bode, *Relevance of hybridization and filling of 3d orbitals for the Kondo effect in transition metal phthalocyanines*, *Nano Letters* **14**, 3895 (2014).
- [160] N. Zaki, H. Park, R. M. Osgood, A. J. Millis, and C. A. Marianetti, *Failure of DFT-based computations for a stepped-substrate-supported correlated Co wire*, *Physical Review B* **89**, 205427 (2014).
- [161] R. Temirov, S. Soubatch, O. Neucheva, A. Lassise, and F. Tautz, *A novel method achieving ultra-high geometrical resolution in scanning tunnelling microscopy*, *New Journal of Physics* **10**, 053012 (2008).
- [162] C. Weiss, C. Wagner, C. Kleimann, M. Rohlfing, F. Tautz, and R. Temirov, *Imaging Pauli repulsion in scanning tunneling microscopy*, *Physical Review Letters* **105**, 086103 (2010).
- [163] M. Lennartz, V. Caciuc, N. Atodiresei, S. Karthäuser, and S. Blügel, *Electronic mapping of molecular orbitals at the molecule-metal interface*, *Physical Review Letters* **105**, 066801 (2010).

- [164] W.-H. Soe, C. Manzano, A. De Sarkar, N. Chandrasekhar, and C. Joachim, *Direct observation of molecular orbitals of pentacene physisorbed on Au(111) by scanning tunneling microscope*, Physical Review Letters **102**, 176102 (2009).
- [165] X. Lu, M. Grobis, K. Khoo, S. G. Louie, and M. Crommie, *Spatially mapping the spectral density of a single C<sub>60</sub> molecule*, Physical Review Letters **90**, 096802 (2003).
- [166] J. Schwöbel, Y. Fu, J. Brede, A. Dilullo, G. Hoffmann, S. Klyatskaya, M. Ruben, and R. Wiesendanger, *Real-space observation of spin-split molecular orbitals of adsorbed single-molecule magnets*, Nature Communications **3**, 953 (2012).
- [167] L. Bartels, *Tailoring molecular layers at metal surfaces*, Nature Chemistry **2**, 87 (2010).
- [168] M. Lackinger and W. Heckl, *A STM perspective on covalent intermolecular coupling reactions on surfaces*, Journal of Physics D: Applied Physics **44**, 464011 (2011).
- [169] M. Feng, J. Zhao, and H. Petek, *Atomlike, hollow-core-bound molecular orbitals of C<sub>60</sub>*, Science **320**, 359 (2008).
- [170] L. Gross, N. Moll, F. Mohn, A. Curioni, G. Meyer, F. Hanke, and M. Persson, *High-resolution molecular orbital imaging using a p-wave STM tip*, Physical Review Letters **107**, 086101 (2011).
- [171] J. Repp, G. Meyer, S. M. Stojković, A. Gourdon, and C. Joachim, *Molecules on insulating films: scanning-tunneling microscopy imaging of individual molecular orbitals*, Physical Review Letters **94**, 026803 (2005).
- [172] P. Liljeroth, I. Swart, S. Paavilainen, J. Repp, and G. Meyer, *Single-Molecule Synthesis and Characterization of Metal-Ligand Complexes by Low-Temperature STM*, Nano Letters **10**, 2475 (2010).
- [173] P. Liljeroth, J. Repp, and G. Meyer, *Current-induced hydrogen tautomerization and conductance switching of naphthalocyanine molecules*, Science **317**, 1203 (2007).
- [174] J. Repp, G. Meyer, S. Paavilainen, F. E. Olsson, and M. Persson, *Imaging bond formation between a gold atom and pentacene on an insulating surface*, Science **312**, 1196 (2006).
- [175] K. Petukhov, M. Alam, H. Rupp, S. Strömsdörfer, P. Müller, A. Scheurer, R. Saalfrank, J. Kortus, A. Postnikov, M. Ruben, *et al.*, *STM spectroscopy of magnetic molecules*, Coordination Chemistry Reviews **253**, 2387 (2009).
- [176] D.-J. Choi, C. Rubio-Verdú, J. de Bruijckere, M. M. Ugeda, N. Lorente, and J. I. Pascual, *Mapping the orbital structure of impurity bound states in a superconductor*, Nature Communications **8** (2017).



# SUMMARY

This thesis work is dedicated to STM studies of single surface adatoms and roles these systems have as working platforms in understanding quantum magnetism. To that end, here I show experimental work on single Co adatoms in UHV at low temperatures. Experiments are performed with the adatoms placed on three distinct solid surfaces – nitride-reconstructed Cu(100), nitride-reconstructed Cu<sub>3</sub>Au(100) and Cl-reconstructed Cu(111). Next to the studies on single adatoms, studies on Co atomic chains built in different surface geometries on nitride-reconstructed Cu(100) are presented.

**Chapter 1** introduces the topic of quantum simulation and explains the role STM studies on magnetic adatoms have in it as an analog simulation tool.

In **chapter 2** I present the basic elements of the theory behind the theoretical model of a particular spin-1/2 chain – XY chain in transverse field. Formal mapping of this well-established theoretical spin chain model onto our atom-by-atom STM-assembled Co chains, discussed in chapter 5, is described. Put in terms of quantum simulation, here I explain the correspondence between a quantum system we want to simulate (XY chain in transverse field) and its analog QS (our Co chain).

**Chapter 3** contains the information on the experimental STM setups and measurement techniques we used in the adatoms studies presented here. Also, here I give a general description of our in-situ preparation methods of surface platforms used for adatom studies in subsequent chapters.

**Chapter 4** presents a detailed discussion on the three surface platforms used for studies on Co adatoms in this thesis – nitride-reconstructed Cu(100), nitride-reconstructed Cu<sub>3</sub>Au(100) and Cl-reconstructed Cu(111). In addition to that, a basic building block for Co chains presented later in this thesis – a Co two-atom chain on nitride-reconstructed Cu(100) – is explored here in great detail. An initial study on single Co atoms on nitride-reconstructed Cu<sub>3</sub>Au(100) is shown here as well as this surface reconstruction could potentially allow for STM construction of atomic structures at least an order of magnitude larger compared to the nitride-reconstruction on Cu(100). A third platform, a Cl-reconstructed Cu(111), is described at the end of the chapter. This surface platform holds promise for surpassing both previously mentioned ones in terms of the size of atomic structures one could build on it and, due to its geometry, might be useful for studies on atomic frustrated magnets.

In **chapter 5** I present a study on Co chains built along the N-vacancy direction on nitride-reconstructed Cu(100). These chains represent an STM realization of an analog QS for the XY chain in transverse field described in chapter 2. The STM-STS study as a function of the chain size and the transverse magnetic field reveals the onset of quantum criticality in our finite chains. In a limit of an infinite chain, this would lead to a quantum phase transition.

**Chapter 6** identifies another function of an STM in atomic magnetism studies – the one of a control button for magnetic excitations of the atom. Namely, by modifying the direct surroundings of an atom, we demonstrate STM-controllable suppression of magnetic excitations in atomic chains. Findings presented here result from a study on Co chains assembled along the N-direction on nitride-reconstructed Cu(100).

In **chapter 7** I show results on a novel system – a Co adatom on a Cl-reconstructed Cu(111) surface. STM-IETS findings, supported by DFT and multiplet calculations, suggest we are probing inelastic excitations of the Co atom with subatomic resolution.

# SAMENVATTING

Dit proefschrift is gewijd aan STM onderzoek aan individuele atomen op oppervlakken en de rol die deze kunnen hebben als platform voor het begrijpen van kwantummagnetisme. Daarin laat ik experimenteel werk zien met enkelvoudige Co atomen in ultrahoog vacuüm bij lage temperatuur. De experimenten hierin zijn uitgevoerd op drie verschillende oppervlakken – N-gereconstrueerd Cu(100), N-gereconstrueerd Cu<sub>3</sub>Au(100) en Cl-gereconstrueerd Cu(111). Daarnaast zijn Co atoomketens van verschillende vormen op N-gereconstrueerd Cu(100) bestudeerd.

**Hoofdstuk 1** introduceert het concept van kwantumsimulatie en beschrijft de rol van STM onderzoek aan magnetische atomen als een analoge simulatietechniek.

In **hoofdstuk 2** presenteer ik de basiselementen van de theorie achter een specifieke spin-1/2 keten – de XY keten in een transversaal veld. De toepassing van dit bekende theoretische spin-ketenmodel op onze atoom-voor-atoom STM-geassembleerde Co ketens wordt beschreven in hoofdstuk 5. Beschreven in termen van kwantumsimulatie, leg ik hier de overeenkomst uit tussen het kwantumsysteem dat we willen simuleren (de XY-keten in transversaal veld) en het bijbehorende analoge kwantumsysteem (onze Co atoomketen).

**Hoofdstuk 3** bevat informatie over de experimentele STM-opstellingen en meettechnieken die we hebben gebruikt in het hier gepresenteerde onderzoek. Ook geef ik hier een algemene beschrijving van onze in-situ preparatiemethoden voor verschillende oppervlakken die worden gebruikt voor experimenten in de volgende hoofdstukken.

**Hoofdstuk 4** presenteert een gedetailleerde discussie over de drie oppervlakteplatforms die worden gebruikt voor studies van Co atomen in dit proefschrift – N-gereconstrueerd Cu(100), N-gereconstrueerd Cu<sub>3</sub>Au(100) en Cl-gereconstrueerd Cu(111). Daarnaast wordt hier in detail het basiselement van Co ketens geïntroduceerd dat pas later in dit proefschrift formeel wordt gepresenteerd: een Co dimeer op N-gereconstrueerd Cu(100). Tevens wordt hier een eerste studie van enkelvoudige Co atomen op N-gereconstrueerd Cu<sub>3</sub>Au(100) getoond: dit oppervlak zou de constructie van atoomstructuren mogelijk maken die ten minste een orde van grootte groter zijn dan op N-gereconstrueerd Cu(100). Een derde oppervlak, Cl-gereconstrueerd Cu(111), wordt aan het eind van het hoofdstuk beschreven. Dit oppervlak is veelbelovend voor het overtreffen van beide eerder genoemde in termen van de grootte van atoomstructuren die men daarop zou kunnen bouwen en, vanwege de geometrie, wellicht nuttig voor studies over atomisch gefrustreerde magneten.

In **hoofdstuk 5** presenteer ik een onderzoek aan Co ketens gebouwd langs de N-vacature-richting op N-gereconstrueerd Cu(100). Deze ketens vertegenwoordigen een STM-realitatie van een analoog kwantumsysteem voor de XY-keten in een transversaal veld beschreven in hoofdstuk 2. Het STM-STS-onderzoek als functie van de ketenlengte en van het transversale magnetische veld onthult het opkomen van kwantumkritisch gedrag in onze ketens. In de limiet van een oneindige keten zou dit leiden tot een kwantumfase-transitie.

**Hoofdstuk 6** identificeert een andere functie van de STM in onderzoeken over atomair magnetisme – die van een aan/uit schakelaar voor magnetische excitaties aan het atoom. Door modificatie van de directe omgeving van een atoom, demonstreren we een controleerbare onderdrukking van magnetische excitaties in atoomketens. De hier gepresenteerde bevindingen zijn het resultaat van een onderzoek naar Co ketens samengesteld in de N-richting op N-gereconstrueerd Cu(100).

In **hoofdstuk 7** toon ik resultaten over een nieuw systeem – een Co atoom op een Cl-gereconstrueerd Cu(111)-oppervlak. STM-IETS bevindingen, ondersteund door DFT en multiplet berekeningen, suggereren dat we inelastische excitaties van het Co atoom detecteren met subatomaire resolutie.

# ACKNOWLEDGEMENTS

A good summary of the last four years would say a pleasure of doing beautiful science, fun with colleagues and friends, making beautiful music and an awful lot of personal and professional growth, for all of which I am very grateful to the people I had shared all these experiences with.

First, I wish to thank all the committee members for accepting to take part in my thesis defense and the time they took in reading my thesis. It is an honour for me to have you in my committee.

I will continue by expressing my gratitude to the group responsible for my arrival to TU Delft and for the great research I was able to be a part of ever since.

Sander, thank you for providing me with the opportunity to "play God" with single atoms – I can only hope to find a topic in my future career that will be as beautiful as the research I've done on single atoms in your group. Your genuine interest in the line of research you do and constant stimulation you provide with your own hard work were great motivators. I can truly say you were formally and really my daily supervisor – your continual guidance and care for my research progress were highly useful in steering my PhD journey in the right direction and in a timely fashion. Also, thanks for the many Belvédère team building celebration activities! Discouraging my laziness in speaking Dutch is already paying off, so thank you for that as well! Lastly, but importantly, thank you for the professional guidance, that went beyond the scope of science, you unreservedly provided during my first four years of professional work.

The time spent in the Otte lab would not have been as productive and fun without all the people I had the opportunity to work with. Ben and Anna, thank you for helping me in making my first steps in the lab. Thanks to both of you, I had a very fast and successful start of my experimental research. Anna, thanks for the many coffee breaks, theory discussions and all the tips you passed onto me as a senior PhD student. Ben, thank you for being keen on the lab running as smoothly as possible and for your Igor Pro functions that made the data analysis much easier. Floris, we began our PhD adventures on the same day and I have since seen you rise to a scientific celebrity while becoming an engaged and later, an honest<sup>1</sup>, man – well done and keep up the success rate! Also, don't neglect singing – the world cannot have enough tenors. Jan, thank you for all the generous help with the lab and the data analysis and for all the nice talks we had in the labs and the bars. I hope you will manage to recover from the Toblerone-induced dip in your bank statement. I wish you and Zuzana much luck with your careers and your life together! Jérémie, I am very happy you joined our group all the way from the Great White North as I enjoyed very much playing a senior PhD colleague in the lab, so thank

---

<sup>1</sup>Here: "honest" = "married".

you for that experience. Also, having a computer wizard like you helped many times – thanks. I wish you much success in the rest of your PhD and I applaud your and Marie's handling of pursuing PhDs together with Sedna. I hope you are finding time to enjoy it all. Mari, I like your serenity in challenging moments – maybe yoga really helps if one has true focus. Thank you for the much needed initial push in my attempt to be more sporty. David, keep up the enthusiasm and hard work (and humor) and I am sure they will pay off! Robbie, may you have nice papers to come and many more students to teach (and many less transatlantic airfares to pay) – good luck with your PhD. Willeke, keep up your cheerful spirit and I hope to see you for many more Wed evenings to come in the Culture Center.

To the students I had the pleasure to supervise – thank you all so much for the countless fun moments in the lab and your good work – I enjoyed working with each one of you a lot! Mariska, my first student – I am glad to see you developed a passion for science. I wish you good luck with your PhD. Bruno, I enjoyed your positive attitude and appreciated your nice work. I am confident your professional life will be a success and I am looking forward to see where it takes you. Marnix, your contribution to our lab was consistently exceptional. I believe your work dedication in combination with your skills can only lead to success in whatever you decide to do. Also, thank you for making the lab time a great fun with your wonderful, twisted humor. Nena, I learned to enjoy your direct approach in communication and thank you for the valuable contribution you left behind. Olaf, it was fun co-supervising you – I wish you much luck in your further studies. Mitchel, my last student – I hope I used properly all the knowledge the five students before you gave me. It was certainly a pleasure for me to supervise someone with your level of self-organization and such pro-active attitude. My black book had no pages for you. Marjolein and Nora – I haven't supervised you, but I am glad we got to work together. Marjolein, I shared my first months of this PhD journey with you in the lab – it was nice having someone side by side in that period of initial training and I thank you for that. Nora, great contribution to our work – I am sure you'll make an excellent experimentalist. To Hans, Shang-Jen, Thomas, Lucas, Daniëlle, Floris, Laurien, Maryam and Lukas – it was very nice crossing paths with you while in the Otte lab.

Upon my arrival to The Netherlands I was lucky enough to have some old friends nearby that made me feel less foreign and whose presence made a huge difference for the better in some challenging moments of my stay here. Dejan and Laura – thank you for accepting to be my paranymphs and I hope my luck doesn't run out and you remain close by in the years to come as well.

Dejan, we shared the same countries/towns/universities/departments for most of the last seven years and it gives me satisfaction to see you not only becoming what you wanted since the beginning of our master – a physicist – but one respected by peers and professors alike (and with 15 publications and counting)! Well done! What I am even more proud of are many great moments we shared together during and outside of our studies and work, so thank you for those and all the ones that are yet to come<sup>2</sup>!

---

<sup>2</sup>For the sake of keeping this chapter somewhat concise and less sappy, I will not detail further.

On a side note, having a personal career/money<sup>3</sup>/toeslagen/whatnot consultant free of charge proved to be very useful in numerous situations. Thanks to both you and Magdalena for being organizers and such welcoming hosts of countless dinners, barbecues and parties.

Laura, it was to my big pleasure to learn you'll be joining TU Delft and four years later I am filled with memories of tulip fields, dinners, board game nights and King's days – thank you for the many times we were making these memories together. I am happy I managed to partially thank you for all these by introducing you to Taylor<sup>4</sup>. Thank you both for trying to turn me into a restaurant-goer and thank you for all the nice evenings and the support! Also, Taylor, thank you for accepting to be my defense photographer!

I joined Otte lab that at the time formed a part of a group called MED. Nice atmosphere of a small close group and a few great traditions describe the MED group well. I also enjoyed the MED expansion and development into the QN department we know now as this brought together a whole lot of people many of which I had the opportunity to share some nice experiences with. In my memory, MED/QN will remain not only as a vast source of intelligent people with a passion for physics, but also as a place where I met interesting people and made some, what I'm sure will be, long-lasting relationships.

I will start with my many office mates. Throughout the course of my PhD, I stayed in a total of four offices. My first office mates – Nandini and Floris – were also the ones I shared my office history the shortest. Nandini, thanks for all the relaxed evenings, Indian treats you brought from back home and for your company (all of which I enjoyed way more than the spices in your dinners<sup>5</sup>). Your stress resilience is exemplary – I wish you success in your marriage and your career, wherever those two take you. Also, thanks for continuously expanding my English vocabulary. Floris, see above. My second and third office were shared with Ignacio, Emre and Richard. Ignacio, you make everyone look bad on the dance floor and I will not thank you for that<sup>6</sup>. I will thank you for all the talks and I will thank you and Rocío for the raclette grill dinners and Chilean pisco! Emre, I hope you enjoyed my office company as much I did yours. Thanks for all the talks and for all the Turkish delight. Richard, I wish your science enthusiasm gets rewarded in form of a fruitful career – good luck! This brings me to my last office and office mates I spent most of the time with – Jérémie, Mari, Miguel, Luigi and Dima. This was a great mix and I had a lot of fun with you! My thesis writing schedule shouts against it, but I wish to thank you for all that fun. Jérémie, it was a pleasure having you a table away<sup>7</sup>. Mari and Miguel, guardians of the (E)Spanish group, thanks for all those coffee breaks and banana muffins. Miguel, thank you for all the talks, advice and support! Also, thank you for all the coffee service and for the mug I'll bring with me to whichever office I go to from now on. Luigi, I am sorry I won't be around to witness all your weirdness. Good luck and much fun in transitioning to an experimentalist! Dima, I enjoyed our talks and sorry for all the times I interrupted your Skype sessions! I wish you a successful experimental run

<sup>3</sup>I do hope one day you learn to apply your skills on your own finance matters.

<sup>4</sup>I had to bring this to public notice in case it gets omitted in both your theses.

<sup>5</sup>for which I am grateful too

<sup>6</sup>Floris, idem.

<sup>7</sup>It was less of a pleasure when you decided to leave.

on your set-up, many papers to come and a successful next career step. It would not be fair excluding Sonia from this last office group. Sonia, thank you for popping into our office so often and for the consistent input of positive drive you bring along. Also, thank you for making sure a part of that drive comes in a form of chocolate supply.

I will continue with mentioning people I met outside my office but enjoyed nevertheless. Yildiz, you brought vibrant mood to our department – keep sharing it generously! I thank you for your warm and welcoming nature and many nice occasions we spent dining and dancing. You've shown your spirit cannot be tamed even by major setbacks – I applaud you on that! Mafalda, I was happy to see you join our department as a PhD colleague and I am happy to see you (about to) leave it as my friend. Martijn, thank you for serving as a great host of many fun evenings in Rotterdam – I am happy your brother had a spare lizard that Nandini wanted. Nikos, thank you for your bbq skills and for being that easy-going – I enjoyed our talks a lot. I hope to see you and Andrea for many more dinners and parties in my post-PhD period as well. Felix, thanks for the bass support in Krashna – I hope to be enjoying it for a long time to come. I wish you many less international weekend trips in the near future and many papers to compensate your many long days and weekends. Santiago, thank you for all the hospitality you've shown numerous times as the party host. I had a lot of fun with you and Gabi and I wish you two a lot of success in your future life together! Joao, I hope you'll enjoy Krashna as much I did. Thank you for the help with the job search and I'm looking forward to discussing many more TV shows with you! Joeri, it's a pleasure to talk to someone that calm and well-reasoned. Davide, thank you for your kind nature. I wish you much success in the rest of your PhD time. Anastasia, thanks for the inburgeringsexamen tips. Good luck with your future research and not getting hurt in your fencing competitions. Rocco, as much as I do not miss your thunderous laughter in the corridors, I wish you best of luck and joy with your postdoc. Lucinda, thank you for the enthusiasm and practical support you provided in my job hunt – I appreciated it a lot. Inge, it was nice having your uplifting spirit around. Thanks for the chats and good luck with your PhD! Alexandra, one of the few who shared my views on the importance of transferable skills for scientists – thanks for the talks and good luck with your next career steps. Giordano, I will do my best to acknowledge you as meaningfully as you did me. Dirk, I am looking forward to seeing more of your forgotten dancing hobby in action. Sabina, I wish you many grants to come – good luck! Venkatesh, thanks for the help with the job hunt. Vera, Julien, Max, Pablo, Sal, Thierry, Holger, Iacopo, Daniel, Ines, Igor, Andreas, Claus, Pascal, Marc, Clemens, Joshua, Enrique, Shun, Ben S., Mingyun, Riccardo, Michele, Mickael, Sofya, Robin, Jorrit and others – good luck with your research and your jobs and thanks for the nice sporadic talks we had! To all the professors of the department – thank you for letting us do nice science and for stimulating each other and all of us by continuously raising the bar higher.

I would be unfair to end my list of thanks to the QN department without mentioning the QN support staff. Etty, your help with the apartment was perhaps crucial – I highly appreciate it<sup>8</sup>! Maria, thank you for encouraging me to use Dutch more often – my written Dutch in particular thanks you! Dorine, I am a big fan of the inspirational notes on

---

<sup>8</sup>Thank you, Kobus, for the signature.

the board of the Project Office and the team building borrels you are organizing together with Heleen and the rest of the support staff. Tino, thanks for all the help with lab-related requests and nice random chats. Casimir Research School has been an organizer of a few editions of spring and winter schools that I got to enjoy throughout the years, being a QN PhD student. Marije, thank you for organizing such great events and for all the career-related workshops, company visits and informal get-together events made for people belonging to the Casimir Research School – very useful and a great deal of fun.

My time at TU Delft has also been marked by its music society – Krashna Musika. To all the singers and players I owe a big thanks for all the joy we had making wonderful music together. I hope to be able to sing with you for a long time to come! Dena, thanks for being the initial glue of our internationals/PhDs-singers group – I wish you every success in your postdoc in Canada and a safe trip back to The Netherlands thereafter. Jaime, thank you for the second prom and for all the support, talks and cakes you gave me along the way. My voice thanks you for being pushy enough to make me join the chamber choir. As I got used to all these services you provide, I very much hope you'll be around for a long time to come. Alexey, thanks for constant effort in trying to make a swimmer out of me and all the bar gezelligheid that followed many of those attempt sessions. Arturo, thank you for all the gezellige dinners and fun nights out. Jay, keep up your enthusiasm and see you at many more barbecues and get-togethers. Tommaso, Ozan, Doedo, Joris, Sophie and my many other singing buddies – you all made my choir experience in Krashna a great one! Encar, I envy you on your way of working and I hope your travel thirst doesn't take you far away on a long run. Susana, thank you for your tips on the naturalization process and the job search. While I'm here, I mustn't forget the first choir that made me fall in love with choir music in the first place – LUK from KU Leuven. I met so many nice and welcoming people there and I thank you all for the great year I had with you. My gratitude extends to the Corus Acusticus, my choir from Sweden, who made that long dark winter a much brighter experience. Finally, a big "thank you" to all of my friends who showed support by coming to my concerts! My experiment with Rock'n'Roll dancing led me to a fun year with people from Rock'n Delft – thank you all for the dance evenings!

To the main protectors of my spoken and written skills in my mother tongue in The Netherlands – Dejan, Aleksandar Jov. and Sasa – I owe a "Hvala!". Dejan, you have enough lines as it is. Aleksandar, I have enjoyed our Locus evenings and your stories<sup>9</sup> and I hope to see you and Katarina in similar settings for many more of them! Sasa, I am happy you made a guest appearance in our lab for your project. I had a lot of fun working with you and running into you at conferences/job fairs and I hope for many more non-random encounters to come! Also, it was fun sharing experiences during the job search. Aleksandar Jac.<sup>10</sup> and Selma, may we meet for more dinners in Delft/wherever we are! Diana, it was nice having you stop by from time to time!

---

<sup>9</sup>long and short

<sup>10</sup>Thank you for inviting me to be a speaker at the OMSA-organized evening of young researchers at the Science Festival in Montenegro – I enjoyed it a lot!

I mustn't forget people whose muscles made it much easier for me to move places a few times. Dejan, Jérémie, Aleksandar Jov., Ignacio, Julien, Martijn, Taylor, Aday – I applaud you on your strength, cargobike- and car-driving skills and wardrobe-assembling craftsmanship and I thank you for your willingness to use them for my moving adventures.

I would like to thank the ones who contributed to my thesis having the shape you, dear reader, are encountering now. Sander, thank you for the prompt reading of my thesis, constructive suggestions you made throughout the writing process and the help with the translation to Dutch. Mari, thank you for the beautiful cover design! Martijn and Luigi, thank you two as well for the help with the translation to Dutch. Dejan, thank you for the help with LaTeX.

To my teachers and professors from back home in Montenegro who encouraged me to continue my studies abroad and pursue a PhD eventually – S. Pavicevic, Prof. J. Mirkovic<sup>11</sup> and Prof. N. Tadic<sup>12</sup> – thank you for being sufficiently convincing! To the group of Prof. F. Lombardi<sup>13</sup> at Chalmers University of Technology where I've conducted research for my master thesis – these were my very first months in a researcher role and months that reinforced in me the desire to continue conducting research, and I thank you for that. To all my supervisors – thank you for showing me how passionate a researcher can be about their work.

The list would not be complete without mentioning some people outside The Netherlands. My hometown friends, with a decade or two of history – Ana T., Ana P., Sanja, Dragana, Dijana, Miladin, Gigo, Ljubica, Stevan – thank you for believing in me and constantly cheering me! Looking forward to the decades to come! My friends from the university days – Andrea, Aleksandra, Natasa, Ana A., Jovana, Milos V., Aleksandar D., Ivan V., Stefan, Radomir S., Danilo D., Danilo C., Ivana, Zarko, Andjela, Milos B., Milica – it is always a pleasure to come back home or go wherever you are and see you again and I hope for much more of that from now on! To my EMM Nano friends who did not end up becoming my paranymphs – Fabian, Max, Anna K., Mattias, Alfonso, Francisco, Valerie, Lennart and many more – master years were my first years of living abroad and will always be special. Thank you for being an important part of them. To my other friends from my master period – Lejla, Severin, Kaveh, Licia and many others – those were two great years and I thank you for being in them with the hope to see more of you in the future! To my new friends: Marija and Javier – may we meet in many more European capitals; Grazia – wish you lots of success and a great job in The Netherlands!

My utmost gratitude is reserved for my parents, Marta and Momir, and their unconditional love, caring and support – I hope to be able to reciprocate for all that in an attempt to show how much I appreciated the belief you had in me for as long as I can remember. My gratitude for unreserved support extends to my sister, Milena, and my brothers, Vladimir and Ivan, of whom I am proud and I can't wait to see and celebrate their achievements in the years to come. To you five I owe the most and my thanks can merely begin to cover it.

---

<sup>11</sup>I wish you all success in bringing the world of nanotechnologies closer to Montenegro.

<sup>12</sup>I attach the name of M. Zogovic here and I thank you both for always fun catching up sessions in your kafana.

<sup>13</sup>Especially Prof. F. Lombardi and my daily supervisor R. Arpaia

# CURRICULUM VITÆ

## Ranko Toskovic

- 23-05-1988 Born in Niksic, Montenegro.
- 2003–2007 Gymnasium (average grade 5/5)  
Stojan Cerovic, Niksic, Montenegro
- 2007–2010 B.Sc. in Electrical Engineering (average grade 10/10)  
University of Montenegro, Podgorica, Montenegro
- 2007–2010 120 ECTS of B.Sc. in Physics (average grade 10/10)  
University of Montenegro, Podgorica, Montenegro
- 2010–2011 Specialization studies in Electronics (average grade 10/10)  
University of Montenegro, Podgorica, Montenegro  
*Thesis:* Voltage controlled relaxation oscillator based on Schmitt trigger  
*Supervisor:* Prof. dr. N. Tadic
- 2011–2013 M.Sc. in Nanoscience and Nanotechnology (*summa cum laude*)  
KU Leuven, Leuven, Belgium (2011–2012)  
Chalmers University of Technology, Gothenburg, Sweden (2012–2013)  
*Thesis:* Doping dependent transport in YBCO nanostructures: insights into the microscopic mechanism for high critical temperature superconductivity  
*Supervisor:* Prof. dr. F. Lombardi
- 2014–2018 Ph.D. in Experimental Physics  
Delft University of Technology, Delft, The Netherlands  
*Thesis:* Magnetic adatoms as building blocks for quantum magnetism  
*Promotor:* Dr. A.F. Otte  
*Promotor:* Prof. dr. ir. H.S.J. van der Zant



# LIST OF PUBLICATIONS

7. **R. Toskovic**, M.C. Martinez Velarte, J. Girovsky, M. Kokken, J. W. González, F. Delgado, and A.F. Otte, *Orbital-specificity in probing inelastic excitations in single Co adatoms on Cl-reconstructed Cu(111)*, manuscript in preparation.
6. F. E. Kalf, M.P. Rebergen, E. Fahrenfort, J. Girovsky, **R. Toskovic**, J.L. Lado, J. Fernández-Rossier, and A.F. Otte, *A kilobyte rewritable atomic memory*, [Nature Nanotechnology](#) **11**, 926 (2016).
5. **R. Toskovic\***, R. v/r Berg\*, A. Spinelli, I.S. Eliens, B. v/d Toorn, B. Bryant, J.-S. Caux, and A.F. Otte, *Atomic spin-chain realization of a model for quantum criticality*, [Nature Physics](#) **12**, 656 (2016).
4. A. Spinelli, M. Gerrits, **R. Toskovic**, B. Bryant, M. Ternes, and A.F. Otte, *Exploring the phase diagram of the two-impurity Kondo problem*, [Nature Communications](#) **6**, 10046 (2015).
3. B. Bryant, **R. Toskovic**, A. Ferrón, J.L. Lado, A. Spinelli, J. Fernández-Rossier, and A.F. Otte, *Controlled complete suppression of single-atom inelastic spin and orbital cotunneling*, [Nano Letters](#) **15**, 6542 (2015).
2. R. Arpaia, S. Charpentier, **R. Toskovic**, T. Bauch, and F. Lombardi, *YBa<sub>2</sub>Cu<sub>3</sub>O<sub>7-δ</sub> nanorings to probe fluxoid quantization in High Critical Temperature Superconductors*, [Physica C: Superconductivity and its Applications](#) **506**, 184 (2014).
1. S.M. Perovich, M.P. Calasan, and **R. Toskovic**, *On the exact analytical solution of some families of equilibrium critical thickness transcendental equations*, [AIP Advances](#) **4**, 117124 (2014).

\* Authors contributed equally.